NEPAL JOURNAL OF SCIENCE AND TECHNOLOGY

Vol.23(1)
NEPAL ACADEMY OF SCIENCE AND TECHNOLOGY
KATHMANDU, NEPAL

Nepal Journal of Science and Technology (NJST) Board Members

Table of Contents

Content

Pages

Study of Dose Measurement and Its Effects Using Relative Hp(10) and Uncertainty Across Different Radiation Field Sizes and Energies

Ram Saran Karki[1], Bidyapati Jha[1], Raju Khanal[1], Agni Dhakal[2] and Buddha Ram Shah[2*]

[1] Central Department of Physics, Tribhuvan University, Kritipur, Kathmandu, Nepal
[2] Faculty of Science, Nepal Academy of Science and Technology, Khumaltar, Lalitpur, Nepal

***CORRESPONDING AUTHOR:**
Buddha Ram Shah
Email: buddharshah25@gmail.com

ISSN : 2382-5359(Online), 1994-1412(Print)

DOI:
https://doi.org/10.3126/njst.v22i2.100107

Date of Submission: 17 Mar, 2025

Date of Acceptance: 25 Jun, 2026

ABSTRACT

This work investigates the dosimetric behavior of relative Hp (10) at various energy levels and radiation field sizes with particular attention to radiation field positions. The goal is to measure the associated uncertainties and evaluate the relative variations in Hp (10) at various positions. The study seeks to improve accuracy in clinical radiation therapy and protection by analyzing the influence of field size and energy on dose distribution. The calibrated dosimeters were used in clinically relevant conditions, with field sizes ranging from 10 ×10 cm² to 25×25 cm². Six and fifteen Megavolts of energy were studied. Multiple dosimetric behaviors were captured by focusing on central and off-center positions during the three different positions where the measurements were taken within the radiation field. Examining the impact of varying energy levels and field sizes on the dose distribution is a crucial step toward quantifying uncertainties and fluctuations in relative Hp(10). In applications involving clinical radiation therapy, the analysis is essential for safeguarding and maximizing dose delivery.

Keywords: Relative Hp (10), Uncertainty, Radiation field size, Energy levels (MV), Radiation therapy

1. INTRODUCTION

The foundation of cancer treatment is radiation therapy, where precise dosimetry, an accurate measurement and control of the radiation dose administered, is necessary to guarantee that the target tissues receive the right amount of radiation while limiting exposure to nearby healthy tissues. Hp (10) or the dose equivalent for deep tissues is a significant number in dosimetry that is essential for tracking radiation exposure during treatment.

The energy level and field size are two factors that affect how difficult it is to dose radiation accurately. The radiation dose distribution is greatly influenced by these factors; larger field sizes usually result in increased scatter and beam divergence, which lowers the dose at periphery positions. Furthermore, radiation energy influences the penetration depth, influencing the distribution of doses in various tissue layers. To ensure that the dose administered adheres to the recommended treatment plan, these factors must be carefully considered, especially in off-center locations within the radiation field.

Field size and energy effects on dosimetry have been studied in the past. The need for standardized dosimetry across various field sizes was highlighted when the International Atomic Energy Agency (2000) established protocols for calculating absorbed doses in external beam radiation. By concentrating on relative Hp (10) measurements across various field sizes and energy levels, this work expands on that basis and contributes to a better understanding of dose distribution in clinical settings. Uncertainty is a crucial component of dosimetry and can be attributed to several factors, including patient variability, measurement technique, and calibration.

There are two types of uncertainty: random, which changes with every measurement, and systematic, which affects all measurements equally (e. g. calibration errors). Both types of uncertainty must be reduced for patient safety and accurate dosage administration. To ensure accurate dosage administration and patient safety, both kinds of uncertainty need to be reduced. Understanding the sources of uncertainty, particularly about different energy levels and field sizes, can help improve the accuracy of radiation therapy.

This work looks at relative Hp (10) at different energy levels and different positions in the radiation field. The study's results will provide a comprehensive analysis of the related uncertainties in addition to quantifying the influence of these factors on dose distribution, which will aid in the creation of more exacting protocols for precise dosimetry in clinical practice.

2. MATERIALS AND METHODS

2.1 Experimental Setup

For the experimental study, Harshaw 6600 plus model Thermo luminescent Dosimeter Instrument is used to read the dosimeters, which is shown in Figure 2. Also, Thermo Luminescent Dosimeter (TLD) cards, as shown in Figure 1, were used to assess the radiation dose distribution. The dosimetric study was conducted using calibrated dosimeters placed at positions P1, P2, and P3, corresponding to different geometric locations of the radiation field. The experiments were carried out under controlled conditions, ensuring that external variables such as room temperature, pressure, and humidity were consistent throughout the measurements.

Precise dosimetric measurements are crucial for ensuring patient safety and accurate radiation therapy. The use of personal dosimeters for measuring Hp (10), which represents the dose equivalent at a 10 mm depth in tissue, is one of the key methods to assess radiation exposure. This paper aims to analyze the relative Hp (10) for different field sizes and energies, comparing them across three distinct positions (P1, P2, and P3) and investigating the associated uncertainties.

***Fig 1:** Thermo luminescent Dosimeter (TLD) Card*

Fig. 2: Harshaw 6600 plus model Thermo luminescent Dosimeter (TLD) Instrument

2.2 Field Sizes and Energy Levels

Four different field sizes were used for the

measurements:

10×10 cm²

15×15 cm²

20×20 cm²

25×25 cm²

These field sizes represent a range of conditions typically encountered in clinical radiotherapy. Each field size was tested with two energy levels:

6 MV: Commonly used for superficial radiation treatments.

15 MV: Utilized for deeper tissue penetration.

2.3 Positions

The dosimeters were placed at three positions:

P1: Located near the central axis of the field.

P2: Situated slightly off-center.

P3: Positioned near the edge of the field.

The placement of the dosimeters allow for a thorough investigation of how radiation dose varies across the field. For each combination of field size, energy, and position, the mean relative Hp (10) was recorded, and the corresponding standard deviation (S.D.) was used to calculate the uncertainty.

2.4 Calculation of Uncertainty

Uncertainty in dosimetric measurements arises from both statistical and systematic sources. The statistical uncertainty was derived from the standard deviation of repeated measurements, while systematic uncertainty was estimated based on equipment calibration and environmental factors. The overall uncertainty was calculated using the formula.

Uncertainty in dosimetric measurements is a crucial factor affecting the reliability of results. In this experiment, the uncertainty was quantified using standard deviation (S.D.) and percentage uncertainty.

The different influential factors contributed to uncertainty, such as detector sensitivity, beam stability, and environmental conditions. Due to these factors, the uncertainty values observed were not as finely controlled as desired. Uncertainty was more pronounced for smaller fields and peripheral positions (P1 and P3). However, in this study, instrumental error is the only factor for uncertainty. Statistical analysis was conducted using Python programming in Jupyter Notebook.

3. RESULTS AND DISCUSSION

Table 1: The following data summarize the relative Hp(10), standard deviation (S.D.), and calculated uncertainty for each field size (dimension), energy in MV, and position.

S.N	Dimension (cm²)	Energy (MeV)	Position	Relative Hp(10)	S.D.	Uncertainty (%)	Scattered Dose % (5 cm)
1	1010	6	P1	1.05	0.043	4.096	3.98
2	1010	6	P2	0.95	0.036	3.797	
3	1010	6	P3	0.88	0.091	10.418	
4	1515	6	P1	1.11	0.011	0.994	5.86
5	1515	6	P2	0.96	0.004	0.372	
6	1515	6	P3	0.9	0.053	5.847	
7	2020	6	P1	1.28	0.013	0.997	6.69
8	2020	6	P2	1.19	0.043	3.609	
9	2020	6	P3	1.14	0.026	2.302	
10	2525	6	P1	1.28	0.01	0.779	7.67
11	2525	6	P2	1.24	0.027	2.142	
12	2525	6	P3	1.21	0.021	1.765	
13	1010	15	P1	1.26	0.008	0.596	3.93
14	1010	15	P2	1.21	0.007	0.537	
15	1010	15	P3	1.17	0.026	2.244	

16	1515	15	P1	1.28	0.013	1.018	3.93
17	1515	15	P2	1.24	0.036	2.936	
18	1515	15	P3	1.21	0.006	0.455	
19	2020	15	P1	1.3	0.009	0.717	9.49
20	2020	15	P2	1.26	0.015	1.19	
21	2020	15	P3	1.23	0.023	1.91	
22	2525	15	P1	1.35	0.014	1.025	11.49
23	2525	15	P2	1.31	0.027	2.03	
24	2525	15	P3	1.27	0.03	2.317	

Table 1 presents the measured relative Hp (10), standard deviation (S.D.), and calculated uncertainty percentages for various radiation field sizes (ranging from 10×10 cm² to 25×25 cm²), energies (6 MV and 15 MV), and three detector positions (P1, P2, and P3). The data reveals that higher relative Hp (10) values are generally recorded at central position P1, with values increasing as the field size enlarges. The 15 MV energy consistently produces higher and more stable dose readings across all positions compared to 6 MV, as indicated by the lower uncertainties. Notably, uncertainties are highest at P3 and in smaller fields (especially for 6 MV), reflecting greater dose fluctuation near the edges of the radiation field and at lower energies. The scattered dose values, reported for selected field sizes, further support the observation that dose dispersion increases with field size, with 25×25 cm² showing the highest scattered dose percentages.

Table 2: Radiation Dose Received by 4 walls during exposure time

TLD ID	Position	1st Exposure (mSv)	2nd Exposure (mSv)	3rd Exposure (mSv)	Distance from Center (cm)
a1001498t	P(e)	1.97	1.29	0.5	410
a1001091t	P(w)	0.48	0.66	0.22	420
a1000469t	P(s)	1.3	0.95	0.37	380
a1001501t	P(n)	0.48	0.55	0.21	370

Table 2 summarizes the radiation dose received by four walls of the treatment room during three exposure events, with dosimeters placed at designated positions: east (P(e)), west (P(w)), south (P(s)), and north (P(n)). The data indicates that the wall located east (P(e)) received the highest cumulative dose over three exposures, reaching up to 1.97 mSv in the first exposure. In contrast, the west and north positions received relatively lower doses. Dose measurements show a declining trend from the first to the third exposure in all positions, which may be attributed to time-dependent decay of scattered radiation or beam directionality. Additionally, the distance of each wall from the radiation field center ranges between 370 cm and 420 cm, correlating to a gradient in dose intensity with increasing distance, reinforcing the importance of room shielding and layout in radiotherapy environments.

From Fig. 3, at P1 (dashed blue lines): Both energies show increasing doses as the field size increases. However, the 15 MV dose (solid line) is consistently higher than the 6 MV dose (dashed line), indicating higher dose deposition at this position for the higher energy. At P2 (dashed green lines): The 6 MV dose (dashed) shows a more noticeable increase between 15×15 and 20×20 field sizes, while 15 MeV (solid) has a steadier trend, with a small but consistent rise. And at P3 (purple lines), Doses are generally lower than at P1 and P2. Both energies show a gradual increase in dose as the field size increases, but the rise is more significant for the 6 MV dose.

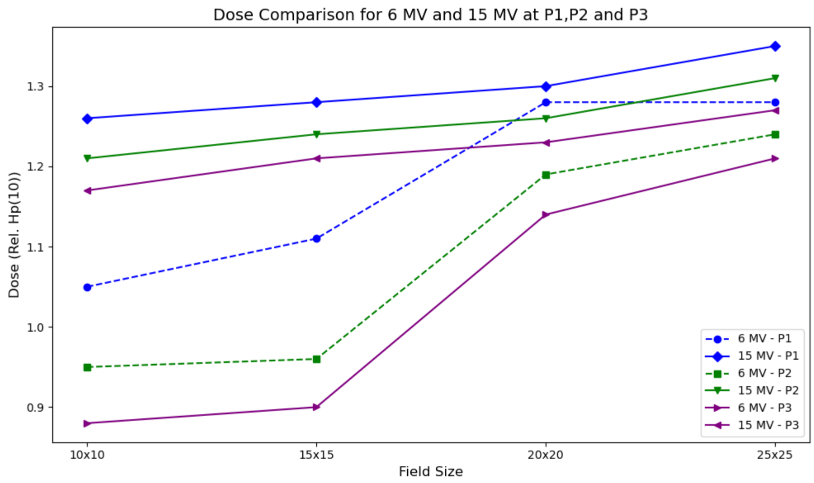

Fig 3: *The line graph compares Relative Hp(10) doses for 6 MV and 15 MV radiation energies at three positions (P1, P2, and P3) across different field sizes (10×10, 15×15, 20×20, and 25×25)*

P1 is likely closer to the high-dose region, indicating this position is subject to the most radiation. P2, being at the center, experiences a more uniform distribution of dose. P3 is farther away, resulting in lower doses compared to P1 and P2. Larger field sizes (20×20 and 25×25) generally result in higher doses at all positions and energies, with more significant differences at 6 MV. For 6 MV at P2 and P3, there's a sharp rise in dose between 15×15 and 20×20, showing a non-linear response to field size changes. The field size significantly influences the dose, particularly for 6 MV radiation at P2 and P3.

This graph likely highlights how field size and energy level affect radiation dose distribution at different points, which is important in dosimetry and treatment planning.

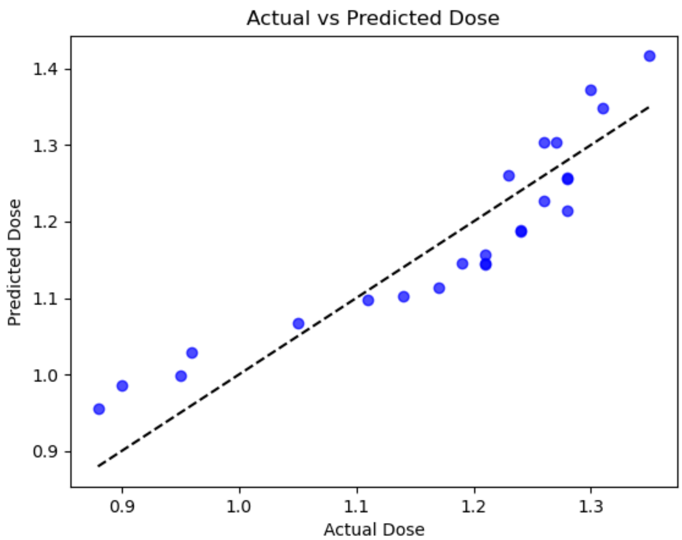

Fig 4: *The regression analysis of actual dose vs. predicted dose*

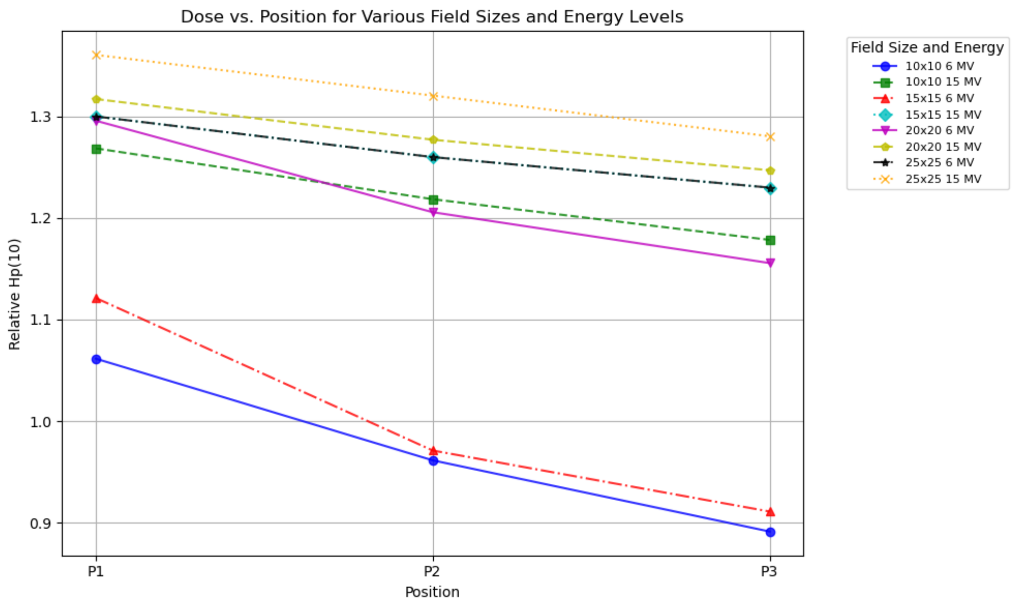

Fig 5: *Percent depth dose (PDD) for different field sizes and energies to understand how these factors influence relative Hp(10) in dosimetric measurements*

From Fig. 5, the PDD curve generated from the dataset offers several key insights into how field size, energy, and position affect relative Hp(10) measurements. Figure 5 shows energy dependence on 15 MV Photon Fields consistently show higher relative Hp(10) values compared to 6 MV fields across all positions and field sizes. Since 15×15 for 15 MV and 25×25 for 25 MV overlap with each other due to similar data points. This suggests that higher energy beams (15 MV) deposit more dose at the measurement positions compared to lower energy beams (6 MV), which is consistent with the deeper penetration capability of higher-energy photons. To determine the field size dependence in both energy levels, as the field size increases (from 10×10 cm² to 25×25 cm²), the relative Hp(10) values increase, especially at P1 and P2. Larger fields provide more uniform radiation distribution, leading to higher and more consistent doses across positions, as observed from the flatter curves for larger fields. The dose variation is more pronounced in smaller fields (e.g., 10×10 cm²), where P1 and P3 exhibit greater deviation from P2 (center), indicating that smaller fields have greater dose inhomogeneity, especially at the edges of the field.

To determine position dose variation, P2 which lies at the center consistently exhibits lower variability compared to P1 (right) and P3 (left), reflecting the fact that the center of the beam receives a more uniform dose (P1 and P3), particularly in smaller fields, show more variation, with P3 (left) generally receiving a lower dose compared to P1 (right), indicating an asymmetry in dose distribution at the edges of the field. The larger fields (15×15 cm² to 25×25 cm²) show improved uniformity across all positions, with smaller dose differences between P1, P2, and P3.

The higher uncertainty in smaller fields and peripheral positions (especially at P3) is visually reflected by the steeper slope for smaller fields, indicating greater positional sensitivity and dose variation. Larger fields and higher energies exhibit reduced uncertainty and more consistent dose delivery across all positions, as evidenced by the flatter curves, especially for P1 and P2.

- Higher photon energy (15 MV) results in higher and more uniform dose distributions compared to **6 MV**.
- Larger field sizes significantly reduce dose variability, creating more homogeneous radiation fields, which is particularly important for minimizing over- or under-dosing in treatment areas.
- Smaller fields should be used with caution, as they introduce more variability at non-central positions, increasing the risk of uneven dose distribution, especially at the edges of the field.

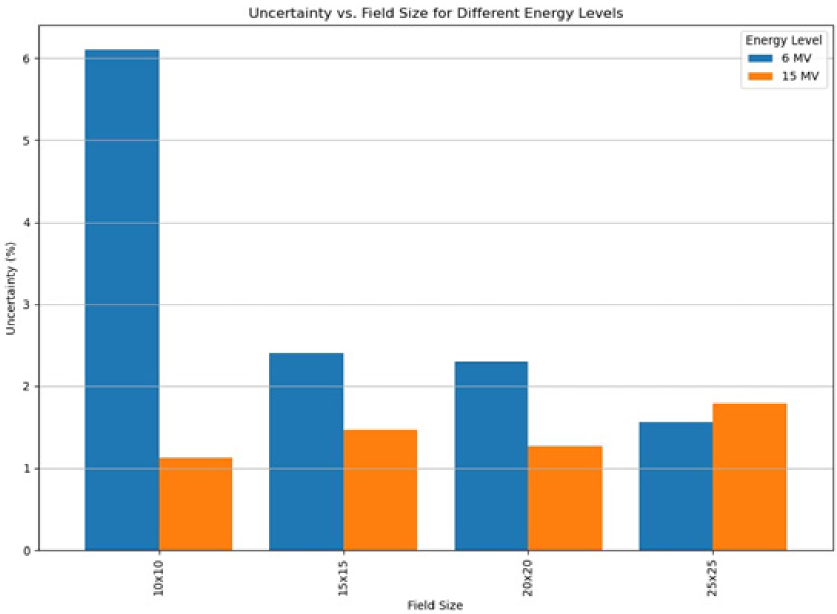

Fig 6: *The relationship between uncertainty vs field size for different energy levels.*

From Fig. 6**,** the uncertainty for each measurement was calculated using the relative standard deviation formula. The uncertainty for Energy Level 6 MV is particularly high at the 10×10 field size is around (6%), whereas Energy Level 15 MV shows a much smaller uncertainty of around (~1%) at the same field size. This could indicate that smaller field sizes are more sensitive to variations or external factors, particularly at lower energy levels. For 15 MV measurements, the uncertainties are notably lower (< 2%), especially for larger field sizes. This suggests better stability and reduced variation in the dosimetric readings at higher energy levels.

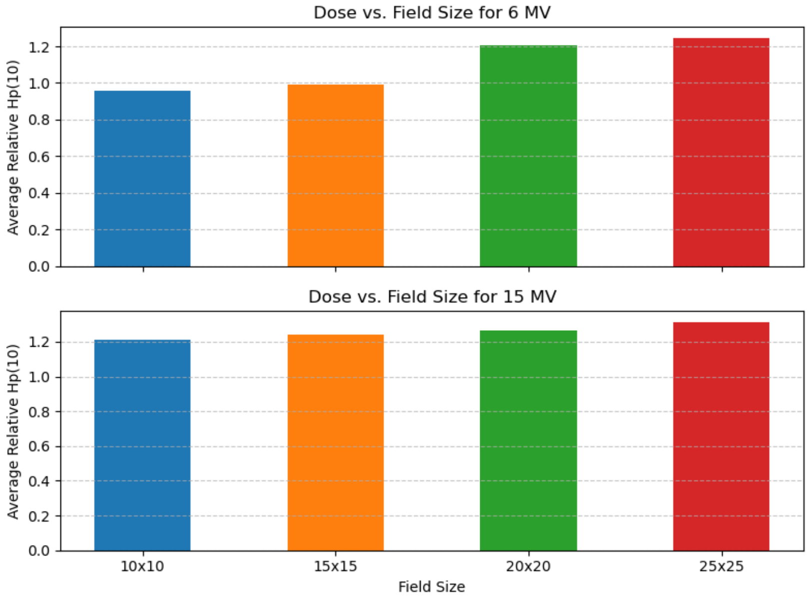

Fig 7: *Average relative dose (Hp(10)) vs. field size at 6 MV and 15 MV energy levels*

From Fig. 7, as the field size increases from 10×10 to 25×25 concerning 6 MeV energy, the average relative dose increases. At 10x10, the relative dose is just below 1.0. And that of 25×25, the dose is just above 1.2. There is a notable increase in dose as the field size increases, suggesting that the 6 MV energy level becomes more effective or intense with larger fields.

For 15 MV, the dose values are relatively consistent across all field sizes. The relative dose remains near or slightly above 1.2 for all field sizes (10×10, 15×15, 20×20, and 25×25). This suggests that the 15 MV energy level provides a stable dose output regardless of field size, indicating less sensitivity to changes in field size compared to 6 MV.

4. DISCUSSION

From Fig. 3, at P1 (dashed blue lines): Both energies show increasing doses as the field size increases. However, the 15 MV dose (solid line) is consistently higher than the 6 MV dose (dashed line), indicating higher dose deposition at this position for the higher energy. At P2 (dashed green lines): The 6 MeV dose (dashed) shows a more noticeable increase between 15×15 and 20×20 field sizes, while 15 MeV (solid) has a steadier trend, with a small but consistent rise. And At P3 (purple lines), Doses are generally lower than at P1 and P2. Both energies show a gradual increase in dose as the field size increases, but the rise is more significant for the 6 MV dose.

P1 is likely closer to the high-dose region, indicating this position is subject to the most radiation. P2, being at the center, experiences a more uniform distribution of dose. P3 is farther away, resulting in lower doses compared to P1 and P2.

Larger field sizes (20×20 and 25×25) generally result in higher doses at all positions and energies, with more significant differences at 6 MV. For 6 MV at P2 and P3, there's a sharp rise in dose between 15×15 and 20×20, showing a non-linear response to field size changes. The field size significantly influences the dose, particularly for 6 MV radiation at P2 and P3.

This graph likely highlights how field size and energy level affect radiation dose distribution at different points, which is important in dosimetry and treatment planning.

The data suggests that both field size and energy level significantly impact the relative Hp (10) and the associated uncertainties. The central axis (P1) consistently records higher dose values, reflecting the expected dose distribution profile in therapeutic beams. Larger field sizes tend to exhibit more variation in Hp (10) across different positions due to the spread of the beam and increased scatter, particularly at lower energy levels.

The higher uncertainty at position P3 for 6 MV and larger field sizes may be attributed to edge effects, where the dosimeter is exposed to a region of rapidly changing dose gradients. In contrast, measurements at 15 MV show lower uncertainties, potentially due to the more uniform dose distribution associated with higher energy photon beams.

Understanding the variation in Hp (10) across different field sizes and energies is crucial for both radiation protection and therapy planning. The findings of this study suggest that while uncertainties remain low overall, particular attention should be paid to off-center positions, especially when using lower energy levels. The Hp (10) measurements at higher energy levels are more consistent, supporting their use in situations requiring higher accuracy. Higher photon energy (15 MV) results in higher and more uniform dose distributions compared to 6 MV**.** Larger field sizes significantly reduce dose variability, creating more homogeneous radiation fields, which is particularly important for minimizing over- or under-dosing in treatment areas. Smaller fields should be used with caution, as they introduce more variability at non-central positions, increasing the risk of uneven dose distribution, especially at the edges of the field.

5. CONCLUSION

The findings underline the vital role that these parameters play in determining the accuracy and consistency of dose delivery, particularly in clinical radiotherapy and radiation protection settings. It was observed that larger field sizes generally contributed to more uniform dose distributions, especially at the central position (P2), which showed the least variability across different configurations. Conversely, peripheral positions (P1 and P3) exhibited higher uncertainty levels, with the most significant variations occurring at smaller field sizes and lower energy levels, and as the field size increases, scattered dose also increases. These observations highlight the potential risks of under- or overdosing in off-center positions when using narrow beams or lower energy settings.

Moreover, the results demonstrated that higher energy photons produced more stable and homogeneous dose distributions across all positions and field sizes, suggesting their suitability for treatment scenarios demanding higher precision and deeper tissue penetration.

Overall, this work contributes valuable insights into the optimization of dosimetric practices.

ACKNOWLEDGEMENT

The authors would like to express their sincere gratitude to the Central Department of Physics, Tribhuvan University, for providing the academic support. Special thanks are extended to Bhaktapur Cancer Hospital for facilitating the experimental setup and for their valuable technical assistance throughout the dosimetric measurements. We are also grateful to the Physical Science Laboratory at the Nepal Academy of Science and Technology (NAST) for the instrumental support and collaboration.

REFERENCES

Almond, Peter & Biggs, Peter & Coursey, B.M. & Hanson, W & Huq, M. Saiful & Nath, Ravinder & Rogers, D. (1999). AAPM's TG-51 protocol for clinical reference dosimetry of high-energy photon and electron beams. Medical physics. 26. 1847-70. DOI: 10.1118/1.598691 PMID: 10505874

Andreo, Pedro & Burns, D.T. & Hohlfeld, K. (2004). Absorbed dose determination in external beam radiotherapy: an international code of practice for dosimetry based standards of absorbed dose to water. IAEA TRS-398. 66-81.

Bolt, M., Clark, C. H., Nisbet, A., & Chen, T. (2021). Quantification of the uncertainties within the radiotherapy dosimetry chain and their impact on tumor control.Physics and imaging in radiation oncology, 19, 33–38. DOI: 10.1016/j.phro.2021.06.004 PMID: 34307916 PMCID: PMC8295844

Castro, P., García-Vicente, F., Mínguez, C., Floriano, A., Sevillano, D., Pérez, L., & Torres, J. J. (2008). Study of the uncertainty in the determination of the absorbed dose to water during external beam radiotherapy calibration. Journal of Applied Clinical Medical Physics, 9(1), 70–86. DOI: 10.1120/jacmp.v9i1.2676 PMID: 18449162 PMCID: PMC5721533

Farrance, I., & Frenkel, R. (2012). Uncertainty of Measurement: A Review of the Rules for Calculating Uncertainty Components through Functional Relationships. The Clinical Biochemist. Reviews, 33(2), 49–75.

Frane N, Bitterman A. Radiation Safety and Protection. [Updated 2023 May 22]. In: StatPearls [Internet]. Treasure Island (FL): StatPearls Publishing; 2024 Jan-. Available from: https://www.ncbi.nlm.nih.gov/books/NBK557499/

Ghorbani, Mojtaba & Tabatabaei, Z & Vejdani, Atefeh & Vosoughi, Habibeh & Knaup, C. (2015). Effect of Tissue Composition on Dose Distribution in Electron Beam Radiotherapy. Journal of biomedical physics & engineering. 5. 15-24.

Jaffray, D. A., & Gospodarowicz, M. K. (2015). Radiation therapy for cancer. In The World Bank eBooks (pp. 239–247). DOI: 10.1596/978-1-4648-0349-9_ch14 PMID: 26913334

Kry, S. F., Smith, S. A., Weathers, R., & Stovall, M. (2012). Skin dose during radiotherapy: a summary and general estimation technique. Journal of Applied Clinical Medical Physics, 13(3), 3734. DOI: 10.1120/jacmp.v13i3.373 PMID: 22584171 PMCID: PMC5716567

Measurement and error analysis. (n.d.). https://www.webassign.net/question_assets/unccolphysmechl1/measurements/manual.html

Yoder, R. C., Dauer, L. T., Balter, S., Boice, J. D., Jr, Grogan, H. A., Mumma, M. T., Passmore, C. N., Rothenberg, L. N., & Vetter, R. J. (2022). Dosimetry for the study of medical radiation workers with a focus on the mean absorbed dose to the lung, brain, and other organs. International journal of radiation biology, 98(4), 619–630. DOI: 10.1080/09553002.2018.1549756 PMID: 30451566 PMCID: PMC9465996

Report of *Phakopsora nishidana* (rust) Parasitic on *Ficus religiosa*, in Nepal

Mahesh Kumar Adhikari[1*], Yoshitaka Ono[2] and Mary Catherine Aime[3]

[1] G . P. O. Box. no. 21758, Kathmandu , Nepal
[2] University of Tsukuba, Laboratory of Plant Parasitic Mycology, Tsukuba, Japan
[3] Department Botany Path.Aime Lab, Purdue University, U.S. A

***CORRESPONDING AUTHOR:**

Mahesh Kumar Adhikari
Email: mahesh.kamalaadh@gmail.com

ISSN : 2382-5359(Online), 1994-1412(Print)

DOI: https://doi.org/10.3126/njst.v22i2.100108

Date of Submission: 31 Dec, 2025

Date of Acceptance: 27 May, 2026

ABSTRACT

During the regular survey of parasitic fungi in and around Kathmandu valley, a rust fungus was incidentally collected. Later it was identified as *Phakopsora nishidana* S. Ito (a rust fungus) found parasitic on *Ficus religiosa* L. (Peepal tree). The material was gathered from Lainchour, Kathmandu, Nepal. Among the rust fungus prevailing in Nepal, it is the first report of *Phakopsora nishidana* S. Ito (family Phakopsoraceae of Pucciniales order) parasitic on Ficus religiosa L. (a fig family plant).

Key words: Rust, Geographic distribution, Himalaya, Nepal, New record

1. INTRODUCTION

Nepal situated in the lap of the central Himalaya, embraces broad range of many interesting mycodiversity under its six diverse topographical and climatic zones. It is the zone of immense biodiversity, dominance, dynamics and the center for origin of Himalayan fungi. It stills needs more exploration and investigation on mycoflora in future also. In addition to diverse indigenous plants, numerous alien species have invaded naturally and or introduced for commercial purposes.

The present paper deals with *Phakopsora* (a rust fungus) which falls under the family Phakopsoraceae of Pucciniales (Kirk *et al, 2008* and *Species Fungorum* (2022).

Previously the rust fungi on *Ficus religiosa* (peepal tree) was known to be caused by the traditionally named *Cerotelium fici,* but the recent molecular studies have identified that *Phakopsora nishidana* is a significant, and perhaps more common, agent of fig rust (specifically on *Ficus carica* and related species). This rust infects several *Ficus* species, including *Ficus religiosa, Ficus benghalensis* and *Ficus carica.* It is characterized by small, spots on the upper leaf surface and rust-colored pustules on the lower surface. The infection often causes chlorosis, necrosis, and premature defoliation. (Boshoff *et al,* 2022). The causal agent of rust on figs in New Zealand was determined using molecular and morphological analyses to be *Phakopsora nishidana* S. Ito and not *Cerotelium fici* (Padamsee & McKenzzie 2024).

Ficus religiosa L.is distributed in Eastern Himalaya (Bangladesh, Bhutan, Nepal, India, Pakistan), the Nicobar Islands, Thailand, Myanmar, and Peninsular Malaysia.

The checklist of rust fungi reported from Nepal record eight species of *Phakopsora* by different authors. But none of the following paper record the present rust on *Ficus religiosa* (Ono *et al,* 1995). They are as follows: *Phakopsora ampelopsidis* Diet. & Syd., on *Parthenocissus semicordata* (Durrieu, 1980; Ono *et al,* 1990); *P. artemisiae* Hirats., on *Anaphalis busua* (Durrieu, 1980; Ono, *et al,*, 1990), *A. margaritacae,* A. *triplinervis* and *Artemisia* sp. (Ono *et al,*1990); *P. cronartiformis* Diet. on *Parthenocissus semicordata* (Durrieu, 1980; Ono *et al,*1990)*; P. gossypii* (Arth.) Hirats. f., on *Gossypium arboreum* (Manandhar, 1977); *P. incompleta* (Syd. & Syd.) Cumm., on *Microstegium ciliatum* (Durrieu, 1980; Ono *et al,* 1990) *M. nudum, Microstegium* sp and *M. viminium* (Ono *et al,*1990); *P. meliosmae* Kusano, on *Meliosma dilleniifolia* (Durrieu, 1980; Ono *et al,* 1990) and *M. pungens* (Durrieu, 1980); *P. pachyrhizi* Syd. & Syd., on *Amphicarpaea ferruginea* (Ono *et al,* 1990) and *Glycine max* (Manandhar, 1977; Singh, 1968; Ono *et al,*, 1990)*; P. punctiformis* (Barcl. et Diet.) Diet., on *Galium asperifolium* (Durrieu, 1980) and *Rubia manjith* (Drrieu, 1987).

2. MATERIAL AND METHOD

During the course of investigation of parasitic fungi, a rust parasitic on *Ficus religiosa was* gathered at Lainchour, Kathmandu. Photograph was taken and the study was done in the laboratory under microscopic power of 10 x 10 and 40. The identification of the material was done in Japan (Y. Ono), at University of Tsukuba, Laboratory of Plant Parasitic Mycology, and Aime Mycology Lab at Purdue University, U.S. A. The scanning microphotograph was done in Japan [Olympus BX 51 equipped with differential interference contrast (DIC) equipment and Olympus DP21 digital camera (Olympus, Tokyo, Japan)]. The specimen has been deposited in National Herbarium and Plant Laboratory, Godavary, Lalitapur, Nepal.

3. DESCRIPTION

Phakopsora nishidana S. Ito, (1938) *Transactions of the Sapporo Natural History Society* 15 117 (1938); Padamsee, & McKenzie, 2024 *Phakopsora nishidana* is the causal agent of rust on figs in New Zealand, *Australasian Plant Disease…* DOI:10.1007/s13314-024-00528-3

Upper leaf surface: Initial symptoms appear as small, yellow or tan flecks and then develop into brown that may merge to form larger necrotic areas. Lower leaf surface: raised, bright rusty pustules (uredinia) form the underside of the leaves. These pustules contain the urediniospores. The hypophyllous uredinia were surrounded by necrotic leaf tissue, visible as dark brown to black spots on upper leaf surfaces. The hypophyllous uredinia were scattered often on reddish brown angular leaf spots.pale reddish brown, circular, up to 0.5 mm diam. with a few inconspicuous, hyaline, thin-walled, cylindric to clavate paraphyses. Urediniospores 20–32 × 15.–21 µm, globose, obovoid, ellipsoidal or angular, contents very pale yellow; wall 0.5–1 µm thin, very pale yellow or hyaline, sparsely echinulate, germ pores obscure. Telia not known in Nepal.

Specimen examined - *Ficus religiosa* L.,Lainchour, 2082 6.28 (14, Oct, 2025), No 2092.8 (NHPL, Kath) **(Fig. no 1- 6)**

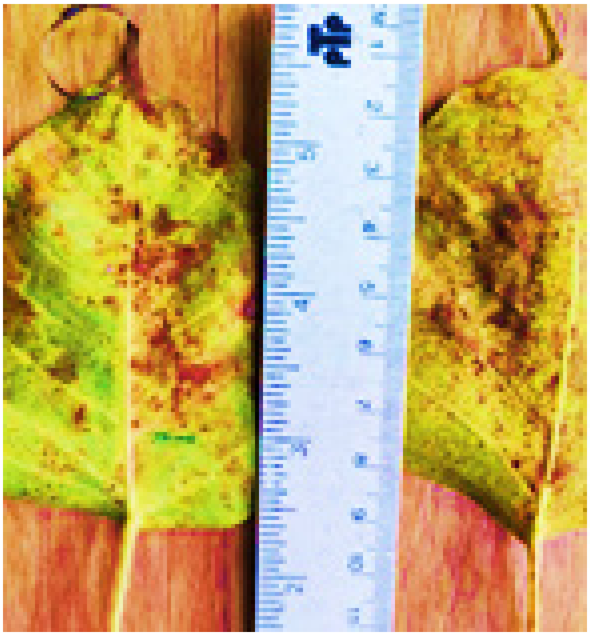

Fig 1: *showing Phakopsora sp. on Ficus religiosa.*

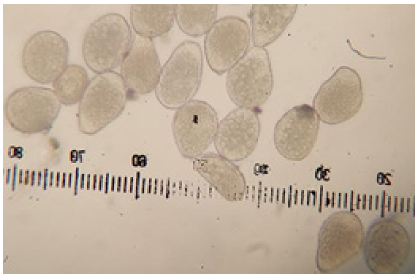

Fig 2: *Urediniospores*

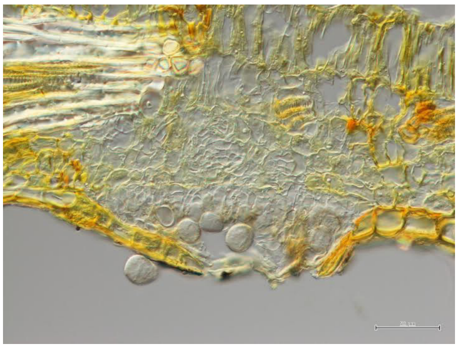

***Fig 3:** SEM section through leaf*

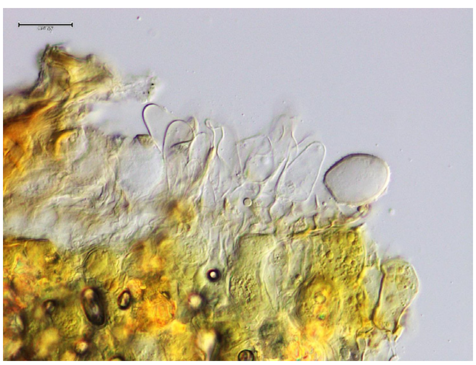

***Fig 4:** showing Phakopsora sp.with thin-walled paraphyses and uredinia at hymenia and margin.*

Fig 5 and 6: *Urediniospores*

4. DISCUSSION

Phakopsora nishidana has been confirmed from South Africa and New Zealand, Two recent publications, one focusing on *C. fici* on *Morus nigra* (mulberry) and another on *Phakopsora nishidana* S. Ito (Ito and Homma 1938) on *F. carica* (Boshoff *et al.* 2022), raised the question whether the rust on figs in New Zealand was *C. fici*. The DNA sequencing and the measurements of the urediniospores in *P. nishidana* in South Africa (SA) matched that of those reported for *C. fici* from Brazil but the urediniospores of the rust on *Ficus* in New Zealand, were (19.5–) 24–30 (–35) x (14–)16–20 (–22) µm, globose, obovoid, ellipsoidal or angular, wall 0.5–1 µm thick, pale, sparsely echinulate, germpores obscure in current collections, (3–4) and equatorial (Boshoff *et al.* 2022; Padamsee & McKenzie, 2024).

ACKNOWLEDGEMENT

The authors are thankful to Dr. Hnry Van T. Cotter (USA), W Maplehurst St Ferndale Michigan, USA for his kind help.

REFERENCES

Boshoff W. H. P,,Visser, B., Bender, C. M,, Wood, A. R., Rothmann, L. , Wilson, K, Hamilton-Attwell V. L, Pretorius, Z. A (2022) Fig rust caused by *Phakopsora nishidana* in South Africa. *Phytopathol Mediterr* 61:283–298 DOI: 10.36253/phyto-13034

Durrieu, G. (1980) Uredinales du Nepal.*Cryptog, Mycol*. 1 : 33-68. DOI: 10.5962/p.354075

Ito, S. and Homma, Y. (1938) Notae mycologicae Asiae orientalis. III. *Trans. Sapporo. Nat. Hist. Soc.* 15:113–128

Kirk P. M,, Cannon P. F, Minter D. W, Stalpers J. A (2008). *Dictionary of the Fungi (10th ed.)*. Wallingford, UK: CABI. p. *519*. *ISBN 978-0-85199-826-8*.

Manandhar, K. L. 1977 Some rust fungi in Nepal. *Jour. Nat. Hist. Mus.* 1 : 237-242.

Ono, Y., Adhikari, M. K. and Rajbhandari, K. R. (1990) Uredinales of Nepal. *Rept. Tottori Mycol. Inst.* 28 : 5775.

Ono, Y., Adhikari, M. K. and Kaneko, R. (1995) An annotated list of the rust fungi (Uredinales) of Nepal. *Cryptogams of the Himalayas.* vol. 3 *Nepal and Pakiistan.* Eds, M. Watanabe and H. Hagiwara, National Science Museum, Tsukuba, Japan. 69 -125.

Padamsee, M and McKenzie, E. H. C. (2024) *Phakopsora nishidana* is the causal agent of rust in figs in New Zealand, *Auatralin Plant Disease Notes*. 19: 3
DOI: 10.1007/s13314-024-00528-3

Species Fungorum, Names Record". *www.speciesfungorum.org. Retrieved 3 November 2022.*

Arsenic Concentration in Public Wells Around the Ring Road in Kathmandu Metropolitan City, Nepal

Aashish Shiwa[1] and Indira Parajuli[2,3*]

[1] Department of Environmental Science, Tri-Chandra Multiple Campus, Tribhuvan University, Nepal
[2] Central Department of Environmental Science, Tribhuvan University, Nepal
[3] Nepal Academy of Science and Technology, kumaltar, Lalitpur, Nepal

***CORRESPONDING AUTHOR:**

Indira Parajuli
Email: parajuli_indira2000@yahoo.com

ISSN : 2382-5359(Online), 1994-1412(Print)

DOI:
https://doi.org/10.3126/njst.v22i2.100109

Date of Submission: 05 Oct, 2024

Date of Acceptance: 20 Dec, 2025

ABSTRACT

An estimated 110 million people across South and Southeast Asia—including the Kathmandu valley and Terai region of Nepal—are susceptible to arsenic contamination. To assess the current levels of arsenic in shallow public wells (1–30m depth), this study was conducted in February 2022 with in the ring road area of Kathmandu Metropolitan City. Eleven water samples (n=11) were collected from the wells selected through simple random sampling. Arsenic concentrations were analyzed using Continuous Hydride Generation Atomic Absorption Spectrophotometry (HG-AAS). Results revealed arsenic levels below the detectable limit (<0.005 mg/L) in all samples, well within Nepal's permissible limit of 0.05 mg/L. These findings indicate no immediate arsenic-related health risk from the shallow public wells examined. However, prior research has documented significant arsenic pollution in the deep aquifers of the Kathmandu Valley, which is hydrologically distinct from the shallow groundwater sources sampled. Despite known risks of chronic arsenic exposure, including cancer, infertility, and developmental impairments, 84.61% of respondents were unaware of arsenic and its potential health impacts. This necessitates urgent public awareness and education.

Keywords: *Arsenic, Groundwater, Kathmandu valley, Health hazard, Public well.*

1. INTRODUCTION

Arsenic-laden groundwater has been a serious public health hazard worldwide for several decades. Though the most common metal pollution in freshwater is from mining industries, groundwater's primary source of arsenic (As)—a poisonous metalloid of the nitrogen family—is mostly geogenic (Rasaili et al., 2024). Arsenic is mobilized through the dissolution of arsenic-rich geological materials, particularly via oxidation of As-containing sulfides, desorption from oxide and hydroxide, and leaching of arsenic from sulfide bicarbonate (Nickson et al., 2000; Stolze et al., 2022). In groundwater systems, arsenic is typically present in inorganic form—arsenite (As(III)) or arsenate (As(V)) oxyanions. In oxygen-rich groundwater, arsenate is dominant, whereas arsenite is more likely to be found under reducing conditions. The higher toxicity of trivalent arsenic, As(III), relative to pentavalent arsenic, As (V), is associated with its greater solubility and mobility, which enhances its bioavailability and cellular uptake (Valskys et al., 2022). Given the well-established toxicity of arsenic, a significant disparity exists in the regulatory limits for arsenic in drinking water: the World Health Organization (WHO) guideline is 0.01 mg/L (WHO, 2008), while the enforceable National Drinking Water Quality Standards of Nepal (NDWQS) remain at 0.05 mg/L (NDWQS, 2022).

Globally, an estimated population of 220 million people are vulnerable to groundwater arsenic contamination, with chronic exposure affecting approximately 100 million (Podgorski & Berg, 2020). Regions of South and Southeast Asia, including Bangladesh, India and Nepal, are particularly affected. High arsenic concentration has been reported in Australia (0.005-300 mg/L), Canada (0.0015-100 mg/L), Bangladesh (0.002-4.73 mg/L), and India (0.001-3.88 mg/L) (Chaudhary et al., 2024). In West Bengal, 30 million people living in six districts covering 34,000 km^2 are affected by arsenic, and over 800,000 inhabitants from 312 villages consume arsenic-contaminated groundwater (Bhat & Bhat, 2020).

Arsenic is a significant problem in the potable water distribution system in Nepal's Terai region, as most shallow tube wells contain a high concentration of naturally occurring arsenic, exceeding the safer limit set for drinking purposes (Lamichhane & Singh, 2019; Mueller, 2020; Rasaili et al., 2024). However, groundwater serves as the principal drinking water source for 90% of the inhabitants in this region (Lamichhane & Singh, 2019; WHO & NHRC, 2009). As per reports, Rupandehi has the highest arsenic concentration (2.62 mg/L), accompanied by Nawalparsi (1.828 mg/L), Rautahat (1.007 mg/L), Kapilvastu (1 mg/L), and Parsa (0.456 mg/L) (NASC and ENPHO, 2004; Ogata & Suenaga, 2023; Rasaili et al., 2024). Epidemiological surveys in Nepal's Terai districts reveal a tiered pattern of arsenic exposure: approximately half a million residents are acutely exposed (>0.05 mg/L), while around 3.5 million (31%) experience chronic exposure within the 0.01-0.05 mg/L range. Approximately 80% of inhabitants in this region have been reported to suffer from arsenic-induced skin manifestations, with arsenicosis reported to be twice as prevalent in males as in females (Maharjan et al., 2005). In the Nawalparasi district alone, 60% of the inhabitants suffered from arsenicosis (Rasaili et al., 2024).

The arsenic-bearing quaternary sediments serve as the primary reservoir for groundwater arsenic contamination in the Kathmandu Valley (Gurung et al., 2007; Rasaili et al., 2024). Shrestha et al. (2013) reported that arsenic displays pronounced spatial variability, with significantly elevated concentrations in the Central Groundwater District (CGWD) within the Kathmandu basin. Given that groundwater is a principal water source used by 52% of households across the Kathmandu region, residents relying on the CGWD face heightened risks of arsenic-induced morbidities (Gwachha et al., 2020; Shrestha et al., 2018). The arsenic concentration and depth of groundwater have a positive correlation (Banson et al., 2020; JICA and ENPHO, 2005; Maharjan et al., 2009). Monitoring of 122 deep tube wells revealed seasonal variation in arsenic violations, with exceedance rates decreasing from 13.1% pre-monsoon to 8.2% monsoon ($p<0.05$), relative to the 0.05 mg/L NDWQS threshold (Maharjan et al., 2009). 2020 monitoring ($n=20$) revealed widespread arsenic contamination, with 76.2% of samples exceeding the WHO threshold (0.01 mg/L), and 47.6% violating the NDWQS standard (0.05 mg/L) (Gwachha et al., 2020). Longitudinal studies conducted in the Kathmandu Valley between 2002 and 2022 documented wide variability in arsenic concentrations. Reported values include 0.0738 mg/L (Khatiwada et al., 2002), 0.019 mg/L (Gurung et al., 2006), 0.100 mg/L (Bajracharya et al., 2007), 0.021 mg/L (Warner et al., 2008), 0.265 mg/L (Maharjan et al., 2009), 0.073 mg/L (Chapagain et al., 2009), 2.070 mg/L (Emerman et al., 2010), 0.143 mg/L (Shrestha et al., 2013), 2.8 mg/L (Gwachha et al., 2020), and 0.071 mg/L (Sarkar et al., 2022).

Arsenic is poisonous, and short-term exposure to arsenic causes arsenicosis—a severe environmental chemical disease—while continuous exposure causes peripheral vascular disease, diabetes mellitus, neurotoxicity, nephrotoxicity, skin lesions, Blackfoot disease, hypertension, and a high risk of different types of cancers (Mueller, 2021; Rasaili et al., 2024). Arsenic contamination also induces genotoxicity and causes the development of vascular diseases such as stroke and ischemic heart disease. The Food and Drug Administration (FDA) and the International Agency for Research on Cancer (IARC) classify arsenic as a known human carcinogen, with conclusive evidence of well-documented associations with cancers of the bladder, pulmonary system, renal organs, and hepatic tissues.

Switching shallow groundwater wells and implementing rainwater harvesting are commonly adopted mitigation strategies; however, to further minimize the health risk, the engineered treatment of arsenic-contaminated water—using methods such as reverse osmosis, ultrafiltration, distillation, or ion exchange—remains an effective and sustainable option. Various arsenic removal techniques have proven effective, including phytoremediation, coagulation-flocculation, oxidation—such as photochemical, photo-catalytic, biological, and in-situ oxidation—as well as electro-coagulation, adsorption (activated alumina,iron-based sorbent, and zero-valent iron), ion exchange, and nanoparticles and nano-engineered adsorbents have shown considerable potential (Hassan, 2023; Rasaili et al., 2024).

According to the annual report of Kathmandu Upatyaka Khanepani Limited (KUKL), only 240.02 million liters per day (MLD) of water is supplied to meet a total demand of 506 MLD, with 25.95 MLD sourced from groundwater (KUKL, 2024). Various sources, including public wells, compensate for the deficit of 265.98 MLD, and the exact data are unknown. Despite the substantial contribution of shallow aquifers to municipal water provision in the Kathmandu Valley, most hydrogeological investigations have concentrated exclusively on deeper aquifer systems. Although public wells play a critical role in Kathmandu Valley's water supply, no systematic investigation has assessed their arsenic contamination status. This study addresses this research void by (1) quantifying arsenic levels across shallow public wells and (2) evaluating associated health risks. This study establishes critical baseline data while significantly advancing understanding of arsenic contamination of groundwater and its linked public health risks in the region.

2. MATERIALS AND METHODS

2.1 Study area and sampling sources

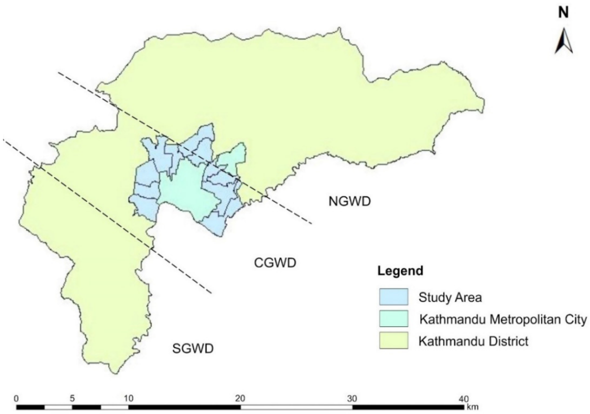

Source: JICA, 1990

Fig 1: GIS map showing the study area within the ring road of Kathmandu Metropolitan City

This study focused on areas within the ring road of the Kathmandu Metropolitan City (27°71›72››N, 85°32›40''E), Kathmandu District, Bagmati Province, Nepal. The study area spans approximately 49.45 km² and receives an annual average precipitation of 1,742 mm (Department of Hydrology and Meteorology (DHM), 2023). While the valley's mean annual temperature (17.6°C) aligns with subtropical highland norms, its extreme precipitation seasonality (80% monsoon concentration) creates marked hydrological contrasts between wet and dry periods. The Kathmandu Metropolitan City consists of 32 administrative wards, and those located along the ring road—Kalanki, Kalimati, Dallu, Shorakhutte, Lainchour, Maharajgunj, Baluwatar, Mitrapark, Pashupati, Gausala, and Koteshowr, were included in this study.

Kathmandu Valley is categorized into three Groundwater Districts (GWD) based on hydrogeological classification: Northern Groundwater District (NGWD), Central Groundwater District (CGWD), and Southern Groundwater District (SGWD), as illustrated in Fig. 1 (JICA 1990). The NGWD and CGWD are located within Kathmandu Metropolitan City. Notably, NGWD is the valley's sole groundwater recharge zone, with aquifer replenishment occurring exclusively through precipitation.

2.2 Data collection, water sampling, and preservation

Data collection and analysis for this study were conducted exclusively during the dry season, from January and February 2022. A dual-methods strategy was implemented, incorporating both qualitative and quantitative analysis. Data sources included field surveys, laboratory analysis of water samples, a structured questionnaire survey, and Key Informant Interviews (KIIs). The questionnaire was administered to 385 well users across all sites. Arsenic awareness was evaluated through multiple questions addressing familiarity with arsenic and knowledge of its health effects; respondents answering 'no' to all related questions were categorized as unaware. Verbal informed consent was obtained from all participants prior to data collection. KIIs were conducted with medical professionals at Tribhuvan University Teaching Hospital, Kathmandu's busiest public hospital. Participants for the KIIs were selected using snowball sampling, wherein each respondent referred to the next.

For water quality assessment, one shallow public well was randomly selected from each of the 11 administrative wards along the ring road, yielding 11 spatially representative samples (n=11). A 125 ml sample was collected in a high-density polyethylene (HDPE) bottle, acidified with 2 mL of concentrated hydrochloric acid (HCl), and stored in dark containers to prevent photochemical reactions. The samples were then transported to the Environment and Public Health Organization (ENPHO) in Kathmandu for arsenic analysis.

2.3 Sample analysis and calculation

The total arsenic concentration in water samples was quantified using a Continuous Hydride Generation Atomic Absorption Spectrophotometer (HG-AAS) at the ENPHO Research Laboratory. The instrument used for the analysis was the iCE 3300 AAS (Thermo Fisher Scientific, USA), which can detect arsenic in water at a minimum concentration of 0.005 mg/L. For the analysis, 50 mL of each water sample was placed in a 100 mL beaker, and then 5 mL of concentrated hydrochloric acid (HCl) was added. The solution was stirred thoroughly using a glass rod. Subsequently, 5 ml of potassium iodide (KI) solution was added, mixed well, and allowed to sit undisturbed for 30 minutes in a safe location. A blank solution was prepared using double-distilled water following the same procedure.

Following sample preparation, the arsenic concentration was measured directly using the HG-AAS system. The spectrophotometer reading (in mg/L) was then multiplied by the dilution factor to calculate the total arsenic concentration in the sample, following the standard procedure recommended by APHA, AWWA, and WEF (2017).

As (mg/L) = AAS reading (mg/L) × dilution time (df)…………………………………………..(i)

where,

As (mg/L) = Concentration of arsenic in milligrams per litre

AAS reading (mg/L) = Measured value from the Atomic Absorption Spectrometer in mg/L

df = Dilution factors used during sample preparation

3. RESULTS

Our preliminary survey identified 43 public wells distributed across 11 wards of the Kathmandu Metropolitan City, with depths varying between 1–30 meters, as indicated in Table 1.

Field assessment revealed that 23.26% of these wells were non-functional (dry), while 76.74% remained actively used by local communities. Among operational wells, six specific locations—Pepsicola, KMC (Sinamangal), Biswarup Forest (Pashupati), Nawali, Dhumbarahi, and Bohoratar— served as crucial drinking water sources for 13.95% of users. Conversely, 30.23% of wells were used exclusively for household chores. Seasonal analysis indicated significantly increased reliance on these wells for drinking and cooking purposes during dry periods.

The study documented 385 household users of these public wells, with usage patterns as follows: 36.88% for drinking, 38.18% for cooking, and 24.94% for cleaning purposes. Notably, despite this substantial dependence on groundwater resources, our survey revealed alarmingly low awareness levels, with only 15.39% of respondents demonstrating knowledge of potential arsenic contamination and its associated health risk. This disparity between usage rates and risk awareness highlights critical gaps in public health education regarding groundwater safety in urban Kathmandu.

Table 1: Details of public wells: location, longitude, latitude, depth (in meters), condition, and number of families using each well.

Ward/Location	Longitude	Latitude	Depth	Condition	No. of the family using well
Ward 14: Kalanki					
TU	85º17’29” E	27º40’54” N	3	Polluted	12
Shanti Rokka Dharmashala	85º17’54” E	27º40’54” N	9	Dry	N/A
Gangkhola**	85º17’22” E	27º41’11” N	7.5	Normal	15
Makalu	85º16’47” E	27º41’45” N	1.5	Polluted	N/A
Buddha Marg	85º17’03” E	27º41’39” N	6	Scarce	7
Gita Panchyam Marg	85º17’01” E	27º41’41” N	8.5	Scarce	5
Ward 13: Kalimati					
Dhaukhel**	85º18’08” E	27º41’56” N	3	Normal	15
Tarkeshowr	85º18’08” E	27º42’04” N	2	Polluted	N/A
Ward 15: Dallu					
Manjushree	85º17’11” E	27º42’50” N	10	Dry	N/A
Kimdol	85º17’34” E	27º42’52” N	N/A	Dry	N/A
Chamati**	85º17’43” E	27º43’01” N	2	Polluted	6
Chhauni	85º17’22” E	27º42’38” N	1	Dry	N/A
Ward 16: Shorakhutte					
Gaurishankar Temple	85º17’32” E	27º43’49” N	7	N/A	N/A
Kharibot**	85º17’34” E	27º43’53” N	3.5	Polluted	10
Bohoratar	85º17’40” E	27º44’14” N	N/A	N/A	N/A
Bohoratar Height	85º17’37” E	27º44’13” N	1.5	Normal	12
Balaju Height	85º17’50” E	27º44’04” N	1.2	Dry	N/A
NEA Balaju Station	85º17’44” E	27º43’35” N	2.5	Normal	4
Ward 32: Koteshowr					
Pepsicola**	85º21’41” E	27º41’26” N	30	Normal	15
Purano Sinamangal	85º21’24” E	27º41’15” N	9.5	Dry	N/A
Sinamangal	85º21’23” E	27º41’09” N	7	Normal	15
Jadibuti	85º21’10” E	27º40’48” N	10	Polluted	9
Ward 03: Maharajgunj					
Gajendra Basti**	85º19’58” E	27º44’13” N	6	Normal	12
Maharjan Nursery	85º19’52” E	27º43’83” N	3	Normal	35
Ward 04: Baluwatar					
Dhumbarahi A	85º20’41” E	27º43’51” N	1	Normal	45
Dhumbarahi B	85º20’41” E	27º43’51” N	0.7	Normal	
Dhumbarahi Marg	85º20’27” E	27º43’34” N	1	Normal	30
Tushaloohar Temple A	85º20’02” E	27º43’52” N	1	Normal	25
Tushaloohar Temple B	85º20’02” E	27º43’52” N	1.4	Normal	
Baluwatar A**	85º19’57” E	27º43’40” N	3	Normal	20
Baluwatar B	85º20’02” E	27º43’47” N	N/A	Dry	N/A
PanchaKanya	85º20’10” E	27º43’51” N	1.5	Polluted	N/A
Ward 07: Mitrapark					

Ganesh Temple**	85º20'41" E	27º42'58" N	6.8	Normal	10
Mirmirey	85º20'36" E	27º43'08" N	3.5	Dry	N/A
Bulbule	85º20'28" E	27º43'01" N	11	N/A	N/A
Ward 08: Pashupati					
Nawali**	85º20'33" E	27º42'40" N	9	Normal	40
Biswarup Forest	85º21'10" E	27º42'29" N	6	Normal	6
Kirateshowr	85º21'02" E	27º42'45" N	4	Normal	5
Ward 09: Gaushala					
KMC, Sinamangal**	85º21'13" E	27º41'42" N	1	Normal	25
Riverside, Sinamangal	85º20'59" E	27º41'42" N	1.7	Scarce	7
Ward 26: Lainchour					
Amrit Marg	85º18'45" E	27º42'57" N	N/A	Dry	N/A
Bhagwan Bahal	85º18'44" E	27º42'57" N	N/A	Dry	N/A
Kapurdhara**	85º18'56" E	27º43'24" N	N/A	N/A	N/A
** represents public wells selected for water sample collection using simple random sampling.					

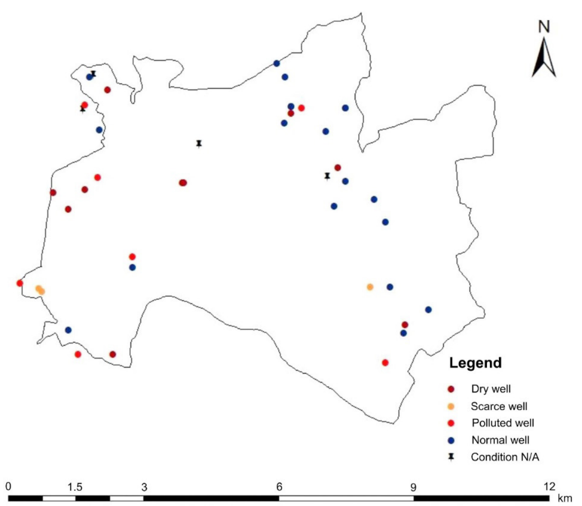

Fig 2: GIS map indicating the status of public wells in Kathmandu Metropolitan City, including conditions such as dry, scarce, and polluted wells.

3.1 Arsenic concentration in public wells

Analysis of water samples (n=11) revealed arsenic concentrations below the detection limit of 0.005 mg/L in all samples. These findings indicate an absence of arsenic pollution in the sampled wells at the time of testing.

3.2 Arsenic exposure, health impacts, and medical professionals

While no statistically significant health impacts from groundwater arsenic contamination were identified in this study, medical practitioners at TU Teaching Hospital report that approximately 5% of patients presenting with dermatological symptoms (itchy skin, sores, overnight blisters, and allergic reactions) were originate from agricultural places like Kavre palanchowk, where arsenic-containing pesticides may contribute to these clinical manifestations. Clinical experts confirm arsenic as an established public health hazard, with acute exposure (8–10 months) causing arsenic poisoning symptoms including nausea, abdominal pain, loss of appetite, diarrhoea, skin allergies, itching of the feet, abdomen, and limbs, and overnight blisters on the hands and skin. Chronic exposure is associated with severe consequences, including arsenic cancer and infertility in women and delayed physical and cognitive development in children. Additionally, chronic arsenic toxicity can impair vital organs, including the nervous system, kidneys, heart, and liver, and may manifest through damage to the skin, hair, and nails.

4. DISCUSSION

Kathmandu has experienced persistent water scarcity since the 1980s, with escalating severity in recent decades. Groundwater extraction supplies 50% of the valley's water demand, rising to 60-70% during dry periods (ICIMOD, 2007; Shrestha et al., 2023). This unsustainable reliance has led to severe aquifer depletion, with water table declining by 13-33 meters (1980-2000), 1.38-7.5 meters (2000-2008), and a projected decrease of 5.25-7.39 meters by 2050

(Lamichhane & Shakya, 2020). Over the last few decades, unprecedented groundwater extraction, coupled with inadequate recharge, exacerbated the crisis.

Our study of public wells revealed that 23.25% were completely dry, 6.98% were functionally scarce, and the remainder exhibited measurable annual decline in water levels due to uncontrolled urban expansion and minimal groundwater recharge. While groundwater is the key water source for 88% of the valley residents for bathing, only 3% utilize groundwater for drinking purposes (Shrestha et al., 2018). This stands in stark contrast to Nepal's Terai region, where approximately 90% of the population sources their potable water primarily from groundwater (WHO & NHRC, 2009; Lamichhane & Singh, 2019). Our data further delineates usage patterns among shallow public well consumers: 36.88% for drinking, 38.18% for domestic chores, and 24.94% exclusively for cleaning.

The absence of detectable arsenic in these shallow wells may be attributed to the prevalent oxidizing conditions, which immobilize arsenic through adsorption onto iron and manganese oxides. Conversely, deeper reducing aquifers, where arsenic is often reported, mobilize As(III), elucidating the disparity between shallow and deep groundwater arsenic levels. However, Shrestha et al. (2013) reported that 34% of the deep groundwater within the Kathmandu Valley surpassed the WHO threshold of 0.01 mg/L, while all shallow groundwater samples remained within acceptable limits. In contrast, Maharjan et al. (2009) identified that 11.4% of 149 shallow tube wells tested within the valley exceeded the WHO threshold, indicating localized variability. The highest recorded arsenic concentration in the valley was 2.8 mg/L (Gwachha et al., 2020).

This study is constrained by its limited sample size (n=11), single-season (dry period) sampling, and the absence of arsenic speciation. Arsenic concentrations are known to exhibit considerable spatiotemporal variability, influenced by seasonal hydrological fluctuations and geological heterogeneity. This necessitates spatiotemporally resolved monitoring designs to accurately characterize arsenic exposure risks across different seasons and hydrogeological settings.

In the Terai region, extensive testing conducted across 20 districts revealed that, out of 25,058 water samples, 23% had arsenic levels falling within the 0.01–0.05 mg/L range, and 8% exceeded 0.05 mg/L (NASC and ENPHO, 2004). Notably, 19 of these districts surpassed the NDWQS threshold. Rupandehi reported the highest arsenic concentration at 2.62 mg/L, followed by Nawalparsi (1.828 mg/L) and Rautahat (1.007 mg/L. By 2008, the blanket testing of 11,39,891 tube wells in Terai had identified 20,243 wells exceeding the NDWQS threshold, and 64,168 wells surpassing the WHO limits (WHO & NHRC, 2009).

A weak positive correlation between groundwater depth and arsenic concentration has been observed, suggesting that deeper aquifers may contain higher arsenic levels compared to shallow ones (Banson et al., 2020; JICA and ENPHO, 2005; Maharjan et al., 2009), which is consistent with the current study's findings. Despite the high literacy rate in Kathmandu, the adoption of safer water practices remains limited only 13% of residents use public wells for drinking, and merely 3.85% employ filtration systems to mitigate contamination. Furthermore, only 15.39% were found to be adequately informed and cautious regarding arsenic contamination. The discordance between high groundwater dependence and significantly low public awareness of arsenic (84.61% unaware) delineates considerable public health vulnerability. In the absence of detectable arsenic, this knowledge deficit nevertheless escalates exposure risk from coexisting contaminants and potential future deterioration of water quality. This awareness gap is likely to be more pronounced in the Terai region. Therefore, public education and targeted training initiatives play a critical role in minimizing the health risks posed by arsenic.

In the public wells of Kathmandu Metropolitan City, arsenic levels were found to be below the detectable limit, and no associated health impacts were reported. In contrast, the situation in Nepal's Terai region is significantly more severe. According to Maharjan et al. (2005), approximately 80% of the population in the Terai were diagnosed with arsenicosis. In Nawalparasi, one of the affected districts, around 60% of the population were diagnosed with the same condition (Rasaili et al., 2024). Skin disorders are among the most reported health issues following arsenic exposure.

Although awareness and capacity among healthcare professionals were minimal up to the year 2000 with limited knowledge and skills to diagnose or manage arsenic-associated health conditions (WHO & NHRC, 2009) recent reports indicate that many health workers are now equipped to treat various complications arising from arsenic exposure. Despite these advancements, no comprehensive research or large-scale surveys have been conducted in the Terai region since 2009 to evaluate the extent of arsenic contamination and the incidence of arsenicosis in Nepal.

5. RECOMMENDATIONS

To address the identified vulnerabilities and ensure long-term water safety, we propose the following measures: (1) routine monitoring of wells by establishing a credible regulatory body to track potential contamination trends, (2) implementing community-based water safety literacy initiatives for consumers, and (3) promotion of preventive strategies, including artificial ground water recharge and rainwater harvesting systems to diversify water sources.

6. CONCLUSION

This study confirms that arsenic levels in shallow public wells are below detection limits, indicating no immediate health risk from arsenic exposure. Despite this, deep aquifer contamination in the Kathmandu Valley and critically low public awareness sustains latent vulnerability. These findings underscore the need for stratified and proactive water safety, as detailed in the following recommendations.

ACKNOWLEDGEMENTS

We express our profound thanks to Dr. Anupama Karki of Bir Hospital and Associate Professor Dr. Eliza Aryal of Tribhuvan University Teaching Hospital for their valuable insights and support. We also acknowledge the contributions of the Environment and Public Health Organization (ENPHO), Kathmandu Upatyaka Khanepani Limited (KUKL), and the ward officials of Kathmandu Metropolitan City for their cooperation and assistance throughout the study.

REFERENCES

APHA, AWWA, & WEF. (2017). *Standard methods for the examination of water and wastewater* (23rd ed.). American Public Health Association.

Bajracharya, A. M., Yami, K. D., Prasai, T., Basnyat, S. R., & Lekhak, B. (2007). Assessment of drinking water quality of Kathmandu metropolitan areas. *Nepal Journal of Science and Technology, 8*, 113–118.

Banson, A. K., Amankwah, R. K., & Ndur, S. A. (2020). Conceptual model for arsenic distribution and its relationship with groundwater depth. *International Journal of Research and Scientific Innovation, 7*(10), 1–9.

Bhat, A., & Bhat, S. C. (2020). Arsenic pollution and remedial measures in West Bengal: An overview. *Global Journal for Research Analysis, 9*(10), 52–56.
DOI: 10.36106/gjra

Chapagain, S. K., Shrestha, S., Nakamura, T., Pandey, V. P., & Kazama, F. (2009). Arsenic occurrence in groundwater of Kathmandu Valley, Nepal. *Desalination and Water Treatment, 4*(1–3), 248–254.

Chaudhary, M. M., Hussain, S., Du, C., Conway, B. R., & Ghori, M. U. (2024). Arsenic in water: Understanding the chemistry, health implications, quantification and removal strategies. *ChemEngineering, 8*(4), 78.
DOI: 10.3390/chemengineering8040078

Department of Hydrology and Meteorology. (2023). *Annual climate report: Kathmandu Valley 2022*. Government of Nepal.

Emerman, S. H., Prasai, T., Anderson, R. B., & Palmer, M. A. (2010). Arsenic groundwater contamination in the Kathmandu Valley, Nepal, as a consequence of rapid erosion. *Journal of Nepal Geological Society, 40*, 49–60.

Gurung, J. K., Ishiga, H., Khadka, M. S., & Shrestha, N. R. (2006). Comparison of arsenic and nitrate contaminations in shallow and deep aquifers of Kathmandu Valley. *Journal of Nepal Geological Society, 33*, 55–62.

Gurung, J. K., Ishiga, H., Khadka, M. S., & Shrestha, N. R. (2007). Characterization of groundwater in the reference of arsenic and nitrate mobilization, Kathmandu Basin, Nepal.

Gwachha, S., Acharya, B., Dhakal, A., Shrestha, S. M., & Joshi, T. P. (2020). Assessment of arsenic content in deep groundwater of Kathmandu Valley, Nepal. *Nepal Journal of Science and Technology, 19*(1), 69–77.

Hassan, H. R. (2023). A review on different arsenic removal techniques used for decontamination of drinking water. *Science Progress, 106*(1), 2165964.
DOI: 10.1080/26395940.2023.2165964

ICIMOD. (2007). *Kathmandu Valley environment outlook*. International Centre for Integrated Mountain Development.

JICA. (1990). *Groundwater management project in the Kathmandu Valley: Final report*. Japan International Cooperation Agency.

JICA & ENPHO. (2005). *Arsenic vulnerability in groundwater resources in Kathmandu Valley: Final report*. Japan International Cooperation Agency & Environment and Public Health Organization.

Khatiwada, N. R., Takizawa, S., Tran, T. V. N., & Inoue, M. (2002). Groundwater contamination assessment for sustainable water supply in Kathmandu Valley, Nepal. *Water Science and Technology, 46*(9), 147–154.

Kathmandu Upatyaka Khanepani Limited (KUKL). (2024). *Seventeenth anniversary annual report 2081* [Annual report]. https://kathmanduwater.org/wp-content/uploads/2025/02/KUKL_Annual_Report_2081.pdf

Lamichhane, S., & Shakya, N. M. (2020). Shallow aquifer groundwater dynamics due to land use/cover change in highly urbanized basin: The case of Kathmandu Valley. *Journal of Hydrology: Regional Studies, 30*, 100707.
DOI: 10.1016/j.ejrh.2020.100707

Lamichhane, S., & Singh, A. K. (2019). Analysis of arsenic concentration in the constructed groundwater of Nepal: Case study of the Terai region of Nepal [Bachelor's thesis, Metropolia University of Applied Sciences].

Maharjan, M., Watanabe, C., Ahmad, S. A., & Ohtsuka, R. (2005). Arsenic contamination in drinking water and skin manifestations in lowland Nepal: The first community-based survey. *American Journal of Tropical Medicine and Hygiene, 73*(2), 477–479.

Maharjan, M., Shrestha, B. R., Shrestha, K. B., Shrestha, R. R., Raut, R., Shrestha, S. D., Kafle, B., & Ishihara, H. (2009). Arsenic contamination in groundwater resources in Kathmandu Valley. *Southeast Asian Water Environment, 3*, 73–79.

Mueller, B., Dangol, B., Ngai, T. K. K., & Hug, S. J. (2021). Kanchan arsenic filters in the lowlands of Nepal: Mode of operation, arsenic removal, and future improvements. *Environmental Geochemistry and Health, 43*(1), 375–389.
DOI: 10.1007/s10653-020-00718-9

NASC & ENPHO. (2004). *The state of arsenic in Nepal–2003*. National Arsenic Steering Committee & Environment and Public Health Organization.

NDWQS. (2022). *Implementation directives for national drinking water quality standards*. Government of Nepal, Ministry of Physical Planning and Works.

Nickson, R. T., McArthur, J. M., Ravenscroft, P., Burgess, W. G., & Ahmed, K. M. (2000). Mechanism of arsenic release to groundwater, Bangladesh and West Bengal. *Applied Geochemistry, 15*(4), 403–413.

Ogata, R., & Suenaga, K. (2023). Critical fluctuations in the arsenic concentration of tube well water in Nepal: Influences of monsoon and groundwater irrigation.
DOI: 10.2139/ssrn.4568649

Podgorski, J., & Berg, M. (2020). Global threat of arsenic in groundwater. *Science, 368*(6493), 845–850.
DOI: 10.1126/science.aba1510

Rasaili, P., Rai, S., Sachin, K. M., Saha, B., & Bhattarai, A. (2024). Arsenic contamination of groundwater sources and a comparative study of its remediation by various conventional and recent approaches in Nepal. *Vietnam Journal of Chemistry, 62*(3), 281–295.
DOI: 10.1002/vjch.202200116

Sarkar, B., Mitchell, E., Frisbie, S., Grigg, L., Adhikari, S., & Maskey Byanju, R. (2022). Drinking water quality and public health in the Kathmandu Valley, Nepal: Coliform bacteria, chemical contaminants, and health status of consumers. *Journal of Environmental and Public Health, 2022*.
DOI: 10.1155/2022/3895859

Shrestha, S., Bista, S., Byanjankar, N., Shrestha, S., Joshi, D. R., & Joshi, T. P. (2023). Groundwater quality evaluation for drinking purpose using water quality index in Kathmandu Valley, Nepal. *Water Science, 37*(3), 239–250.
DOI: 10.1080/23570008.2023.2237278

Shrestha, S., T. Nakamura, J. Magome, Y. Aihara, N. Kondo, E. Haramoto, B. Malla, J. Shindo, and K. Nishida. 2018. Groundwater use and diarrhea in urban Nepal: novel application of a geostatistical interpolation technique linking environmental and epidemiologic survey data. International Health 10(5):324–332.

Shrestha, S.M., K. Rijal, and M.R. Pokhrel. 2013. Arsenic contamination in the deep and shallow groundwater of Kathmandu Valley. Nepal Scientific World 11(11):25–31.

Stolze, L., Battistel, M., & Rolle, M. (2022). Oxidative dissolution of arsenic-bearing sulfide minerals in groundwater. *Environmental Science & Technology, 56*(8), 5049–5061. DOI: 10.1021/acs.est.2c00309

Valskys, V., Hassan, H. R., Wołkowicz, S., Satkūnas, J., Kibirkštis, G., & Ignatavičius, G. (2022). A review on detection techniques, health hazards and human health risk assessment of arsenic pollution in soil and groundwater. *Minerals, 12*(10), 1326. DOI: 10.3390/min12101326

Warner, N. R., Levy, J., Harpp, K., & Farruggia, F. (2008). Drinking water quality in Nepal's Kathmandu Valley: A survey and assessment of selected controlling site characteristics. *Hydrogeology Journal, 16*, 321–334.

WHO. (2008). *Guidelines for drinking-water quality* (3rd ed.). World Health Organization.

WHO & NHRC. (2009). *Detection, management and surveillance of arsenicosis in Nepal: Proceedings of the consultative workshop*. World Health Organization & Nepal Health Research Council.

Identification and Characterization of *Aeromonas* sp. KBK3 as a Multifunctional Plant Growth-Promoting Rhizobacterium from Banana

Govinda Pathak[1], Sandip Ghimire[1], Gyanu Raj Pandey[2], Junxi Shi[3], Manish Rijal[1], Durga Karki[1], Janardan Lamichhane[1]

[1] Department of Biotechnology, Kathmandu University, Kavre, Nepal
[2] Shubham Biotech Nepal Private Limited, Bharatpur, Chitwan, Nepal
[3] Food Safety Detection Key Laboratory of Sichuan Province, Chengdu, China

***CORRESPONDING AUTHOR:**
Janardan Lamichhane
Email: ljanardan@ku.edu.np

**ISSN : 2382-5359(Online),
1994-1412(Print)**

DOI:
https://doi.org/10.3126/njst.v22i2.100110

Date of Submission: 24 Sep, 2025

Date of Acceptance: 26 May, 2026

ABSTRACT

In sustainable agriculture, plant growth-promoting rhizobacteria (PGPR) are beneficial bacteria, that enhance nutrient availability and improve plant resilience to stress. This study was conducted to isolate and characterize PGPR from the banana (*Musa* sp.) rhizosphere. An efficient strain, identified as *Aeromonas* sp. KBK3 via biochemical tests and 16S rRNA gene sequencing, demonstrated significant plant growth-promoting traits. It showed noteworthy potassium solubilization index of 3.77 ± 0.27 and produced 11.4 ± 0.28 ppm of indole-3-acetic acid (IAA). The strain showed optimal growth at 35°C, pH 7, 0.5% NaCl, and tolerated 30% osmotic stress. Its PGPR traits include potassium and phosphorus solubilization, IAA production, extracellular enzymes such as cellulase and pectinase production, and tolerance to 30% polyethylene glycol (PEG). In addition, the strain didn't show any phytotoxic effects towards spinach seed germination. Therefore, *Aeromonas* sp. KBK3 is a promising biofertilizer to increase nutrient availability and crop productivity. However, it must be validated through greenhouse and field trials for its agronomic performance.

Keywords: Plant growth promoting rhizobacteria (PGPR), Potassium solubilization, Indole-3-acetic acid (IAA), Phosphate solubilization, germination, biofertilizer

1. INTRODUCTION

Global food security is increasingly threatened by a confluence of factors: steady population growth, the shrinkage of cultivable land, and the escalating challenges of climate change (Daniel *et al.* 2022; Alzate Zuluaga *et al.* 2024). To meet rising demands, agricultural systems have become dependent on synthetic inputs, yet their use poses serious adverse effects on both environmental integrity and human health (Saeed *et al.*

2021). This unsustainable paradigm underscores the critical necessity of developing alternative production systems that are both sustainable and eco-friendly. A promising approach involves harnessing beneficial microorganisms, particularly plant growth-promoting rhizobacteria (PGPR), to enhance crop productivity (Saeed *et al.* 2021; Yang *et al*. 2024).

Characterized by complex plant-soil-microbe interactions, the rhizosphere constitutes a critical hotspot for microbial processes (Basu *et al.* 2021; Chandran *et al.* 2021; Solomon *et al.* 2024; Wang *et al.* 2024). Through the release of complex mixtures of photosynthates, known as rhizodeposits, plants exude chemical signals that selectively recruit and shape the surrounding microbial community (De Andrade *et al.* 2023; Solomon *et al.* 2024). This dynamic interplay directly impacts plant physiology and health. Among the key beneficiaries and mediators of this relationship are PGPR, a heterogeneous group of bacteria that efficiently colonize the rhizoplane and contribute to plant fitness (Basu *et al.* 2021; Yang *et al.* 2024).

The banana (*Musa* sp.) rhizosphere represents a prime niche for prospecting novel PGPR, a promise derived from its nutrient-rich root exudates and stable physicochemical conditions. These attributes support microbial communities that perform essential functions, directly enhancing plant growth, nutrient acquisition, and overall productivity (Yang *et al.* 2021; Muzami *et al.* 2025). Dominant among these communities are beneficial phyla such as Proteobacteria, Actinobacteria and Cyanobacteria (Muzami *et al.* 2025). PGPR strains isolated from this environment often possess multiple plant-beneficial traits, including the production of phytohormones like indole-3-acetic acid (IAA), the solubilization of essential nutrients (e.g., phosphate, potassium, zinc), nitrogen fixation, chlorophyll biosynthesis and biocontrol activity against pathogens (KC *et al.* 2020). Consistent with this functional diversity, several bacterial genera are recurrently identified as effective PGPR in banana systems, including *Bacillus, Pseudomonas, Enterobacter, Kosakonia, Paenibacillus,* and *Streptomyces.* Specific species, such as *Bacillus subtilis, Pseudomonas putida,* and *Streptomyces aureoverticillatus*, have been highlighted for their exceptional PGPR activity and efficacy as biocontrol agents (Posada *et al.* 2016; Yang *et al.* 2021; Tatung and Deb 2023).

This study aims to isolate and characterize native PGPR from the banana rhizosphere to identify highly efficient, ecologically adapted strains. The goal is to develop these strains into microbial inoculants that enhance crop vigor, improve root architecture, strengthen nutrient acquisition, and promote disease suppression. Ultimately, this approach seeks to foster a resilient root microbiome, thereby contributing to agroecosystem resilience and food security.

2. MATERIALS AND METHODS

2.1 Materials and Equipment

All chemicals, growth media, and reagents were of microbiological or molecular biology grade. General chemicals and growth media were procured from HiMedia and Fisher Scientific, while molecular biology reagents, buffers, and enzymes were obtained from Thermo Scientific, Cleaver Scientific, SRL, and New England Biolabs. Specific kits, including the Genomic DNA extraction kit (Genes2me, India) and Hi-Carbo kit (HiMedia), were used as per the manufacturers' instructions. PCR primers were synthesized by Barcode Biosciences.

Laboratory consumables included glassware from Borosil and plasticware from Tarson. The following equipment was used: a Labomed Lx 400 microscope for microscopic characterization; a Lab Companion IB-01-65L incubator for culture growth; a Nuve FN120 oven for drying; and a Shimadzu UV-1800 spectrophotometer for absorbance measurements. Centrifugation was performed using MPW-260R centrifuge for DNA extraction and a Hermle Z-336 model for other processes. PCR amplification was carried out in a Bio-Rad T100TM Thermal Cycler, and DNA fragments were visualized using a GenoSens 2100 gel documentation system.

2.2 Sample collection, Isolation and Confirmation of Potassium Solubilizing Bacteria (KSB)

Rhizospheric soil samples were collected from a banana field in Khatrithowk, Sindhupalchowk, Nepal (Elevation: 1028 m; Coordinates: 27°41′54″ N and 085°43′53″ E; see Fig. 1) using a Garmin eTrex 10 handheld GPS receiver. For microbial isolation, 10 g of soil was weighed using a BEL Engineering M124A balance and serially diluted in 90 mL of sterile distilled water. Aliquots (1 mL) from appropriate dilution were plated via the pour plate method onto sterilized Aleksandrow agar. The plates were incubated at 30 ºC for 24 hours. Distinct colonies were purified by repeated streaking on nutrient agar. The pure isolated colony was spot inoculated into an Aleksandrow agar plate and incubated at 28 °C for 4 days. The potassium solubilization index (KSI) was calculated using the formula(Sun *et al.* 2020; Yaghoubi Khanghahi *et al.* 2021):

$$KSI = \frac{\text{diameter of solubilization halo} + \text{colony diameter}}{\text{Colony diameter}}$$

Pure cultures were maintained on Nutrient agar slants for short-term storage and preserved long-term at -80 °C in cryovials containing the respective basal medium supplemented with 20% glycerol (Cappuccino and Welsh 2019).

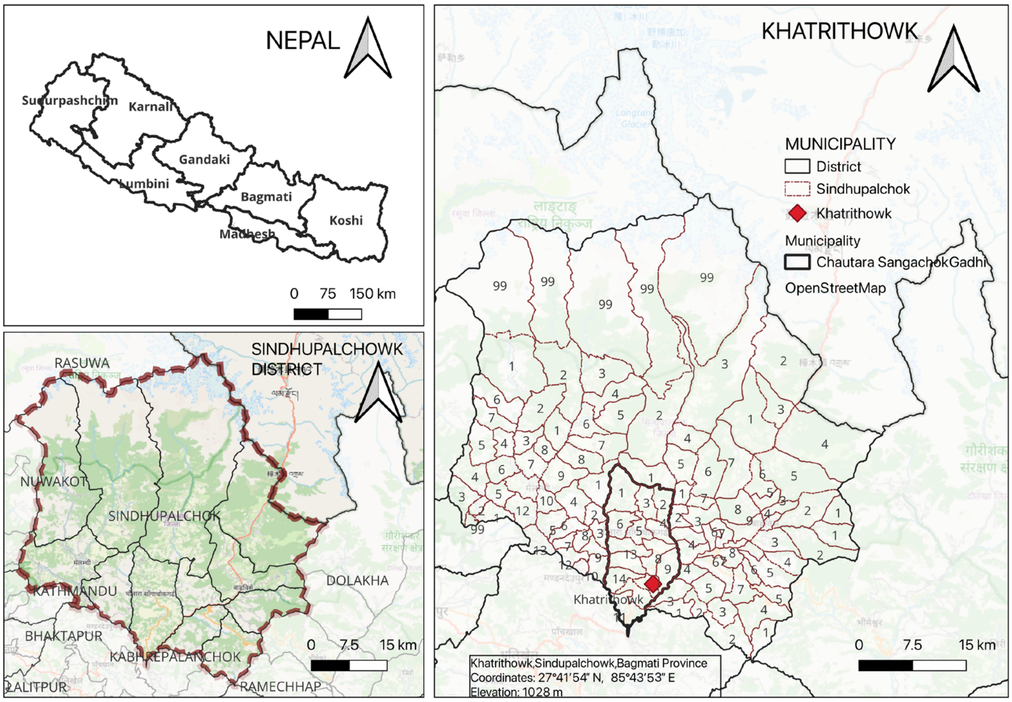

***Fig 1:** Administrative map of Khatrithowk (Ward No. 10, Chautara Sangachokgadhi Municipality) showing ward boundaries and the sampled site (red diamond).*

2.3 Identification of Selected Bacterial Strain

2.3.1 Molecular Identification

Genomic DNA (gDNA) was purified from the isolated organism by bacterial DNA extraction kit. About 2 ml of the isolate, cultured in 5 ml nutrient broth at 30 ºC for 24 hours, was centrifuged at 15000g for a minute. The pellet was processed as per manufacturer's protocol.

The 16S rRNA gene was amplified using universal primers 27F (5'-AGAGTTTGATCMTGGCTCAG-3') /1492R (5'-TACGGYTACCTTGTTACGACTT -3') primers (22) and sequenced by 785F (5'-GGATTAGATACCCTGGTA-3') /907R (5'-CCGTCAATTCMTTTRAGTTT- 3') at Macrogen Inc., South Korea.

Raw sequences were trimmed and assembled using Codon Code Aligner v 12.0.1 (CodonCode) and the consensus sequence was subjected to BLASTN and the database—rRNA/ITS database was selected in NCBI. Sixteen highly similar sequences (based on BLAST result) along with our sequence were taken in FASTA format for phylogenetic analysis. A maximum likelihood phylogenetic tree was constructed in MEGA12 (Tamura et al. 2021) via the Tamura-Nei model (Tamura and Masatoshi Nei 1993), with nodal support assessed via 2,000 bootstrap replicates (Felsenstein 1985).

2.3.2 Morphological and Biochemical

Characterization

The isolated strain was cultured on nutrient agar and incubated at 30 °C for 24 hours to study its colony morphology, documenting characteristics including shape, size, pigmentation, elevation, margin, opacity, surface texture, and any change in medium color. Micromorphological analysis was performed via Gram staining using a HiMedia Kit following established methods (Cheesbrough 2006), with subsequent observation under a light microscope at 1000X magnification. Biochemical characterization included standard tests for methyl red, Voges-Proskauer, oxidase, catalase, and citrate utilization (Cappuccino and Welsh 2019). Carbohydrate utilization profiles were determined using a HiCarbo kit according to the manufacturer's instructions, and all morphological and biochemical data were interpreted with reference to Bergey's Manual of Systematic Bacteriology (Martin-Carnahan and Joseph 2015).

2.4 Growth under Different Abiotic Stress Conditions

2.4.1 Temperature

The optimal growth temperature was determined by inoculating 10 mL of nutrient broth with a loopful of an overnight culture and incubating at 25, 30, 35 and 40ºC. After 24 hours of incubation, bacterial growth was quantified by measuring optical density at 600 nm using UV-Vis spectrophotometer (Agunbiade *et al.* 2024).

2.4.2 Salt Concentrations

Salt tolerance was assessed in nutrient broth supplemented with varying concentrations of NaCl (0.5%, 5.5%, and 10.5% w/v). The medium was inoculated with a loopful of an overnight bacterial culture and incubated at 30ºC for 24 hours. Growth under these saline conditions was measured as OD_{600} (Agunbiade *et al.* 2024).

2.4.3 pH

To evaluate growth at different pH levels, the bacterium was inoculated into 10 mL of nutrient broth adjusted to acidic (pH 4), neutral (pH 7), and alkaline (pH 10) conditions using appropriate buffers. The cultures were incubated at 30ºC for 24 hours, and growth was determined spectrophotometrically at 600 nm (Agunbiade *et al.* 2024).

2.4.4 Drought

Drought stress was simulated using polyethylene glycol (PEG 400, SRL-25322-68-3). A loopful of bacterial culture was used to inoculate nutrient broth supplemented with 0%, 15%, and 30% (v/v) PEG. The cultures were incubated at 30°C for 24 hours, and bacterial growth was assessed by measuring the OD_{600} (Sandhya *et al.* 2009; Agunbiade *et al.* 2024; Noureen *et al*. 2024; Rafedzi *et al*. 2024).

2.5 Plant Growth Promoting Traits

2.5.1 Indole-Acetic Acid (IAA) Production

IAA production was quantified following the method of Loper and Schroth. A pure bacterial isolate was inoculated into DEV tryptophan broth and incubated at 30 ºC for 72 hours. The bacterial suspension was then centrifuged at 5000 g for 20 minutes at 4 ºC. Subsequently, 2mL of the cell-free supernatant was mixed with 4 mL of Salkowski's reagent and a few drops of orthophosphoric acid (H_3PO_4). The development of pink color indicated IAA production. The IAA concentration was determined by measuring the absorbance at 530 nm and comparing it to a standard IAA calibration curve (AlAli *et al.* 2021; Agunbiade *et al.* 2024).

2.5.2 HCN Production test

The potential for HCN production was assessed using nutrient agar supplemented with glycine (4.4 g/L). Bacterial cultures were streaked onto the agar, and a filter paper soaked in a picrate solution (0.5% picric acid and 1% Na_2CO_3) was attached to the underside of the plate lid. The plates were sealed with parafilm to prevent desiccation and incubated at 30°C for 48 hours. A color change of the filter paper from yellow to reddish-brown was considered a positive result (Agunbiade *et al.* 2024).

2.5.3 Phosphate solubilization

The ability to solubilize inorganic phosphate was tested on Pikovskaya agar medium. The agar plates were spot-inoculated with an overnight bacterial culture and incubated at 30°C for 4 days. The formation of a clear halo zone around the bacterial colony was indicative of phosphate solubilization (Wan *et al.* 2020).

2.6 Hydrolytic Enzyme Production

2.6.1 Protease

Protease production was assessed using skimmed milk agar. Plates were inoculated in a zigzag pattern with the bacterial culture and incubated at 30°C for 24 hours. The formation of a clear halo zone around the bacterial growth, indicating casein hydrolysis, was recorded as a positive result (Lakshmi 2014; Marathe *et al*. 2018).

2.6.2 Amylase

Amylase activity was detected on nutrient agar supplemented with 1% (w/v) starch. After the bacterial strain was streaked in zigzag pattern onto the medium and incubated at 30°C for 24 hours, the plates were flooded with an iodine solution. A clear zone surrounding the bacterial growth against a dark blue background confirmed starch hydrolysis and a positive result (AlAli *et al.* 2021).

2.6.3 Cellulase

Cellulase production was evaluated on nutrient agar containing 1% (w/v) carboxymethyl cellulose (CMC). The medium was streaked with bacterial strain and incubated at 30°C for 24 hours. The plates were then flooded with a 0.1% Congo red and washed with 1M NaCl. The formation of a clean zone around the colony was recorded as a positive result (Gautam *et al.* 2012).

2.6.4 Pectinase

Nutrient agar incorporated with 1% pectin was used for the isolation and screening of pectinolytic bacteria. The initial pH of medium was adjusted to 4.5. This medium was sterilized and distributed aseptically in Petri dishes. Isolates were streaked into this media and incubated at 30°C for 24 hours. For primary screening, plates were stained with 50 mM iodine for result. A clear halo zone around the colonies indicates the pectinolytic activity of bacteria (Khairnar *et al*. 2009; Raju and Divakar 2013).

2.6.5 Chitinase

For screening of chitinase producing bacteria, the nutrient agar medium amended with 1% (w/v) colloidal chitin was used. The colonies showing clearance zones, after 24 hours upon incubating at 30°C, on a creamish background were considered as chitinase-producing bacteria (Saima *et al.* 2013).

2.7 Seed Germination Test

A seed vigour assay was conducted under laboratory conditions to evaluate the plant growth-promoting potential of selected bacterial isolates on broad leaf mustard (*Brassica juncea* var. Khumal Chaudapat). Indigenous seeds were procured from the Nepal Agricultural Research Council (NARC), Khumaltar.

Seeds were surface-sterilized by immersion in 70% (v/v) ethanol for one minute, followed by rinsing with sterile distilled water. Subsequently, seeds were treated with a 5% (v/v) sodium hypochlorite solution for 4-5 minutes and thoroughly rinsed 4-6 times with sterile distilled water. A bacterial suspension was prepared by harvesting a 24-hour-old nutrient broth culture via centrifugation and resuspending the cells in 0.85% saline to an optical density (OD_{600}) of 1. The surface-sterilized seeds were then immersed in this bacterial suspension for two hours. Following inoculation, the seeds were blotted dry on sterile filter paper (Sartorious, 393) for 12 hours. For the germination test, one hundred treated seeds were placed aseptically in 90 mm petri plates, with three replicates per treatment. The plates were maintained in an incubator at 25°C, regularly watered, and monitored daily for germination over eight days. A control treatment consisted of surface-sterilized seeds treated with 0.85% saline solution without bacteria. The number of germinated seeds was counted every day after incubation, and each spinach seed was adjudged as germinated if the radicle has emerged. Post priming radicle and plumule (early seedling) lengths were measured following standard assessment methods used for spinach, with measurements taken on day 8 after sowing on petri plate (Chen and Arora 2011; Wang *et al.* 2019).

2.8 Statistical Analysis

Statistical analyses were carried out in OriginPro 2024. A one-way analysis of variance (ANOVA) was used to determine the significance of differences among treatment groups for quantitative data. Where ANOVA indicated a significant effect ($p < 0.05$), Tukey's post-hoc test was applied for multiple comparisons. Specifically, for the seed germination assay, a two-tailed, paired-sample t-test was employed to compare the means of the treatment and control groups, with the null hypothesis of no difference between means. All experiments in this study were conducted in triplicate ($n = 3$), and the mean values with standard error were calculated accordingly.

3. RESULT

3.1 Potassium Solubilization Index

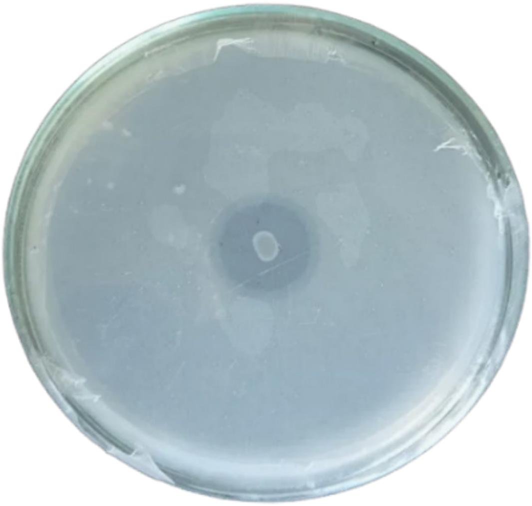

Fig 2: *Potassium solubilization index (KSI) (3.77± 0.27) of the KBK3. Clear halo zones around colonies on potassium-bearing medium indicate solubilization*

Initial screening of bacterial isolate from the banana rhizosphere on Alexandrow agar led to the identification of a promising potassium-solubilizing bacterium (KSB), strain KBK3. The isolate demonstrated a high potassium solubilization index (KSI) of 3.77 ± 0.27 after a 4-day incubation period (Fig. 2).

3.2 Identification of Selected Bacterial Strain

3.2.1 Molecular Characterization of the isolate

A maximum-likelihood phylogenetic tree (Fig. 3), based on 16S rRNA gene sequences, was constructed to determine the taxonomic position of the environmental isolate KBK3 within the genus *Aeromonas*. The tree revealed that KBK3 forms a distinct branch within a well-supported clade containing *Aeromonas dhakensis* strain BLW14 and *Aeromonas* media strain BCPP1. Despite this close association, measurable genetic distances (0.01 – 0.02) separate KBK3 from its nearest neighbor, *A. dhakensis* BLW14, indicating a degree of sequence divergence. This isolate consistently clustered within the broader *Aeromonas* lineage, with high bootstrap support at major nodes, confirming its unambiguous placement within this genus while highlighting its phylogenetic distinctiveness from other closely related species and strains included in the analysis.

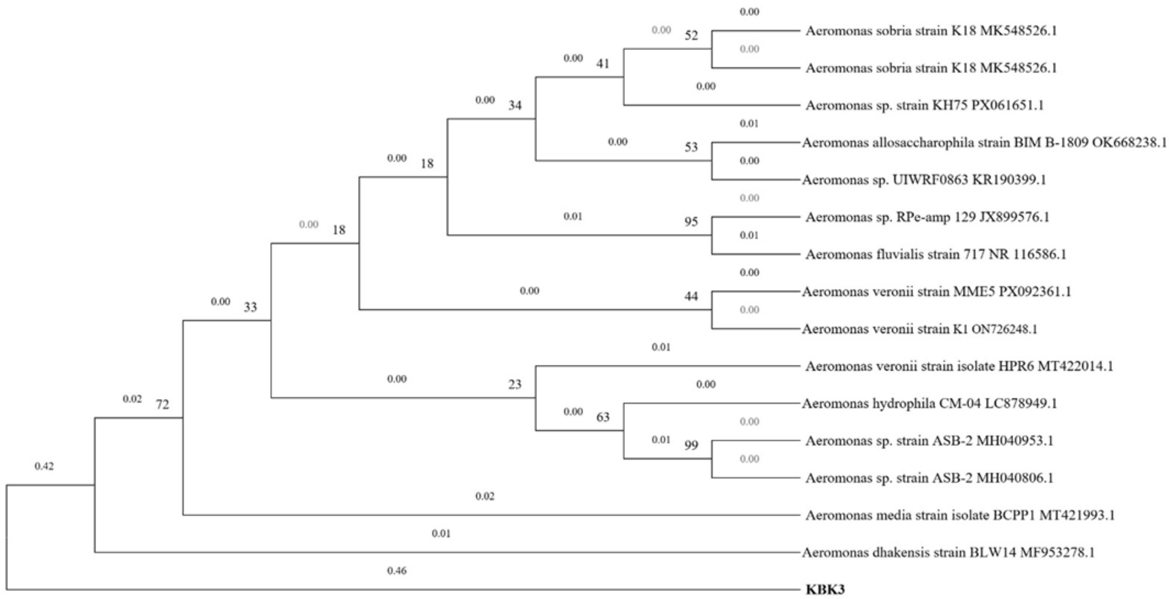

Fig 3: *Maximum likelihood phylogenetic tree of the isolate based on 16S rRNA sequence data (Tamura-Nei model). The tree is drawn with branch lengths (shown next to the branches) computed using the maximum likelihood method and measured in the number of substitutions per site. Bootstrap values (2000 replicates) were shown at nodes; branches with <50% support were collapsed.*

3.2.2 Phenotypic descriptions of the isolate

The isolate KBK3 exhibited phenotypic characteristics consistent with members of the genus *Aeromonas*. Colonies on nutrient agar medium were circular, convex, entire-margined, creamy-white, opaque, and displayed a smooth, sticky texture. Biochemically, KBK3 was positive for oxidase, catalase, and citrate utilization, and was motile. It produced acid and gas from glucose, sucrose, and lactose on triple sugar iron agar, but did not produce H_2S. The isolate demonstrated as extensive carbohydrate fermentation profile (Table 1), utilizing a wide range of sugars including lactose, xylose, maltose, fructose, dextrose, galactose, raffinose, trehalose, melibiose, sucrose, mannose, inulin, sodium gluconate, glycerol, salicin, dulcitol, inositol, sorbitol, mannitol, adonitol, arabitol, erythritol, α-methyl-D-glucoside, rhamnose, cellobiose, melezitose, α-methyl-D-mannoside, xylitol, ONPG (O-nitrophenyl-β-D-galactopyranoside), esculin, D-arabinose, citrate, malonate, and sorbose, but was negative for L-arabinose fermentation. On blood agar, KBK3 displayed γ-hemolysis.

Table 1: Phenotypic characterization of bacterial isolate comparison with closely related species based on BLAST result

Test	KBK3	A. *hydrophila* (Abbott *et al.* 2003; Abulhamd 2009; Ahangarzadeh *et al.* 2022)
Colony morphology		
Size(mm)	1.67	
Gram staining	-	-
Elevation	Convex	
Margin	Entire	
Colony form	Circular	
Pigmentation	Creamy white	
Opacity	Opaque	

Surface appearance	Smooth	
Texture	Sticky	
Oxidase	+	+
Catalase	+	+
H_2S	-	-
Motile	+	+
Methyl-red	-	+
Voges-Proskauer	-	+/-
Blood agar	γ Hemolysis	β hemolytic
Sugar Utilization		
Lactose	+	-/+
Xylose	+	-
Maltose	+	+
Fructose	+	
Dextrose	+	+
Galactose	+	
Raffinose	+	-
Trehalose	+	+
Melibiose	+	-
Sucrose	+	+
L-Arabinose	-	+
Mannose	+	+
Inulin	+	-
Sodium gluconate	+	+/-
Glycerol	+	+
Salicin	+	+/-
Dulcitol	+	-
Inositol	+	-
Sorbitol	+	-
Mannitol	+	+
Adonitol	+	-
Arabitol	+	-
Erythritol	+	-
α-Methyl-D-glucoside	+	+/-
Rhamnose	+	-/+
Cellobiose	+	-
Melezitose	+	
α-Methyl-D-Mannoside	+	
Xylitol	+	-
ONPG	+	+

Esculin	+	+
D-Arabinose	+	+
Citrate	+	+
Malonate	+	-
Sorbose	+	

3.3 Growth under different abiotic stress

3.3.1 Temperature

The isolate exhibited optimal growth at 35°C, achieving an OD_{600} of 0.645 ± 0.007 after 24 hours. Growth was significantly reduced at 30°C (0.57 ± 0.00153), 25°C (0.352 ± 0.00379), and 40°C (0.049 ± 0.00493), as determined by one-way ANOVA and Tukey's test ($p < 0.05$) (Fig. 4a).

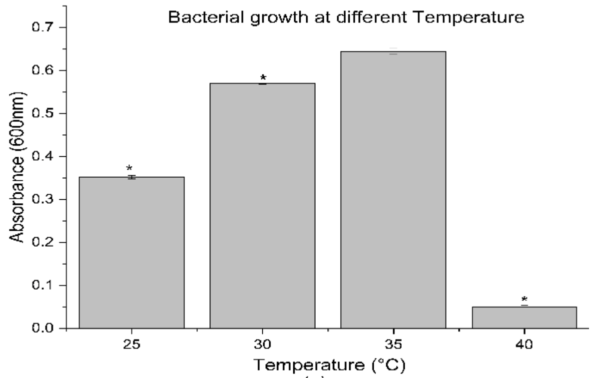

(a)

3.3.2 Salt

Bacterial growth under saline conditions was evaluated at concentrations of 0.5%, 5.5%, and 10.5% NaCl by measuring optical density at 600 nm after 24 hours. The isolate showed optimal growth at 0.5% NaCl (0.49733 ± 0.0229). Statistical analysis (Tukey's test, $p < 0.05$) revealed that growth at this concentration was significantly higher than at 5.5% (0.19167 ± 0.00416) and 10.5% (0.07067 ± 0.00404) NaCl (Fig. 4b).

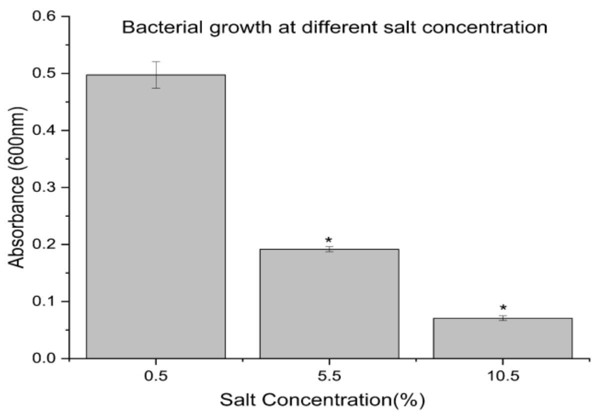

(b)

3.3.3 pH

The effect of pH on bacterial growth was assessed at pH 4, 7, and 9 by measuring optical density at 600 nm after 24 hours. Optimal growth occurred at pH 7 (0.46933 ± 0.00233). Statistical analysis revealed this growth was significantly higher than at pH 4 (0.18333 ± 0.00203) and pH 9 (0.095 ± 0.00252), according to Tukey's post-hoc test ($p < 0.05$) (Fig. 4c).

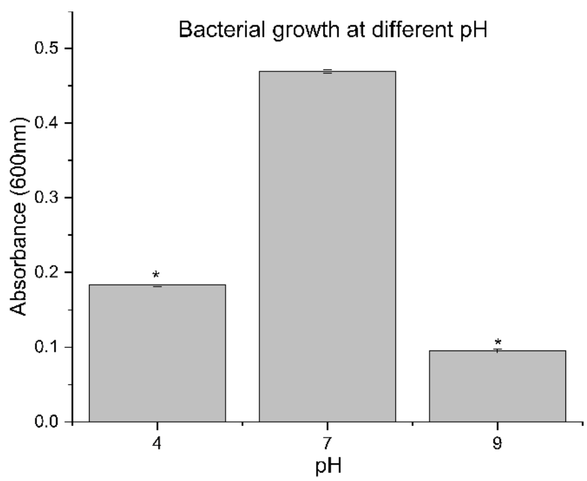

(c)

3.3.4 Drought

To assess drought tolerance, bacterial growth was measured in media supplemented with 0%, 15%, and 30% PEG. After 24 hours, optical density at 600 nm revealed a significant, concentration-dependent inhibition. While significantly higher ($p < 0.05$) growth occurred in the absence of PEG (0.553 ± 0.00265), it was markedly reduced at 15% PEG (0.21933 ± 0.00521) and 30% PEG (0.10833 ± 0.00328) (Fig. 4d).

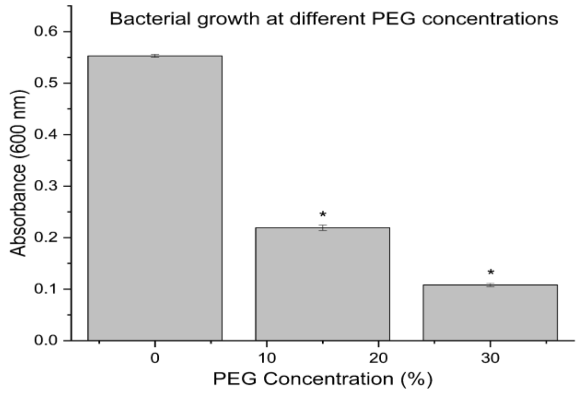

(d)

*Fig 4: Growth of KBK3 in nutrient broth under (a) varying temperature; (b) varying concentration of salt (%); (c) varying PH and (d) varying concentration of PEG (%). * Significantly higher than the compared groups (α = 0.05).*

3.4 Plant Growth Promoting Traits

3.4.1 Indole Acetic acid (IAA) production

This study quantified indole-3-acetic acid (IAA) production by the bacterial isolate. A standard calibration curve ($y= 0.01682x + 0.04027$; Pearson's $r = 0.99551$) (Fig. 5) was used to determine concentrations. Following 72 hours of incubation in DEV tryptophan broth, isolate KBK3 demonstrated the ability to synthesize IAA, producing 11.4 ± 0.28 ppm.

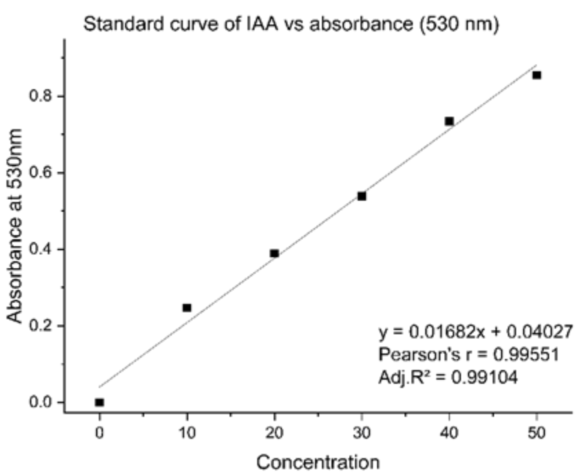

Fig 5: Standard curve of IAA concentration vs absorbance at 530 nm

3.4.2 Determination of other plant growth promoting traits

Assessment of key plant growth-promoting traits revealed that strain KBK3 solubilized phosphate (Table 2). However, it did not exhibit nitrogen-fixing activity or produce hydrogen cyanide (HCN).

Table 2: Plant growth promoting traits exhibited by KBK3

Plant growth traits	KBK3
Nitrogen fixation	-
Phosphate solubilization	+
HCN produced	-

3.5 Hydrolytic enzymes production

KBK3 demonstrated a selective enzymatic profile, positive for cellulase and pectinase production but negative for chitinase, protease, and amylase (Table 3).

Table 3: Hydrolytic enzymes produced by KBK3

Enzymes produced	KBK3
Cellulase	+
Chitinase	-
Proteinase	-
Amylase	-
Pectinase	+

3.6 Seed Germination

Seed germination and early seedling growth parameters were analyzed using a paired two-sample t-test. While PGPR-treated seeds showed no significant difference in germination rate compared to the control (28 ± 1.15 vs. 29.33 ± 0.88 seeds, $p = 0.27$) and exhibited no phytotoxic effects, treated seedlings demonstrated non-significant increase in total length (5.64 ± 0.25 cm vs. 5.12 ± 0.24 cm), radicle length (3.21 ± 0.22 cm vs. 2.77 ± 0.20 cm), and plumule length (2.43 ± 0.12 cm vs. 2.34 ± 0.10 cm). These results indicate that, although statistically non-significant under the tested conditions, the PGPR inoculation was safe and showed a positive trend toward enhancing early seedling vigor.

4. DISCUSSION

The banana rhizosphere isolate KBK3 demonstrated rapid potassium solubilization, achieving a high solubilization index (KSI) of 3.77 ± 0.27 within four days. This efficiency is significant when compared to the broader spectrum of potassium-solubilizing microorganisms (KSMs), which include genera such as *Bacillus, Paenibacillus, Pseudomonas, Burkholderia, Enterobacter, Aspergillus, Penicillium,* and several *actinomycetes* that mobilize insoluble soil potassium through organic acid secretion such as tartaric acid, citric acid, and oxalic acid (Olaniyan *et al.* 2022; Sharma *et al*. 2024).

Our isolate's performance places it among the more efficient and faster-acting potassium-solubilizing bacteria (KSB) reported. It exceeds the KSI of several moderate-efficiency KSB, such as *Metabacillus indicus* (KSI ~ 3 after 7 days) (Fatema *et al*. 2024), halotolerant species like *Halomonas and Oceanobacillus* (KSI 2.33-2.96 after 5 days) (Reang *et al.* 2022), and other *Aeromonas* strains (KSI 2.25-2.98 after 5 days) (Antonelli *et al.* 2025). It also compares favorably to *Serratia* sp. Bg22c (KSI 2.50 after 2 days) (Bouizgarne *et al.* 2023) and high-performing actinomycetes that require longer incubation, such as *Streptomyces anulatus* (KSI 3.17 after 11 days) (Boubekri *et al.* 2021). While some isolates from specific niches report higher indices (e.g., KSI up to 6.70 after 7 days) (Saheewala *et al.* 2023), they generally require nearly twice the incubation time. Similarly, other studies report indices in the range of 1.57-5.67 after 7 days (Nawaz et al. 2023), 1.79 after 7 days at low temperature (Yan *et al.* 2024), and more than 2 after 8 days (Raji and Thangavelu 2021). Thus, the combination of a high KSI and a short incubation period underscores the notable solubilization capacity of KBK3. This trait, central to its biofertilizer potential, can enhance plant-available potassium and reduce dependency on chemical inputs, offering a promising sustainable alternative for nutrient management in agriculture.

Based on the integrated phylogenetic and phenotypic features such as gram negative, motile, oxidase & catalase positive, H_2S negative, utilization of maltose, dextrose, trehalose, mannitol, ONPG and esculin, isolate KBK3 can be confidently assigned to the genus *Aeromonas*. The phylogenetic reconstruction placed KBK3 within a well-supported clade of *Aeromonas* species, most closely related to *Aeromonas dhakensis*, yet the observed genetic distances and notable biochemical variations, such as its broad sugar fermentation profile in raffinose, melibiose, L-arabinose, inulin, dulcitol, inositol, sorbitol, adonitol, arabitol, erythritol, cellobiose, xylitol, & malonate, and non-hemolytic activity, suggest that KBK3 may represent a distinct strain within the genus (Abbott *et al.* 2003; Martin-Carnahan & Joseph 2015; Abo-Shama *et al.* 2025). These discrepancies, coupled with the high metabolic versatility observed in biochemical assays, support a conservative classification as *Aeromonas* sp. KBK3, reflecting its clear genus-level affiliation while acknowledging sufficient divergence to preclude reliable species-level identification without further genomic characterization.

The indole-3-acetic acid (IAA) production of *Aeromonas* sp. KBK3 was quantified at 11.4 ± 0.28 ppm (µg/mL) after 72 hours of incubation. This output situates the strain within as intermediate range of phytohormone synthesis, a level often associated with the beneficial modulation of root architecture by plant growth-promoting rhizobacteria (PGPR). When compared to other PGPR, KBK3's production exceeds that of weaker producers, such as *Bacillus zanthoxyli* strain GGS1 (1.5 ppm after 9 hours) (Kim *et al.* 2024) and *Stenotrophomonas* sp. strain C1 and C10 (8.94 ppm and 2.68 ppm after 5 days, respectively) (Abd-Alla *et al.* 2024). Conversely, it is substantially lower than that of highly efficient producers like *Klebsiella* sp. CK-40 and *Bacillus cereus* M28, which can yield over 41.06 ppm and 378.44 ppm, respectively (Ganesh *et al*. 2024; Uzma *et al.* 2025). Critically, both deficient and excessive IAA levels can impair plant development by disrupting auxin homeostasis. Low IAA concentrations can reduce primary root elongation and suppress lateral root formation, thereby limiting nutrient uptake (Fu *et al.* 2015; Liu *et al.* 2023; Yang *et al.* 2025). Excessively high IAA, however, may inhibit primary root growth, disrupt cellular elongation, and induce hormonal stress responses (Roychoudhry and Kepinski 2021; Ashokkumar *et al.* 2025). Therefore, maintaining a moderate auxin concentration is essential for balanced root development and overall plant performance (Pantoja-Guerra *et al*. 2023). In this context, the moderate but consistent IAA production by KBK3 represents a functionally meaningful trait. It is sufficient to stimulate positive morphological changes without triggering inhibitory stress responses, underscoring the strain's suitability for development as a balanced and effective bioinoculant for sustainable agriculture.

The physiological profile of KBK3 indicates a broad adaptive capacity. Notably, KBK3's ability to grow at 10.5% NaCl surpasses the tolerance of other environmental *Aeromonas* strains, such as *Aeromonas* sp. FONT1B and FONT3B, which fail to grow at 5% NaCl, though *Aeromonas* sp. FONT6 can tolerate up to 10% (Antonelli *et al.* 2025). Its growth across a wide pH range (4-9) is consistent with other resilient strains like FONT6 and strains A1-2 and C7_8, which also grow at pH 4 and 10 (Agunbiade *et al*. 2024; Antonelli *et al.* 2025). The pathogenic *Aeromonas veronii* shows a similar pH range (5-9) but markedly weaker halotolerance, with poor growth above 3% NaCl (Hassan *et al.* 2017). While some *Aeromonas* strains exhibit survival at extremely low temperature (-72°C) (Abeyta *et al.* 1986), KBK3's optimal growth at 35°C aligns with other PGPR *Aeromonas* strains (Agunbiade *et al.* 2024). Importantly, its sustained growth under high osmotic stress (30% PEG) mirrors the notable drought tolerance reported for strains A1-2 and C7_8 (Agunbiade *et al.* 2024). Collectively, these results position *Aeromonas* sp. KBK3 as a robust PGPR candidate with notable abiotic stress resilience, enhancing its potential for application as a bioinoculant in suboptimal or variable soil conditions.

The isolate *Aeromonas* sp. KBK3 further demonstrated a capacity to enhance plant nutrition through phosphate solubilization. Phosphorus (P) is a critical macronutrient for fundamental processes such as photosynthesis and cell division; however, its bioavailability in soil is severely limited, with only 0.1-5% existing in the soluble orthophosphate forms ($H_2PO_4^-$ and HPO_4^{2-}) accessible to plants (Hakim *et al.* 2021; Alzate Zuluaga *et al.* 2024). KBK3 likely mobilizes insoluble soil phosphates via a common PGPR mechanism: the secretion of low-molecular-weight organic acids (e.g., gluconic or citric acid). These compounds acidify the microenvironment and chelate metal cation (e.g., Ca^{2+}, Fe^{3+}, Al^{3+}), thereby releasing plant-available phosphate(Chandran *et al.* 2021; Saeed *et al.* 2021). This function aligns with well-characterized phosphate-solubilizing genera, including *Pseudomonas*, *Bacillus*, and *Streptomyces* (Mahdi *et al.* 2020; Soumare *et al.* 2021; Timofeeva *et al.* 2023; Wahab *et al.* 2024). The absence of direct antagonistic traits like HCN and chitinase production in KBK3 suggests its primary ecological role is nutrient facilitation rather than pathogen inhibition. Together, these multifunctional traits solidify KBK3's profile as a promising bioinoculant for improving plant nutrition and growth under nutrient-limiting conditions.

The enzymatic profile of *Aeromonas* sp. KBK3 further clarifies its functional niche within the rhizosphere. The production of cellulase and pectinase indicates a capacity to degrade key plant-derived polymers, contributing to organic matter turnover and nutrient cycling. Cellulase activity facilitates the breakdown of cellulose into simpler sugars, supporting soil carbon dynamics (Hakim *et al*. 2021; Shi *et al*. 2022; De Andrade *et al*. 2023; Sritongon *et al*. 2023). Pectinase, in turn, aids in the decomposition of pectin, a major component of plant cell walls, thereby promoting carbon mineralization and the release of nutrients from plant residue (El Hjouji *et al*. 2025; Hajji-Hedfi *et al*. 2025). Notably, pectinolytic activity has been positively correlated with increased rhizosphere colonization through biofilm formation (Shi *et al*. 2022). Conversely, the absence of detectable protease, chitinase, and amylase activities suggests a limited capacity for direct enzymatic antagonism against pathogens. Protease and chitinase are particularly associated with the biocontrol of fungal pathogens, as they degrade essential structural proteins and chitin in cell walls (Jadhav *et al*. 2017; Chandran *et al.* 2021; Hamada and Soliman 2023). The lack of these enzyme positions KBK3 closer to PGPR strains primarily involved in nutrient facilitation and organic matter transformation, rather than these specializing in direct pathogen suppression (Hakim *et al*. 2021; Hajji-Hedfi *et al*. 2025).

The functional profile of *Aeromonas* sp. KBK3, characterized by the absence of nitrogen fixation and hydrogen cyanide (HCN) production, further refines its ecological specialization toward mineral solubilization and organic matter decomposition rather than atmospheric nitrogen assimilation or direct cyanogenic antagonism. This does not detract from its plant growth-promoting potential, as many effective PGPR strains facilitate growth through mechanisms independent of biological nitrogen fixation. In non-leguminous systems, nitrogen acquisition often occurs via alternative pathways, and various beneficial bacteria, including some rhizobia, can promote growth in non-host plants through diverse direct and indirect mechanisms (Solomon *et al*. 2024). Similarly, the lack of detectable HCN aligns with finding for other highly effective PGPR isolate where cyanogenesis is not a prerequisite for plant-beneficial activity (Agunbiade *et al*. 2024). This absence may be advantageous, as it reduces potential risk while underscoring that KBK3's primary mode of action is likely rooted in enhancing nutrient bioavailability and participating in rhizosphere nutrient cycling, rather than in pathogen suppression via cyanide production.

Consistent with its nutrient-facilitating profile, *Aeromonas* sp. KBK3 exhibited no adverse effects on seed germination relative to the control, confirming its non-phytotoxic nature and compatibility with early seedling development. This non phytotoxic germination response aligns with reports for other mineral-solubilizing PGPR, such as strains of *Klebsiella, Enterobacter, Pseudomonas, Bacillus*, and *Serratia* (Mahdi *et al*. 2020; Fahsi *et al*. 2021; Salazar-Ramírez *et al*. 2021; Fiodor *et al*. 2023; Ganesh *et al*. 2024; Bhardwaj *et al*. 2025), further supporting its safety and potential for use as an agricultural inoculant.

5. CONCLUSION

This study identifies and characterizes *Aeromonas* sp. KBK3, a novel and robust plant growth-promoting rhizobacterium (PGPR) isolated from the banana rhizosphere. The isolate demonstrates a multifaceted profile of agronomically valuable traits. Its high potassium solubilization capacity (KSI 3.77 ± 0.27 within 4 days), combined with moderate indole-3-acetic acid production, and phosphate solubilization, directly addresses key constraints in plant nutrient acquisition. Furthermore, its enzymatic activities (cellulase, pectinase) suggest a complementary role in rhizosphere carbon cycling. The strain exhibits pronounced resilience to abiotic stressors, including salinity, pH variation, and osmotic drought—highlighting its adaptability to challenging soil environments. Critically, its non-phytotoxic nature, confirmed by a neutral effect on seed germination, ensures biological safety for agricultural application.

Collectively, the functional attributes, stress tolerance, and biosafety of *Aeromonas* sp. KBK3 underscore its significant potential as a next-generation microbial inoculant. It is a promising candidate for development into a biofertilizer aimed at enhancing nutrient use efficiency and crop resilience. Subsequent validation through controlled greenhouse trials and field studies is essential to confirm its efficacy and integrate it into sustainable crop production systems.

ACKNOWLEDGEMENTS

We extend our sincere gratitude to the Biotechnology Department and the Organic Farming and Natural Product Research Center (ONRC) at Kathmandu University, Dhulikhel, Nepal, for providing essential research facilities. We also thank Sanjeev Prasad Devkota, Khusbu Raut, Shusma Giri and Shristina Shrestha for their invaluable technical support.

REFERENCES

Abbott SL, Cheung WKW, Janda JM. 2003. The genus *Aeromonas* : biochemical characteristics, atypical reactions, and phenotypic identification schemes. J Clin Microbiol. 41(6):2348-2357. DOI: 10.1128/JCM.41.6.2348-2357.2003 PMID: 12791848 PMCID: PMC156557

Abd-Alla MH, Nafady NA, Hassan AA, Bashandy SR. 2024. Isolation and characterization of non-rhizobial bacteria and arbuscular mycorrhizal fungi from legumes. BMC Microbiol. 24(1):454. DOI: 10.1186/s12866-024-03591-z PMID: 39506644 PMCID: PMC11539435

Abeyta C, Kaysner CA, Wekell MM, Sullivan JJ, Stelma GN. 1986. Recovery of *Aeromonas hydrophila* from Oysters Implicated in an Outbreak of Foodborne Illness. J Food Prot. 49(8):643-647. DOI: 10.4315/0362-028X-49.8.643 PMID: 30959691

Abo-Shama UH, El Raheem AAA, Alsaadawy RM, Sayed HH. 2025. Phenotypic and genotypic characterization of *Aeromonas hydrophila* isolated from freshwater fishes at Middle Upper Egypt. Sci Rep. 15(1):5920. DOI: 10.1038/s41598-025-89465-4 PMID: 39966501 PMCID: PMC11836066

Abulhamd AT. 2009. Characterization of *Aeromonas hydrophila* isolated from aquatic environments using phenotypic and genotyping methods. :1-9.

Agunbiade VF, Fadiji AE, Agbodjato NA, Babalola OO. 2024. Isolation and Characterization of Plant-Growth-Promoting, Drought-Tolerant Rhizobacteria for Improved Maize Productivity. Plants. 13(10):1298. DOI: 10.3390/plants13101298 PMID: 38794369 PMCID: PMC11125291

Ahangarzadeh M, Ghorbanpour Najafabadi M, Peyghan R, Houshmand H, Sharif Rohani M, Soltani M. 2022. Detection and distribution of virulence genes in *Aeromonas hydrophila* isolates causing infection in cultured carps. Vet Res Forum. 13(1). DOI: 10.30466/vrf.2020.115998.2761

AlAli HA, Khalifa A, Almalki M. 2021. Plant growth-promoting rhizobacteria from *Ocimum basilicum* improve growth of *Phaseolus vulgaris* and *Abelmoschus esculentus*. South Afr J Bot. 139:200-209. DOI: 10.1016/j.sajb.2021.02.019

Alzate Zuluaga MY, Fattorini R, Cesco S, Pii Y. 2024. Plant-microbe interactions in the rhizosphere for smarter and more sustainable crop fertilization: the case of PGPR-based biofertilizers. Front Microbiol. 15:1440978. DOI: 10.3389/fmicb.2024.1440978 PMID: 39176279 PMCID: PMC11338843

Antonelli C, Narduzzi M, Ruzzi M, Testa A, Vettraino AM. 2025. Mining Microbial Niches: Sources of Bacteria for Enhancing Plant Growth and Resilience to pH, Salinity, Drought and *Phytophthora infestans*. Environ Microbiol Rep. 17(5):e70217. DOI: 10.1111/1758-2229.70217 PMID: 41108603 PMCID: PMC12535207,

Ashokkumar K, Krishnapriya KP, Dharshini SM, Dharani L, Prasath GA. 2025. Influence of Varying Concentrations of Indole-3-Acetic Acid (IAA) on Root Growth Characteristics of Blackgram (*Vigna mungo* L.) Varieties. J Curr Opin Crop Sci. 6(4):270-278. DOI: 10.62773/jcocs.v6i4.365

Basu A, Prasad P, Das SN, Kalam S, Sayyed RZ, Reddy MS, El Enshasy H. 2021. Plant Growth Promoting Rhizobacteria (PGPR) as Green Bioinoculants: Recent Developments, Constraints, and Prospects. Sustainability. 13(3):1140. DOI: 10.3390/su13031140 PMCID: PMC9904496

Bhardwaj I, Kumar V, Singh S, Sharma AJ, Kumari S, Bhardwaj N, Dulta K, Peter L, Verma R, Kumar N, et al. 2025. Evaluation of Stress-Tolerant *Serratia* and *Enterobacter* as PGPR for Nutrient Solubilization and Dose-Dependent Bioformulation to Enhance Tomato Seedlings. Plants. 14(14):2154. DOI: 10.3390/plants14142154 PMID: 40733392 PMCID: PMC12299828

Boubekri K, Soumare A, Mardad I, Lyamlouli K, Hafidi M, Ouhdouch Y, Kouisni L. 2021. The Screening of Potassium- and Phosphate-Solubilizing Actinobacteria and the Assessment of Their Ability to Promote Wheat Growth Parameters. Microorganisms. 9(3):470. DOI: 10.3390/microorganisms9030470 PMID: 33668691 PMCID: PMC7996285,

Bouizgarne B, Bakki M, Boutasknit A, Banane B, El Ouarrat H, Ait El Maalem S, Amenzou A, Ghousmi A, Meddich A. 2023. Phosphate and potash solubilizing bacteria from Moroccan phosphate mine showing antagonism to bacterial canker agent and inducing effective tomato growth promotion. Front Plant Sci. 14:970382. DOI: 10.3389/fpls.2023.970382 PMID: 36968412 PMCID: PMC10030999

Cappuccino JG, Welsh C. 2019. Microbiology: A Laboratory Manual. Twelfth edition. New York: Pearson.

Chandran H, Meena M, Swapnil P. 2021. Plant Growth-Promoting Rhizobacteria as a Green Alternative for Sustainable Agriculture. Sustainability. 13(19):10986. DOI: 10.3390/su131910986

Cheesbrough M. 2006. District laboratory practice in tropical countries: part 2. Second edition. Cambridge: Cambridge University Press. DOI: 10.1017/CBO9780511543470 PMCID: PMC2870630

Chen K, Arora R. 2011. Dynamics of the antioxidant system during seed osmopriming, post-priming germination, and seedling establishment in spinach (*Spinacia oleracea*). Plant Sci. 180(2):212-220. DOI: 10.1016/j.plantsci.2010.08.007 PMID: 21421363

Daniel AI, Fadaka AO, Gokul A, Bakare OO, Aina O, Fisher S, Burt AF, Mavumengwana V, Keyster M, Klein A. 2022. Biofertilizer: The Future of Food Security and Food Safety. Microorganisms. 10(6):1220. DOI: 10.3390/microorganisms10061220 PMID: 35744738 PMCID: PMC9227430

De Andrade LA, Santos CHB, Frezarin ET, Sales LR, Rigobelo EC. 2023. Plant Growth-Promoting Rhizobacteria for Sustainable Agricultural Production. Microorganisms. 11(4):1088. DOI: 10.3390/microorganisms11041088 PMID: 37110511 PMCID: PMC10146397

El Hjouji H, Qessaoui R, Chafiki S, Mayad EH, Houmairi H, Dari K, Bencharki B, Aassila H. 2025. Enhancement of Tomato Growth Through Rhizobacteria and Biocontrol

of Associated Diseases. Life. 15(7):997. DOI: 10.3390/life15070997
PMID: 40724500 PMCID: PMC12298581

Fahsi N, Mahdi I, Mesfioui A, Biskri L, Allaoui A. 2021. Plant Growth-Promoting Rhizobacteria Isolated from the Jujube (*Ziziphus lotus)* Plant Enhance Wheat Growth, Zn Uptake, and Heavy Metal Tolerance. Agriculture. 11(4):316. DOI: 10.3390/agriculture11040316

Fatema K, Mahmud NU, Gupta DR, Siddiqui MdN, Sakif TI, Sarker A, Sharpe AG, Islam T. 2024. Enhancing rice growth and yield with weed endophytic bacteria *Alcaligenes faecalis* and *Metabacillus indicus* under reduced chemical fertilization. Pereira SIA, editor. PLOS ONE. 19(5):e0296547. DOI: 10.1371/journal.pone.0296547
PMID: 38753661 PMCID: PMC11098348

Felsenstein J. 1985. Confidence Limits on Phylogenies: An Approach Using the Bootstrap. Evolution. 39(4):783.
DOI: 10.2307/2408678
PMID: 28561359

Fiodor A, Ajijah N, Dziewit L, Pranaw K. 2023. Biopriming of seed with plant growth-promoting bacteria for improved germination and seedling growth. Front Microbiol. 14:1142966. DOI: 10.3389/fmicb.2023.1142966
PMID: 36925481 PMCID: PMC10011460

Fu S-F, Wei J-Y, Chen H-W, Liu Y-Y, Lu H-Y, Chou J-Y. 2015. Indole-3-acetic acid: a widespread physiological code in interactions of fungi with other organisms. Plant Signal Behav. 10(8):e1048052. DOI: 10.1080/15592324.2015.1048052
PMID: 26179718 PMCID: PMC4623019

Ganesh J, Hewitt K, Devkota AR, Wilson T, Kaundal A. 2024. IAA-producing plant growth promoting rhizobacteria from *Ceanothus velutinus* enhance cutting propagation efficiency and Arabidopsis biomass. Front Plant Sci. 15:1374877. DOI: 10.3389/fpls.2024.1374877
PMID: 38807777 PMCID: PMC11131947

Gautam SP, Bundela PS, Pandey AK, Jamaluddin, Awasthi MK, Sarsaiya S. 2012. Diversity of cellulolytic microbes and the biodegradation of municipal solid waste by a potential strain. Int J Microbiol. 2012:1-12. DOI: 10.1155/2012/325907
PMID: 22518141 PMCID: PMC3299345

Hajji-Hedfi L, Wannassi T, Tawfeeq Al-Ani LK, Balbool BA, Tissaoui S, Mougou-Hamdane A, Hamdi W, Azeem AMA, Rebouh NY. 2025. Investigating the potential role of beneficial rhizobacteria for protecting grapevine health and promoting growth. Front Sustain Food Syst. 9:1619801. DOI: 10.3389/fsufs.2025.1619801

Hakim S, Naqqash T, Nawaz MS, Laraib I, Siddique MJ, Zia R, Mirza MS, Imran A. 2021. Rhizosphere Engineering With Plant Growth-Promoting Microorganisms for Agriculture and Ecological Sustainability. Front Sustain Food Syst. 5:617157. DOI: 10.3389/fsufs.2021.617157

Hamada MA, Soliman ERS. 2023. Characterization and genomics identification of key genes involved in denitrification-DNRA-nitrification pathway of plant growthpromoting rhizobacteria (*Serratia marcescens* OK482790). BMC Microbiol. 23(1):210.
DOI: 10.1186/s12866-023-02941-7
PMID: 37543572 PMCID: PMC10403818

Hassan MA, Noureldin EA, Mahmoud MA, Fita NA. 2017. Molecular identification and epizootiology of *Aeromonas veronii* infection among farmed *Oreochromis niloticus* in Eastern Province, KSA. Egypt J Aquat Res. 43(2):161-167. DOI: 10.1016/j.ejar.2017.06.001

Jadhav HP, Shaikh SS, Sayyed RZ. 2017. Role of hydrolytic enzymes of rhizoflora in biocontrol of fungal phytopathogens: an overview. In: Mehnaz S, editor. Rhizotrophs: plant growth promotion to bioremediation. Singapore: Springer Singapore. p. 183-203. DOI: 10.1007/978-981-10-4862-3_9

Khairnar Y, K. VK, B J, Mujapara A, Jhadav A, Gupta M, Gupta G, Patil P, Trivedi S, Gupta N. 2009. Study of pectinase production in submerged fermentation using different strains of *Aspergillus Niger*. Int J Microbiol Res. 1(2):13-17. DOI: 10.9735/0975-5276.1.2.13-17

KC BM., Gauchan DP, Khanal SN, Chimouriya S, Lamichhane J.,2020. Extraction of indole-3-acetic acid from plant growth promoting rhizobacteria of bamboo rhizosphere and its effect on biosynthesis of chlorophyll in bamboo seedlings, *Indian Journal of Agricultural Research*, 54 (6), 781-786. DOI: 10.18805/IJARe.A-5578

Kim E, Baek J, Lee PH, Hwang K-W, Moon JK, Koo Y. 2024. Isolation and Identification of Ginseng Growth Promoting Bacteria from Korean Ginseng Rhizosphere. Korean J Environ Agric. 43:290-300. DOI: 10.5338/KJEA.2024.43.28

Lakshmi BKM. 2014. Screening, optimization of production and partial characterization of alkaline protease from haloalkaliphilic *Bacillus* sp. Int J Res Eng Technol. 3(2):435-443. DOI: 10.15623/ijret.2014.0302077

Liu M, Zhang Q, Jin R, Zhao P, Zhu X, Wang J, Yu Y, Tang Z. 2023. The role of IAA in regulating root architecture of sweetpotato (*Ipomoea Batatas* [L.] lam) in response to potassium deficiency stress. Plants. 12(9):1779. DOI: 10.3390/plants12091779 PMID: 37176837 PMCID: PMC10181447

Mahdi I, Fahsi N, Hafidi M, Allaoui A, Biskri L. 2020. Plant Growth Enhancement using Rhizospheric Halotolerant Phosphate Solubilizing Bacterium *Bacillus licheniformis* QA1 and *Enterobacter asburiae* QF11 Isolated from *Chenopodium quinoa* Willd. Microorganisms. 8(6):948. DOI: 10.3390/microorganisms8060948 PMID: 32599701 PMCID: PMC7356859

Marathe SK, Vashistht MA, Prashanth A, Parveen N, Chakraborty S, Nair SS. 2018. Isolation, partial purification, biochemical characterization and detergent compatibility of alkaline protease produced by *Bacillus subtilis, Alcaligenes faecalis* and *Pseudomonas aeruginosa* obtained from sea water samples. J Genet Eng Biotechnol. 16(1):39–46. DOI: 10.1016/j.jgeb.2017.10.001 PMID: 30647702 PMCID: PMC6296584

Martin-Carnahan A, Joseph SW. 2015. *Aeromonas*. In: Trujillo ME, Dedysh S, DeVos P, Hedlund B, Kämpfer P, Rainey FA, Whitman WB, editors. Bergey's manual of systematics of archaea and bacteria. 1st ed. Wiley. p. 1-44.

Muzami EM, Kitundu G, Muriithi OM, Kavoo AM, Gichuru VG, Mbinda WM. 2025. Metagenomic insights to bacterial communities, functional traits, and soil health in banana smallholder agroecosystems of Kenya. Front Microbiol. 16:1582271. DOI: 10.3389/fmicb.2025.1582271 PMID: 40520380 PMCID: PMC12162901

Nawaz A, Qamar ZU, Marghoob MU, Imtiaz M, Imran A, Mubeen F. 2023. Contribution of potassium solubilizing bacteria in improved potassium assimilation and cytosolic K+/Na+ ratio in rice (*Oryza sativa* L.) under saline-sodic conditions. Front Microbiol. 14:1196024. DOI: 10.3389/fmicb.2023.1196024 PMID: 37711698 PMCID: PMC10497963

Noureen S, Iqbal A, Muqeet HA. 2024. Potential of Drought Tolerant Rhizobacteria Amended with Biochar on Growth Promotion in Wheat. Plants. 13(9):1183. DOI: 10.3390/plants13091183 PMID: 38732400 PMCID: PMC11085571

Olaniyan FT, Alori ET, Adekiya AO, Ayorinde BB, Daramola FY, Osemwegie OO, Babalola OO. 2022. The use of soil microbial potassium solubilizers in potassium nutrient availability in soil and its dynamics. Ann Microbiol. 72(1):45. DOI: 10.1186/s13213-022-01701-8

Pantoja-Guerra M, Valero-Valero N, Ramírez CA. 2023. Total auxin level in the soil-plant system as a modulating factor for the effectiveness of PGPR inocula: a review. Chem Biol Technol Agric. 10(1):6. DOI: 10.1186/s40538-022-00370-8

Posada LF, Ramírez M, Ochoa-Gómez N, Cuellar-Gaviria TZ, Argel-Roldan LE, Ramírez CA, Villegas-Escobar V. 2016. Bioprospecting of aerobic endospore-forming bacteria with biotechnological potential for growth promotion of banana plants. Sci Hortic. 212:81-90. DOI: 10.1016/j.scienta.2016.09.040

Rafedzi EAK, Bharudin I, Kamaruddin S, Abu Bakar FD, Abdul Murad AM. 2024. Effectiveness of the drought-tolerant plant growth promoting rhizobacteria (PGPR) that supports paddy growth in drought condition. J Pure Appl Microbiol. 18(1):297-310. DOI: 10.22207/JPAM.18.1.13

Raji M, Thangavelu M. 2021. Isolation and screening of potassium solubilizing bacteria from saxicolous habitat and their impact on tomato growth in different soil types. Arch Microbiol. 203(6):3147-3161. DOI: 10.1007/s00203-021-02284-9 PMID: 33818654

Raju EVN, Divakar G. 2013. PRODUCTION OF PECTINASE BY USING *BACILLUS CIRCULANS* ISOLATED FROM DUMP YARDS OF

VEGETABLE WASTES. Int J Pharm Sci Res. 4(7). DOI: 10.13040/IJPSR.0975-8232.4(7).2615-22

Reang L, Bhatt S, Tomar RS, Joshi K, Padhiyar S, Vyas UM, Kheni JK. 2022. Plant growth promoting characteristics of halophilic and halotolerant bacteria isolated from coastal regions of saurashtra gujarat. Sci Rep. 12(1):4699. DOI: 10.1038/s41598-022-08151-x PMID: 35304507 PMCID: PMC8933404

Roychoudhry S, Kepinski S. 2021. Auxin in root development. Cold Spring Harb Perspect Biol.:a039933. DOI: 10.1101/cshperspect.a039933 PMID: 34312248 PMCID: PMC9121899

Saeed Q, Xiukang W, Haider FU, Kučerik J, Mumtaz MZ, Holatko J, Naseem M, Kintl A, Ejaz M, Naveed M, et al. 2021. Rhizosphere Bacteria in Plant Growth Promotion, Biocontrol, and Bioremediation of Contaminated Sites: A Comprehensive Review of Effects and Mechanisms. Int J Mol Sci. 22(19):10529. DOI: 10.3390/ijms221910529 PMID: 34638870 PMCID: PMC8509026

Saheewala H, Sanadhya S, Upadhyay SK, Mohanty SR, Jain D. 2023. Polyphasic Characterization of Indigenous Potassium-Solubilizing Bacteria and Its Efficacy Studies on Maize. Agronomy. 13(7):1919. DOI: 10.3390/agronomy13071919

Saima, Kuddus M, Roohi, Ahmad IZ. 2013. Isolation of novel chitinolytic bacteria and production optimization of extracellular chitinase. J Genet Eng Biotechnol. 11(1):39-46. DOI: 10.1016/j.jgeb.2013.03.001

Salazar-Ramírez MT, Sáenz-Mata J, Preciado-Rangel P, Fortis-Hernández M, Rueda-Puente EO, Yescas-Coronado P, Orozco-Vidal JA. 2021. Plant growth-promoting rhizobacteria associated to candelilla rhizosphere (*Euphorbia antisyphilitica*) and its effects on *Arabidopsis thaliana* seedlings. Not Bot Horti Agrobot Cluj-Napoca. 49(2):12294. DOI: 10.15835/nbha49212294

Sandhya V, Sk. Z. A, Grover M, Reddy G, Venkateswarlu B. 2009. Alleviation of drought stress effects in sunflower seedlings by the exopolysaccharides producing *Pseudomonas putida* strain GAP-P45. Biol Fertil Soils. 46(1):17-26. DOI: 10.1007/s00374-009-0401-z

Sharma R, Sindhu SS, Glick BR. 2024. Potassium solubilizing microorganisms as potential biofertilizer: a sustainable climate-resilient approach to improve soil fertility and crop production in agriculture. J Plant Growth Regul. 43(8):2503-2535. DOI: 10.1007/s00344-024-11297-9

Shi P, Zhang J, Li X, Zhou L, Luo H, Wang L, Zhang Y, Chou M, Wei G. 2022. Multiple metabolic phenotypes as screening criteria are correlated with the plant growth-promoting ability of rhizobacterial isolates. Front Microbiol. 12:747982. DOI: 10.3389/fmicb.2021.747982 PMID: 35069464 PMCID: PMC8767003

Solomon W, Janda T, Molnár Z. 2024. Unveiling the significance of rhizosphere: implications for plant growth, stress response, and sustainable agriculture. Plant Physiol Biochem. 206:108290. DOI: 10.1016/j.plaphy.2023.108290 PMID: 38150841 PMCID: PMC13150743

Soumare A, Boubekri K, Lyamlouli K, Hafidi M, Ouhdouch Y, Kouisni L. 2021. Efficacy of phosphate solubilizing actinobacteria to improve rock phosphate agronomic effectiveness and plant growth promotion. Rhizosphere. 17:100284. DOI: 10.1016/j.rhisph.2020.100284

Sritongon N, Boonlue S, Mongkolthanaruk W, Jogloy S, Riddech N. 2023. The combination of multiple plant growth promotion and hydrolytic enzyme producing rhizobacteria and their effect on Jerusalem artichoke growth improvement. Sci Rep. 13(1):5917. DOI: 10.1038/s41598-023-33099-x PMID: 37041302 PMCID: PMC10090049

Sun F, Ou Q, Wang N, Guo ZX, Ou Y, Li N, Peng C. 2020. Isolation and identification of potassium-solubilizing bacteria from *Mikania micrantha* rhizospheric soil and their effect on *M. micrantha* plants. Glob Ecol Conserv. 23:e01141. b Ecol Conserv. 23:e01141. DOI: 10.1016/j.gecco.2020.e01141

Tamura K, Masatoshi Nei. 1993. Estimation of the number of nucleotide substitutions in the control region of mitochondrial DNA in humans and chimpanzees. Mol Biol Evol. DOI: 10.1093/oxfordjournals.molbev.a040023

Tamura K, Stecher G, Kumar S. 2021. MEGA11: molecular evolutionary genetics analysis version 11. Battistuzzi FU, editor. Mol Biol Evol. 38(7):3022-3027.

DOI: 10.1093/molbev/msab120
PMID: 33892491 PMCID: PMC8233496

Tatung M, Deb CR. 2023. Isolation, Characterization, and Investigation on Potential Multi-trait Plant Growth Promoting Rhizobacteria from Wild Banana (*Musa itinerans*) Rhizospheric Soil. J Pure Appl Microbiol. 17(3):1578-1590. DOI: 10.22207/JPAM.17.3.19

Timofeeva AM, Galyamova MR, Sedykh SE. 2023. Plant Growth-Promoting Soil Bacteria: Nitrogen Fixation, Phosphate Solubilization, Siderophore Production, and Other Biological Activities. Plants. 12(24):4074. DOI: 10.3390/plants12244074
PMID: 38140401 PMCID: PMC10748132,

Uzma M, Nisar A, Iqbal A, Hasnain S, Mahmoud MH, Rahim MA, Gull T, Castro-Muñoz R, Zongo E. 2025. Exploring the efficacy of drought tolerant, IAA-producing plant growth-promoting rhizobacteria for sustainable agriculture. Plant Signal Behav. 20(1):2452331. DOI: 10.1080/15592324.2025.2452331
PMID: 39813100 PMCID: PMC11740683

Wahab A, Bibi H, Batool F, Muhammad M, Ullah S, Zaman W, Abdi G. 2024. Plant growth-promoting rhizobacteria biochemical pathways and their environmental impact: a review of sustainable farming practices. Plant Growth Regul. 104(2):637-662. DOI: 10.1007/s10725-024-01218-x

Wan W, Qin Y, Wu H, Zuo W, He H, Tan J, Wang Y, He D. 2020. Isolation and Characterization of Phosphorus Solubilizing Bacteria With Multiple Phosphorus Sources Utilizing Capability and Their Potential for Lead Immobilization in Soil. Front Microbiol. 11:752. DOI: 10.3389/fmicb.2020.00752
PMID: 32390988 PMCID: PMC7190802

Wang C, Wu B, Jiang K. 2019. Allelopathic effects of Canada goldenrod leaf extracts on the seed germination and seedling growth of lettuce reinforced under salt stress. Ecotoxicology. 28(1):103–116. DOI: 10.1007/s10646-018-2004-7
PMID: 30547327

Wang M, Sun H, Dai H, Xu Z. 2024. Characterization of PlantGrowth-Promoting Rhizobacteria for Tea Plant (*Camellia sinensis*) Development and Soil Nutrient Enrichment. Plants. 13(18):2659. DOI: 10.3390/plants13182659
PMID: 39339634 PMCID: PMC11434996

Yaghoubi Khanghahi M, Strafella S, Allegretta I, Crecchio C. 2021. Isolation of bacteria with potential plant-promoting traits and optimization of their growth conditions. Curr Microbiol. 78(2):464-478. DOI: 10.1007/s00284-020-02303-w
PMID: 33354746 PMCID: PMC7864805

Yan H, Wang T, Wang H, Sun N, Wang X, Zhao X, Yao Z, Tian H, Chen S, Tang S, et al. 2024. Screening and Identification of Cold-Tolerant Phosphorus and Potassium Solubilizing Bacteria and Their Growth-Promoting Effects on Soybean in Cold Regions. Agronomy. 15(1):40. DOI: 10.3390/agronomy15010040

Yang D, Wang L, Wang T, Zhang Y, Zhang S, Luo Y. 2021. Plant Growth-Promoting Rhizobacteria HN6 Induced the Change and Reorganization of Fusarium Microflora in the Rhizosphere of Banana Seedlings to Construct a Healthy Banana Microflora. Front Microbiol. 12:685408. DOI: 10.3389/fmicb.2021.685408
PMID: 34354685 PMCID: PMC8329250

Yang P, Condrich A, Scranton S, Hebner C, Lu L, Ali MA. 2024. Utilizing Plant Growth-Promoting Rhizobacteria (PGPR) to Advance Sustainable Agriculture. Bacteria. 3(4):434-451. DOI: 10.3390/bacteria3040030

Yang Y, Shi Y, Tong C, Zhang D. 2025. Effects and Mechanism of Auxin and Its Inhibitors on Root Growth and Mineral Nutrient Absorption in Citrus (Trifoliate Orange, *Poncirus trifoliata*) Seedlings via Its Synthesis and Transport Pathways. Agronomy. 15(3):719. DOI: 10.3390/agronomy15030719

Physicochemical Properties of Soils from Grasslands and Forests in Two Protected Areas Across Temperate and Subtropical Zones of Nepal

Saraswati K.C[1], Sanu Raja Maharjan[1] and Deepa Dhital[2*]

[1] *Department of Environmental Science, Khwopa College, Kathmandu, Nepal*
[2] *Faculty of Science, Nepal Academy of Science and Technology (NAST), Kathmandu, Nepal*

***CORRESPONDING AUTHOR:**

Deepa Dhital
Email: dhital.deepa@gmail.com

ISSN : 2382-5359(Online), 1994-1412(Print)

DOI:
https://doi.org/10.3126/njst.v22i2.100111

Date of Submission: 14 Jan, 2025

Date of Acceptance: 5 Oct, 2025

ABSTRACT

Soil is the largest carbon reservoir, contains soil organic carbon (SOC) influenced by soil properties that is vital for soil fertility and carbon management. This study assessed physicochemical properties in grasslands and forests within the Annapurna Conservation Area (ACA) and Shivapuri Nagarjun National Park (SNNP) across temperate and subtropical zones. The soil temperature was lower and soil moisture was higher in the temperate ACA grassland, compared to sub-tropical SNNP, and in forests compared to the grasslands. Soil electrical conductivity was higher in ACA grasslands than forests, but lower in grassland than forests in SNNP, and overall lower in ACA than in SNNP. Both soil pH and bulk density were higher in grasslands than forests at ACA and SNNP, with a sandy loam soil texture across sites. Soil organic carbon (SOC) and organic matter were higher in ACA than SNNP, with ACA grasslands and SNNP forests showed the highest values. Soil properties differed significantly between grasslands and forests, with soil parameters varying across land uses and climate zones. Most soil characteristics apart SOC being more pronounced in temperate zone than in subtropical one. Hence, grassland and forest soils are key carbon sinks, and these soils require proper management, assessment and conservation.

Keywords: Soil properties, Land use type, Grassland, Forest, Temperate and subtropical zone

1. INTRODUCTION

Soil is the largest carbon reservoir in the terrestrial carbon cycle, holding nearly three times more carbon than all of Earth's vegetation combined (Sheikh et al. 2009). Carbon is stored in soil through contributions from aboveground organic biomass and root inputs (Beniston et al. 2014). Understanding how soil organic carbon (SOC) is distributed within the soil profile is vital for assessing soil fertility, health, carbon stock, and management practices, as this distribution varies across different vegetation types and land uses (Kopittke et al. 2022; Feeney et al. 2024). Research has shown significant variations in soil physicochemical parameters across different land use systems (Tellen et al. 2018).

The soil physicochemical properties like soil organic carbon (Shapkota et al. 2021), soil organic matter (Mayer et al. 2020), soil temperature and soil moisture (Tang et al. 2022), soil bulk density and pH (Zhang et al. 2018), soil texture (Iranmanesh and Sadeghi 2019) and electrical conductivity (Win et al. 2025) are the most recognized key factors influencing soil quality, vegetation growth, productivity, and carbon storage and sequestration, that might vary with seasonal variations, land use changes and ecological zones. More than 75% of SOC in the top meter of soil is directly influenced by human land use (Harden et al. 2018). The primary source of organic matter in soil comes from dead plant material (litter) derived from both above and below ground tissues (Mayer et al. 2020). Soil texture is one of the regulating elements that affects carbon sequestration and storage (Iranmanesh and Sadeghi 2019). The SOC levels in sandy soils are frequently low, and are considered to have a low capacity for sequestering SOC (Adhikari et al. 2017).

Nepal's grasslands cover 1.75 million hectares, providing crucial services like water filtration, biodiversity preservation, and soil erosion control (Shrestha et al. 2016). According to estimates, 0.2-0.8 Gt CO_2 per year can be absorbed in grassland soils by 2030 if management practices are altered (Ghosh et al. 2014). At the same time forests are believed to store the largest amount of carbon in terrestrial ecosystems (Bonan et al. 2008). The SOC concentration in the forest soil was significantly greater than that of other land uses (Alidoust et al. 2018). There are an estimated 726 million ha of forest in protected areas worldwide (FAO 2020).

There are currently more than one trillion tons of carbon stored in the world's forests and soils (Oli et al. 2009). Forests contain significant amounts of SOC, which must be preserved to prevent climate change (Ali et al. 2020). The SOC sequestration is influenced by temperature, soil, tree species, management practices, and litter composition (Lal et al. 2005). Accurate estimates of SOC decomposition and carbon emissions are vital for carbon modeling and decision-making (Zhong et al. 2017, Dhital et al. 2019, 2022b). Forest and grassland soils store significant carbon (Meena et al. 2018), and forests impact carbon storage capacity (Subashree et al. 2019). Protected areas store 0.5 Pg of carbon annually, but this is expected to decrease by 2100 due to climate change (Melillo et al. 2016). Land use changes may convert 5.6 million km² of protected areas (Panchal et al. 2022).

Measuring soil parameters helps predict the long-term effects of land use and climate changes (Bhutia et al. 2021). Plant remains contribute most carbon inputs to ecosystems (Paustian et al. 2019). Soils in cold, high-altitude areas store significant belowground carbon but are sensitive to climate change (Pan et al. 2011, Dhital et al. 2022a). Estimating key soil property like SOC can be enhanced using climate proxies like elevation, land use, soil practices, and vegetation (Wiesmeier et al. 2019). This study aimed to examine the various soil physicochemical properties, including temperature, moisture content, electrical conductivity, pH, bulk density, texture, organic carbon and organic matter of the soil, in the different land use types such as grasslands and forests of the temperate and subtropical zones within the Annapurna Conservation Area (ACA) and Shivapuri Nagarjun National Park (SNNP) in protected areas of Nepal.

2. MATERIAL AND METHODS

2.1 Study Site

2.1.1 Grassland (ACA Grassland 1) and forest (ACA Forest 1) site of the Annapurna Conservation Area

The temperate grassland site (ACA Grassland 1) and forest site (ACA Forest 1) of size 100m×100m in the Annapurna Conservation Area (ACA) was selected for this study which is located in the Ghorepani area. The grassland site is situated at an elevation of 2900 m asl (Figure 1i). Sampling points were chosen within the coordinates 28°24'211.1" N latitude and 83°41'752" E longitude. The plant species like *Potentila fulgens*, *Rumex nepalensis, Hemiphragma heterophyllum* etc., were dominated in the ACA grassland 1. The grassland was surrounded by Rhododendron (*Rhododendron arboreum*) forests and moderately grazed with minimal human disturbance. The forest site is located at the coordinates between 28°24'5.41" N latitude and 83°42'11.9" E longitude. It is situated at an altitude of 2870 m asl (Figure 1i). The forest is primarily dominated by Rhododendron (*Rhododendron arboreum*) trees, with a few *Acer spp.* also present in the forest. It is a deciduous temperate forest, free from human disturbances as it is located in a protected area.

The Ghorepani area falls within the temperate climatic zone, with the average annual temperature over the past ten years (2013–2022) reaching a maximum of 20.4°C and a minimum of 12.13°C. Air temperature consistently increased above 20°C from June to August, while temperature dropped below 12°C from December to February. Over the period, total annual precipitation of the study site was recorded 2557.56 mm, with the highest rainfall recorded in July (666.98 mm) Likewise (Figure 2a).

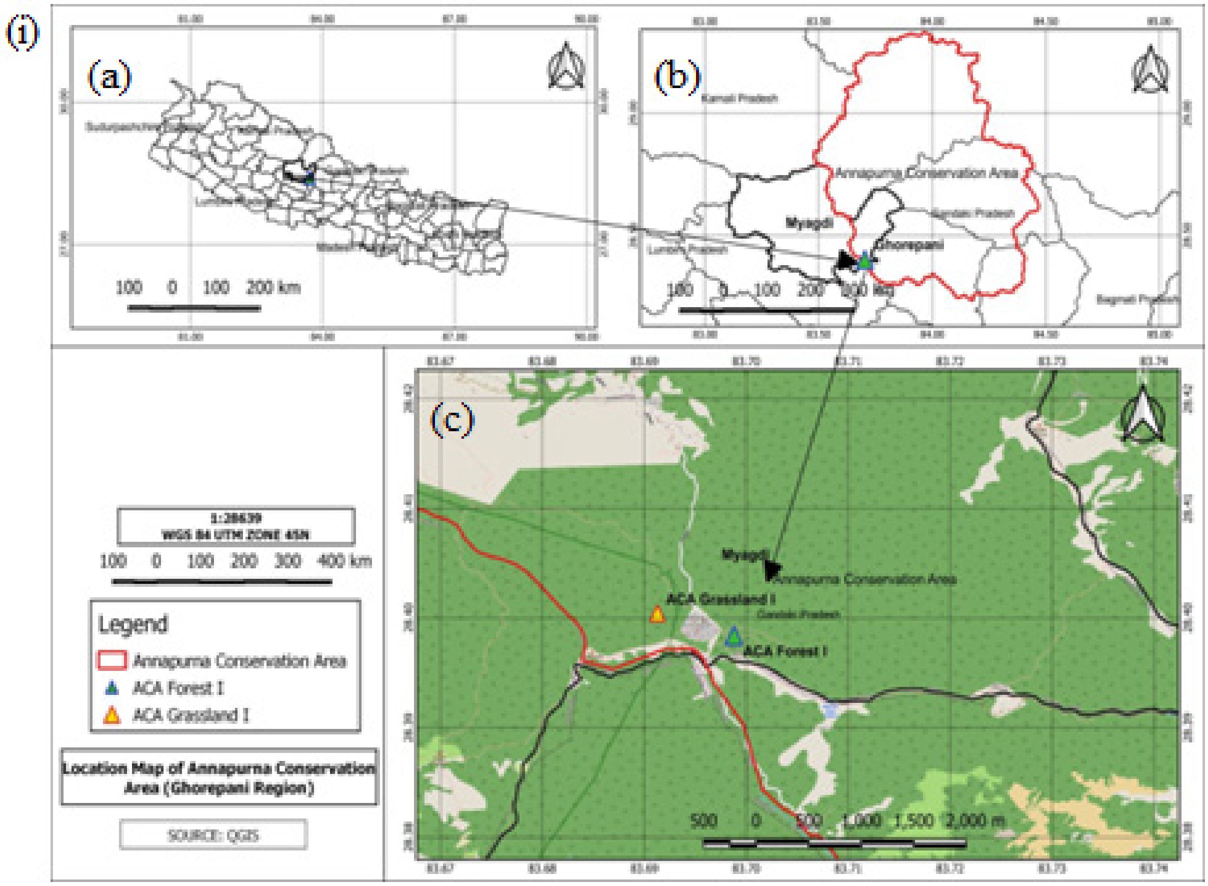

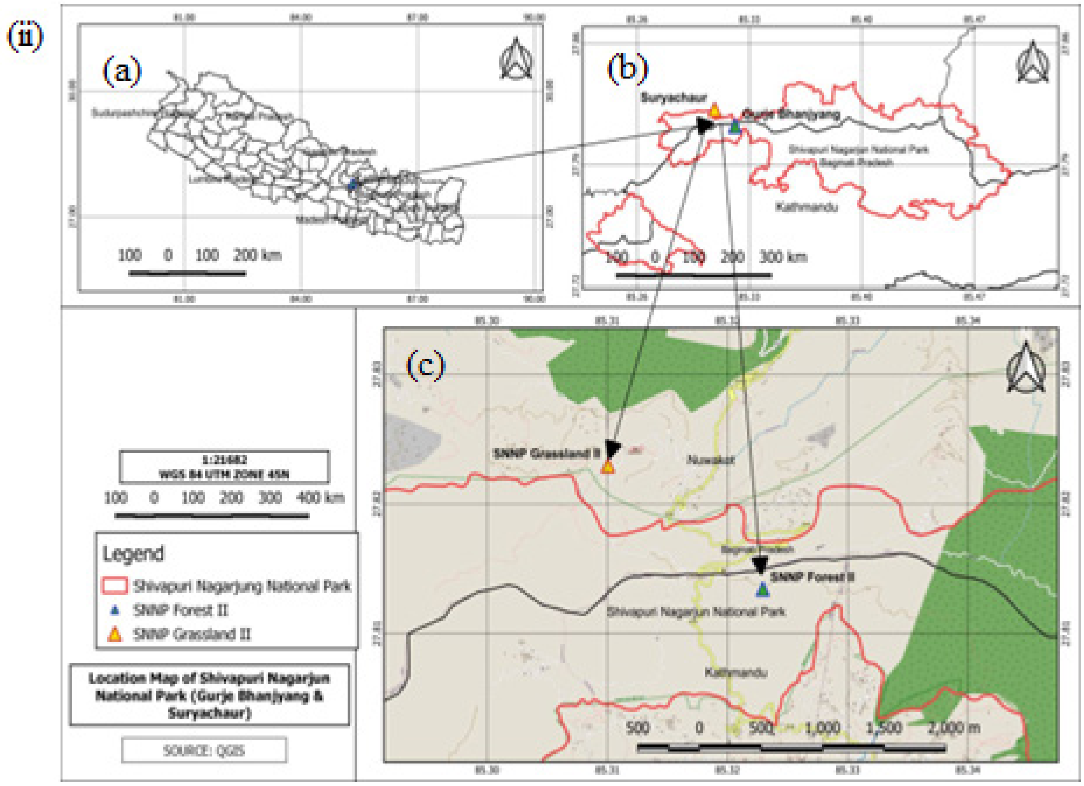

Fig 1: *Location map of (i) (a) Annapurna Conservation Area (ACA) in Nepal (b) Ghorepani in ACA (c) Grassland I and forest I in Ghorepani and (ii) (a) Shivapuri-Nagarjun National Park (SNNP) in Nepal (b) Study site in SNNP (c) grassland II and forest II in the study site*

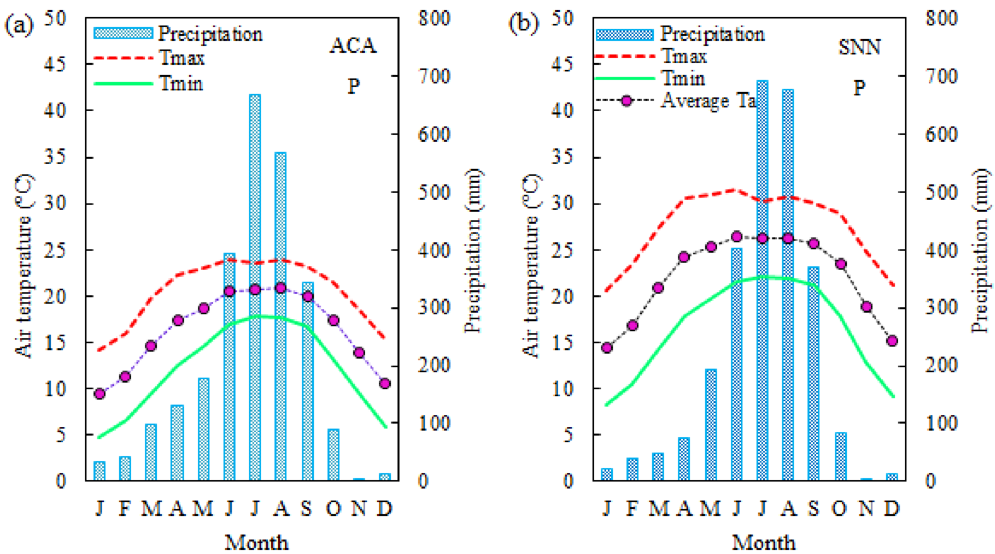

Fig 2: *Monthly average ten years mean (from 2013 to 2022) precipitation, and maximum and minimum air temperatures of (a) Ghorepani in ACA and (b) Kakani in SNNP (Source: Department of Hydrology and Meteorology, Government of Nepal, Kathmandu, Nepal)*

2.1.2 Grassland (SNNP Grassland 2) and forest (SNNP Forest II) site of Shivapuri Nagarjun National Park

The sub-tropical grassland (SNNP Grassland 2) and forest (SNNP Forest II) of sampling plot size 100m×100m in the Shivapuri Nararjun National Park (SNNP) was selected for this study. The grassland lies within 27°48′48″ to 27°49′17″N latitude and 85°18′31″ to 85°19′17″E longitude in the Suryachaur area. The altitude was 1979 m asl (Figure 1ii). The plant species like *Ageratina adenophora*, *Artemisia vulgaris*, *Melastoma malabathricum* etc., are dominated in the SNNP grassland II. The area was over grazed and frequent human disturbances was observed. The forest is located in the Gurje bhanjyang area of the Shivapuri-Nararjun National Park (SNNP), with the coordinates 27°48′48″N latitude to 85°19′20″E longitude and lies at 1882 m asl altitude (Figure 1ii). The forest is dominated with *Pinus roxburghii*, *Castanopsis indica* and *Schima wallichii*, etc. It is a mixed forest with minimal human disturbance.

The study site in the Shivapuri-Nagarjun National Park (SNNP) area falls within the sub-tropical climatic zone, with the average annual temperatures over the past ten years (2013–2022) reaching a maximum of 27.5°C and a minimum of 16.4°C. Air temperatures from June to August increased above 26°C and dropped below 15°C from December to February. The total of annual precipitation over the period of ten years in this study site was recorded as 2612.2 mm, with the highest rainfall recorded in July at 690.6 mm in average (Figure 2b).

2.2 Methods of Data Collection

2.2.1 Sampling design

The study area was categorised into grasslands and forest sites within the Annapurna Conservation Area (ACA) in the Temperate zone and the Shivapuri-Nagarjun National Park (SNNP) in the Subtropical zone of Nepal. The study area of size 70m×70m were selected in the ACA Grassland I, ACA Forest I, SNNP Grassland II and SNNP Forest II within the grasslands and forests in each site for sample collection and measurements. The sampling and measurements were conducted in pre-monsoon season, from March to May in the year 2023.

2.2.2 Soil sample collection

A total of 15 random sampling points were selected from 15 subplots in the study area of ACA Grassland I, ACA Forest I, SNNP Grassland II and SNNP Forest II for soil sample collection to make sure every part of the site was included, and precise data collection and representation. Samples were taken from a depth of 15 cm at each site using a stratified random sampling approach. The sample was taken with a sampler volume 117.75 cm^3 (a metallic cylinder with a diameter of 5 cm and a height of 6 cm). Zip lock polythene bags were used to collect the soil sample. The geographical coordinates and elevations of the sampling sites were recorded using the GPS (global positioning system). For bulk density analysis, soil samples were taken up to 15 cm depth. Additionally, 300 gm soil samples were collected for soil properties analysis. At the sampling locations, soil temperature was measured. The collected soil samples were carried to the laboratory at the Nepal Academy of Science and Technology (NAST) immediately after collection and were then processed for the necessary laboratory analysis for the measurements of moisture content, electrical conductivity (EC), pH, bulk density (BD), texture, organic carbon (SOC) and organic matter (OM) of the soil.

2.2.3 Soil temperature measurement

The soil temperature at a depth of 5 cm from the study sites in the grasslands and forests of ACA and SNNP was recorded using a digital lab stem thermometer (MEXTECH Multi-Stem Thermometer, ST9283B, India) during the soil sample collection period.

2.2.4 Moisture content (MC) measurement

A total of 50 g fresh soil sample was weighed and kept at 100°C in an oven for 48h in order to determine its moisture content. The oven-dried soil sample was left for 24 hrs to cool down and weighed. The same steps were followed for all soil samples to determine the moisture content.

The percent of moisture content was calculated by using formula:

% of Moisture content = $\frac{W1-W2}{W1} X\ 100$

Where,

W1 = Initial weight of sample

W2 = Final (air dry) weight of sample

2.2.5 Soil electrical conductivity (EC) measurement

A digital conductivity meter was used to measure soil EC. The 20 gm of soil was taken in a beaker and 40 ml of distilled water was added and it was vigorously stirred. Then, left for an hour with continuous stirring. The electrode of the EC meter was dipped into the beaker, and the obtained value was noted. After determination of each sample, electrode was rinsed with distilled water (Smith and Doran 1997).

2.2.6 Soil pH measurement

Using a digital pH meter, the soil pH was determined. At first, a beaker was taken and 20 g soil sample was placed in the beaker. Then 40 ml of distilled water was poured ointo the sample. Further, the mixture was gently stirred for 5 minutes with a clean glass rod, and was left for 30 minutes to allow the suspension to settle. Then, a pH meter was calibrated before the measurement using buffer solution. The electrode was then placed into the beaker to get a pH reading.

2.2.7 Bulk density (BD) measurement

Bulk density (BD) of soil was determined by using the core method (Blake and Hartge,1986). The soil sample of volume 117.7 g cm^{-3} was sampled from the study sites and at the laboratory of NAST and oven dried at 105°C for 24 hours. The BD was estimated by:

$$\text{Bulk Density (BD)} = \frac{\text{Weight of oven dried soil}}{\text{Volume of Core Sampler (V)}}$$

Where, V is the volume of core sampler auger in cm^3

Volume of core sampler was calculated by using formula:

$$\text{Volume (V)} = h \times \Pi r^2$$

Where, V is the volume of the soil in the core sampler in cm^3,

'h 'is the height of the core sampler in cm and,

'r 'is the radius of the core sampler in cm

2.2.8 Soil texture measurement

The soil texture of the sample was determined by using hydrometer (Pradhan et al. 1996). A 50 g of soil was transferred to 1000 ml jar and 100 ml of sodium hexametaphosphate was added. To that suspension on 250 ml of distilled water was added, stirred well and left overnight. Day after, water was added to the solution up to 1000ml, cork was placed and shaked well. The mixture was then left for sediment action for 40 seconds. After 40 seconds, initial reading was observed, was left for 3 hours for particles settlement and the final reading was taken. Lastly, blank (without soil sample) reading was taken. The temperature of the solution was also noted using a thermometer.

The soil texture was calculated using a formula,

(Silt+ clay) %= Hydrometer reading at 40 second + 0.3 * (t-20°C)

Clay %= Reading after 3 hours + 0.3 * (t-20°C)

Sand %= 100 − (Silt + clay) %

Silt %= (Silt + clay) % − Clay %

According to obtained proportions of sand, silt and clay, soil textural classes of the samples were calculated.

2.2.9 Soil organic carbon (SOC) measurement

Soil organic carbon (SOC) was determined by titrimetric method (Walkley and Black 1934). A total of 0.25 g of the soil was taken in a dried 500 ml conical flask, to which 10 ml of normal potassium dichromate (1N $K_2Cr_2O_7$) was added. Then, 20 ml of sulphuric acid (H_2SO_4) was added and was gently stirred. The mixture was left for half an hour. During this time, the potassium dichromate oxidizes the organic carbon present in the soil. After 30 minutes, 100 ml of distilled water was added to dilute the suspension of the flask and cooled. Then, 10 ml of phosphoric acid and 1 ml of diphenylamine indicator were added. After that, the sample was titrated with 0.5N ferrous ammonium sulphate (FAS) to notice the endpoint. At the endpoint, the colour turned into brilliant green. Further, for blank sample, same amount of chemical was used in the process. The blank titration was run without the soil and the endpoint was noted. The soil organic carbon content (SOC%) was calculated using the formula:

$$\frac{(\text{Blank reading} - \text{Titration reading}) \times N \times 0.003 \times 100}{\text{Weight of soil (g)}}$$

Here,

N= Normality of ferrous ammonium sulphate

0.003 is a factor to convert the amount of dichromate into organic carbon.

The carbon stock of soil was calculated as,

SOC Stock= $\rho \times d \times \%C$

Where,

SOC = Soil organic carbon stock per unit area (t ha^{-1})

ρ = Soil bulk density (g cm^{-3})

d = The total depth at which the sample was taken (cm) and

%C = SOC (%)

2.2.10 Soil organic matter (SOM) measurement

The soil organic matter (SOM) was estimated by multiplying the soil organic carbon content by a conversion factor of 1.724, since SOM is typically considered to contain about 58% organic carbon on average i.e. 100% (SOM)/58% (SOC) (Douglas 2010).

Then,

Soil organic matter (%) = Total soil organic carbon % × 1.724

2.3 Statistical Analysis

The mean values and standard errors of soil physicochemical parameters were calculated for both land use types in temperate and subtropical climates. A t-test and correlation analysis were conducted using Microsoft Excel (version 2013) and R (version 4.3.2) to compare soil property differences ($p<0.05$) and correlate MC, EC, pH, BD, SOC, and OM.

3. RESULTS

3.1 Soil Temperature

In the Annapurna Conservation Area (ACA), the average soil temperature at a 5 cm depth was recorded at 9.9°C in ACA grassland I (n=15), while in ACA forest I, it was 5.2°C. Similarly, in the Shivapuri-Nagarjun National Park (SNNP), the soil temperature at a 5 cm depth was measured at 21.5°C in SNNP grassland II and 15.1°C in SNNP forest II. The soil temperatures across the different land use types showed statistically significant ($p<0.05$) variation (Figure 3a).

3.2 Soil Moisture Content (MC)

The soil moisture content in the ACA grassland I and forest I were measured at 20.7% and 22.3%, respectively. Similarly, the average soil moisture content (n=15) in the SNNP grassland II and forest II were 20.1% and 18.5%, respectively. This indicates that the grassland and forest in the temperate climatic zone in ACA had higher soil moisture content compared to the subtropical zone (Figure 3b). However, the differences in soil moisture content between these two climatic zones were not statistically significant ($P>0.05$, i.e., 0.33 in grassland and 0.56 in forest).

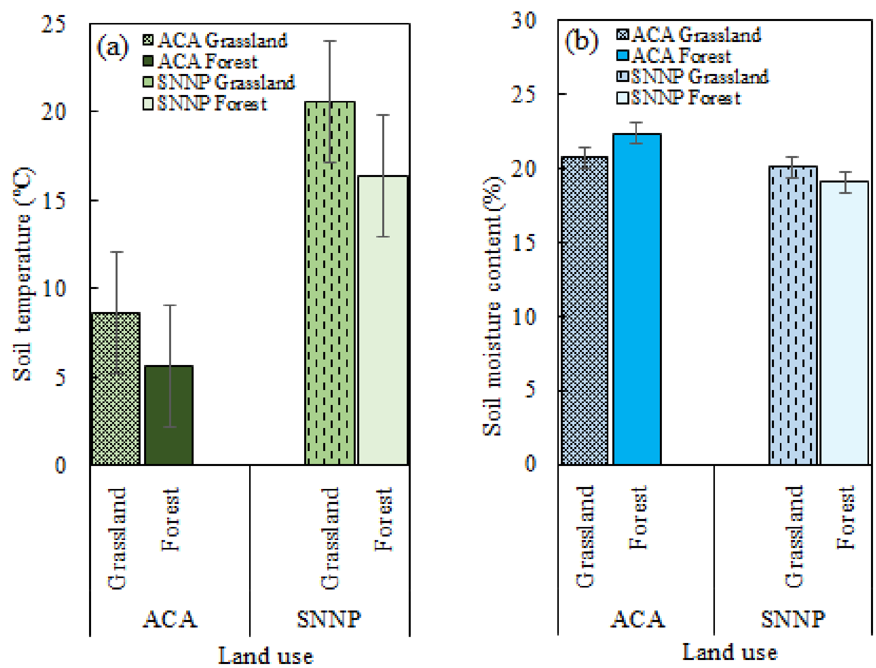

***Fig 3:** (a) Soil temperature and (b) soil moisture content variations in two land use types; grasslands and forests in ACA and SNNP; Error bar-Standard error*

3.3 Soil Electrical Conductivity (EC)

The average (n=15) soil electrical conductivity (EC) of ACA grassland I was 296 µs cm^{-3}, while that of the forest was 260 µs cm^{-3}, indicating that the grassland soil had a higher EC than the forest. In contrast, the average EC of SNNP grassland II was 270 µs cm^{-3}, whereas the forest had a higher EC of 358 µs cm^{-3} (Figure 4a), meaning the grassland soil had a lower EC compared to the forest. Statistical analysis of the EC values showed no significant difference between the land use types ($P>0.05$).

3.4 Soil pH

The average pH of ACA grassland I was 6.35 (n=15), which is nearly neutral and indicates a weakly acidic soil pH. In contrast, the pH of ACA forest I soil was 4.86, which is acidic. The mean pH of SNNP grassland II was 6.31, also nearly neutral, while the pH of SNNP forest II soil was 4.7, indicating acidity (Figure 4b) . Both the ACA and SNNP forest soils were found to be acidic, while the grasslands were nearly neutral. Statistically significant differences in soil pH were observed between the different land use types ($p<0.05$).

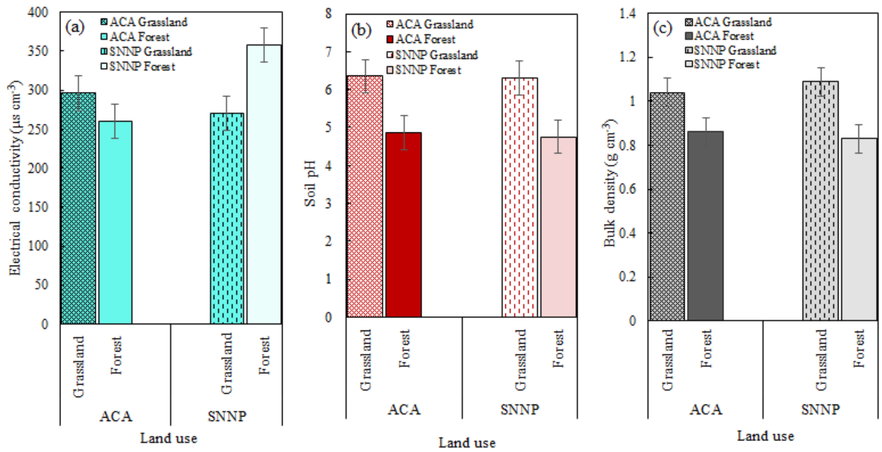

Fig 4: *(a) Soil electrical conductivity (µs cm^{-3}) (b) soil pH and (c) bulk density (g cm^{-3}) variations in two land use types in ACA and SNNP; Error bar-Standard error*

3.5 Soil Bulk Density (BD)

The average bulk density of the ACA grassland I was 1.04 g cm^{-3} (n=15), while the forest I had a BD of 0.86 g cm^{-3}. In the SNNP, average BD was 1.09 g cm^{-3} in grassland II and 0.83 g cm^{-3} in forest II (Figure 4c). The findings indicated that the grasslands at both study sites had a higher BD compared to the forest sites. Significant variations ($p<0.05$) in BD were observed between different land use types within the same climatic zone.

3.6 Soil Texture

In both ACA and SNNP, forest soils (n=15) had a greater average clay percentage than grassland soils, with values of 16.4% and 11.7% for forests, and 13.9% and 9.0% for grasslands, respectively.

However, the clay percentage was higher in the ACA than the SNNP in both forests and grasslands (Figure 5a). The clay percentage was statistically not varied ($p>0.05$) in grassland and forest of the ACA, while it was significantly varied ($p<0.05$) in SNNP sites. The sand percentage in grassland soils was higher than in forest soils for both the Annapurna Conservation Area (ACA) and Shivapuri-Nagarjun National Park (SNNP), with values of 72.9% and 78.6% for grasslands, and 65.5% and 74.9% for forests, respectively. Thus, it shows that the soil under forests have less sand percent (Figure 5b). The statistical calculation justified for significant variation in sand percentage between land use type in both climatic zones ($p<0.05$). The silt percentage in ACA and SNNP grasslands have less silt percentage was (13.2% and 12.4%), than the respective forests was (18.1% and 13.4%) (Figure 5c). The statistical calculation revealed that there was significant ($p<0.05$) variation between grassland and forest of ACA, whereas no significant variation ($p>0.05$) in grassland and forest of SNNP region. The overall estimation of the soil texture on the basis of the soil particle sizes the study sites among grasslands and forests indicated that all of the soils have sandy loam texture, characterized by high percentage of sand (greater than 50% in all cases), moderate to low percentages of clay (between 8-17%) and moderate amounts of silt (12-18%) (Table 1).

Table 1: Soil particle size distribution and texture in two land use types in the Annapurna Conservation Area (ACA) and Shivapuri-Nagarjun National Park (SNNP)

Particle size distribution				
Land use type	**Clay %**	**Sand %**	**Silt %**	**Texture**
ACA Grassland	13.9 ±3.46	72.9 ±7.67	13.2 ±4.59	Sandy loam
ACA Forest	16.38 ±3.49	65.49 ±6.46	18.13 ±3.31	Sandy loam
SNNP Grassland	8.97 ±2.46	78.63 ±3.44	12.4 ±1.76	Sandy loam
SNNP Forest	11.7 ±2.83	74.9 ±4.27	13.4 ±2.41	Sandy loam

± indicates Standard error (SE)

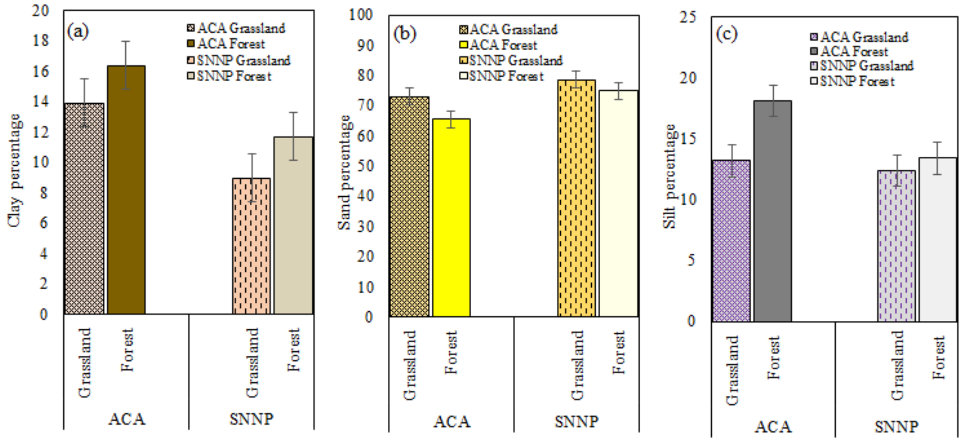

Fig 5: *(a) Clay, (b) sand and (c) silt percentage (%) variations in the grasslands and forests of ACA) and (SNNP); Error bar-Standard error*

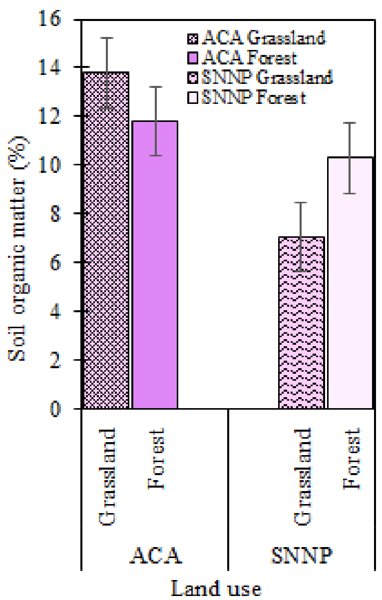

Fig 6: *Soil organic matter variation in two land use types in ACA and SNNP; Error bar-Standard Error*

3.7 Soil Organic Matter (SOM)

The soil under ACA grassland I had an average (n=15) organic matter content of 13.8%, while the forest I soil contained 11.3%, which was comparatively lowered than the grassland I. In the SNNP region, the grassland II soil had an average organic matter content of 6.1%, while the forest II soil had 10.1%, showing a higher organic matter content in the forest compared to the grassland. Statistical analysis revealed significant differences ($p<0.05$) in soil organic matter across the various land use types in these study sites.

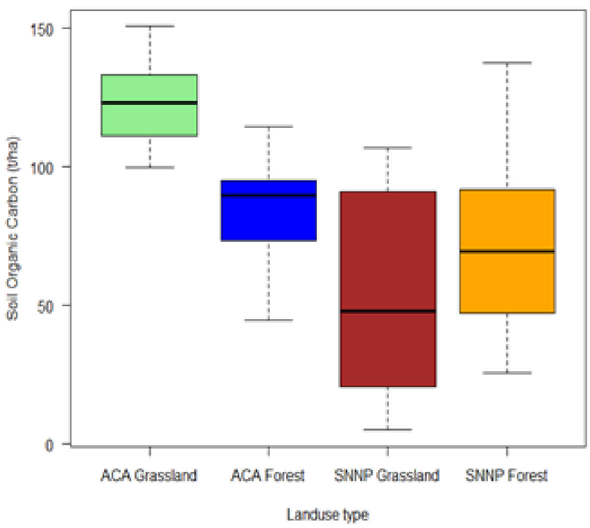

Fig 7: *Soil organic carbon (SOC, t ha^{-1}) variations in the grasslands and forests of ACA and SNNP; Error bar-Standard error*

3.8 Soil Organic Carbon (SOC)

This study found that the average soil organic carbon (SOC) in ACA grassland I across all sampling sites (n=15) was 123.2 t ha^{-1}, which was the highest value recorded among both climatic zones. In comparison, the SOC in the ACA forest I soil was 84.6 t ha^{-1}. The lowest SOC value was observed in the SNNP grassland II, with an average of 55.5 t ha^{-1}, while the forest II site in the SNNP region had 71.7 t ha^{-1} (Figure 6). Statistical analysis revealed that there were significant differences ($p<0.05$) in SOC levels between the two land use types i.e. grassland and forest across both climatic zones.

3.9 Correlations between the soil physicochemical properties

Correlation between various physicochemical properties of soil was analysed in the grasslands and forests of the two climatic zones in the Annapurna Conservation Area (ACA) and the Shivapuri-Nagarjun National Park (SNNP). In the ACA grassland I, pH, Electrical conductivity (EC), organic matter (OM), and moisture content (MC) all showed negative correlations with bulk density (BD) (r = -0.16, -0.29, -0.74, and -0.59, respectively), indicating if BD increases, these properties decrease, and vice versa. However, SOC showed no significant correlation with BD (r = 0.01).

All other soil properties, except BD, were positively correlated with each other. In the ACA forest, soil pH and EC exhibited positive correlations with OM and MC, while pH showed a negative correlation with EC, SOC, and BD. The EC had a significant ($p<0.05$) negative correlation with SOC (r = -0.57). The SOC was negatively correlated with both MC and BD (r = -0.23, -0.15), and OM also had negative correlations with MC% and BD (r = -0.22, -0.31) (Table 2).

Table 2: Correlation between soil properties in the grassland and forest of the ACA

Soil properties	pH	EC	SOC	OM	MC	BD
Grassland						
pH	1					
EC	0.22	1				
SOC	0.06	0.26	1			
OM%	0.21	0.38**	0.65**	1		
MC%	0.13	0.41**	0.23	0.61**	1	
BD	-0.17	-0.29	0.01	-0.74**	-0.59**	1
Forest						
pH	1					
EC	-0.13	1				
SOC	-0.06	-0.57	1			
OM %	0.10	0.12	0.09	1		
MC %	0.38	0.31	-0.23	-0.23	1	
BD	0.38	0.22	-0.15	-0.32	0.19	1

**Significant at P<0.05

Table 3: Correlation between soil properties in the grassland and forest of the SNNP

Soil properties	pH	EC	SOC	OM %	MC %	BD
Grassland						
pH	1					
EC	0.23	1				
SOC	0.25	0.37	1			
OM %	0.23	0.43	0.99	1		
MC %	0.23	-0.24	0.17	0.19	1	
BD	0.18	-0.50	-0.48	-0.55	-0.38	1
Forest						
pH	1					
EC	-0.55	1				
SOC	-0.29	0.26	1			
OM %	-0.32	0.4	0.93	1		
MC %	-0.56	0.56	0.21	0.39	1	
BD	0.23	-0.38	0.12	-0.22	-0.57	1

**Significant at $P<0.05$

In the SNNP grassland I, EC, SOC, OM, and MC were all negatively and significantly ($p<0.05$) correlated with BD (r = -0.50, -0.48, -0.55, -0.38), while pH showed a positive correlation with BD (r = 0.18). The correlation between EC and MC was negative but insignificant ($p>0.05$, r = -0.23). In the SNNP forest II, pH had a negative correlation with EC, SOC, OM, and MC (r = -0.55, -0.29, -0.32 and -0.56). Additionally, EC showed positive and significant ($p<0.05$) correlations with OM and MC (r = 0.40 and 0.56). Other soil properties were positively correlated with each other, with SOC and OM showing a strong positive and significant ($p<0.05$) correlation (Table 3).

4. DISCUSSION

The variations in soil and air temperature beneath the canopy and in open areas were strongly associated with solar radiation and the changes in solar energy and heat passing through the soil surface (Onwuka et al. 2018). In the hot season, area with less canopy absorbed heat and this supported for greater temperature in grassland area. Further, according to Morecroft et al. (1998), at two sites in the deciduous forest, it was found that forest soil temperature didn't rise above 20°C and this outcome supported for lower soil temperature of both forest areas of our study compared to the grassland of the similar zone. However, the soil temperature in the ACA region of the temperate zone is lower in both land use types i.e. grassland and forest compared to the sub-tropical zone of this study (Figure 3a). The presence of the tree canopy causes forest soil to experience more stable temperatures compared to the fluctuating temperatures in grassland soil (Lozano-Parra et al. 2018), which results in differing vegetation responses to soil temperature variations in the forest and grassland ecosystems (Luis et al. 2021).

Precipitation increases soil moisture and decreases soil temperature (Shi et al. 2011). This result supported higher moisture (Fig. 3b) and lower temperature (Fig. 3a) in ACA grassland and forest, compared to the subtropical zone. Forest soil moisture varies with vegetation density and rainfall; for example, Bangladesh's forest moisture ranged from 5 to 18% (Islam et al. 2016). In this study, ACA grassland (20.7%) and SNNP grassland (20.1%) had similar moisture, while ACA forest (22.3%) had higher moisture than SNNP forest (19.0%) (Fig. 3b), which was less dense and more disturbed. Zhou et al. (2019) found low average soil moisture in forests with significant temporal variation, but more moisture was present in forests with increased rainfall compared to grasslands. Ghosh et al. (2020) reported, moisture content ranging from 3.41 to 28% in temperate forest soil at Jaldapara National Park, similar to our study, where soil moisture in the ACA temperate forest ranged from 13.14 to 26.32%.

Soil electrical conductivity (EC) indicates salt content and the availability of water and nutrients for plants. A decline in EC with lower soil temperature and increase with higher organic matter (OM) content was observed in forests (Dar et al. 2018). In this study, ACA forest had lower EC (260 $\mu s\ cm^{-3}$) in the temperate zone, while SNNP forest had higher EC (358 $\mu s\ cm^{-3}$) in the subtropical region (Fig. 4a) which may be because of higher soil temperature and lower OM content. The study by Chaneton and Lavado (1996) found that salinization was higher in grazed grasslands. In our study, the ACA grassland I (296 $\mu s\ cm^{-3}$) in the temperate zone had higher EC, likely due to seasonal grazing, which may have contributed to the increased EC in the area. In contrast, the SNNP grassland II (270 $\mu s\ cm^{-3}$) had lower EC, possibly because of less grazing, disturbance, and more open vegetation.

Grassland soils are generally neutral to slightly alkaline, but in this study, both ACA (6.4) and SNNP (6.3) grasslands had weakly acidic pH. Forest soils had more acidic pH (4.9 in ACA, 4.8 in SNNP) of this study (Fig. 4b) comply with the findings from Shrestha et al. (2020)

and Sigdel et al. (2015). Generally, decomposition of organic matter in forests contributes to this acidity. The optimal pH for soil nutrient availability and microbial activity is close to 7 (McCauley et al., 2009).

A soil's bulk density (BD) is an unpredictable attribute that changes depending on the soil's structural characteristics. In this study, the mean BD was found to be higher in ACA grassland I (1.04 g cm^{-3}) and SNNP grassland (1.09 g cm^{-3}) compared to the forests in ACA (0.86 g cm^{-3}) and SNNP (0.83 g cm^{-3}) (Fig. 4c). The higher BD in grassland than the forest, which were 1.29 and 1.23 g cm^{-3}, respectively were reported by Shrestha et al. (2020) observed in the grasslands of this study and most prominent in the SNNP grassland. The BD increases with availability of nutrients (Chaudhari et al. 2013), grazing intensity together (Hamza and Anderson, 2005) and vegetation. The average high BD (1.2 g cm^{-3}) reported by Muche et al. (2015), under grassland soil is in harmony with the BD value of SNNP grassland II with average value of 1.09 cm^{-3}. This could be due to lower litter deposition, which caused soil particles to be strongly packed together.

Soil textures in grasslands and forests can vary based on factors such as climate, parent material, plant types, and soil-forming processes (Tellen et al. 2018, Bhutia et al. 2021). Differences in precipitation, landscape position, and zone variations play significant roles in shaping soil texture (Meij et al. 2020, Sun et al. 2021, Sheshnitsan et al. 2024). Grassland soils feature a mix of clay and loam and offer better water retention, while forest soils develop finer textures due to organic matter accumulation. In this study, ACA grassland and forest soils had higher clay content (13.9% and 16.4%) than SNNP soils (11.7% and 9%), leading to higher water retention and poor drainage, which supports higher moisture content and nutrient levels. ACA soils were more clayey than those in the subtropical zone. However, ACA grassland (72.9%) and forest (65.5%) had lower sand content than SNNP grassland (78.6%) and forest (74.9%), indicating better drainage and lower nutrients in SNNP soils. The silt content was higher in ACA grassland (13.2%) and forest (18.2%) compared to SNNP grassland (12.4%) and forest (13.4%), showing moderate drainage and nutrient content in the ACA region (Fig. 5). Kumar et al. (2022) found significant differences in sand, silt, and clay percentages along the elevational gradient, with the lowest sand content between 3360 to 3540 m asl, supporting the lower sand proportion in the temperate zone of this study. Soil texture in grasslands and forests of ACA and SNNP was sandy loam (Table 1). A similar sandy loam texture was observed in temperate forests at varying altitudes in Uttarakhand, India (Rawat et al. 2021).

Soil organic matter (OM) is an important soil characteristic. The OM, such as animal manures and compost, can be added to the soil. As per the obtained result, grassland I of ACA had the higher percentage of OM (13.8%) than the other sites in different land use and zones (Fig. 6). A significant portion of grasslands are composed of herbaceous plants, which includes grasses and contribute OM to the soil. According to Mason and Zanner (2005) animal manures and roots are the principal sources of OM inputs for grassland soils, whereas plant litter makes up a very small portion, thus supporting for higher OM in ACA grassland I (Figure 6). Antony et al. (2022), stated that topsoil and subsoil of the forests were substantially higher in the mineral-free particulate matter proportion, and supported for higher OM percentage in both forests (11.9% in ACA, 10.3% in SNNP). As a consequence of the decomposition of leaf litter, forests obtain a higher intake of OM, which significantly assists in the accumulation of organic matter than those under grassland. The intensity and frequency of grazing have a substantial impact on OM build-up. Overgrazing inhibits OM formation, which could explain why the SNNP grassland (7.0%) has low OM availability. Moderate grazing, on the other hand, promotes root growth and increases organic input, contributing in more OM in ACA grassland I.

Soil organic carbon (SOC) is an essential component of terrestrial ecosystems, contributing significantly to carbon sequestration and general soil health. The amount of SOC was found higher in grassland I (123.3 t ha^{-1}) and forest I (84.6 t ha^{-1}) of ACA. Similar result was obtained in a study conducted by Gupta et al. (2013), where SOC pool was estimated in the grasslands occurring between the wide altitudinal range, found that 142.14 t ha^{-1} was observed in the altitudinal range of 2501and 4200m asl and 97.80 t ha^{-1} between 150 and 2000 m asl, and concluded that temperate climate favours organic carbon accumulation in the soil (Fig. 7). Dondini et al. (2023) stated that the highest SOC stocks were discovered in temperate areas with slow rates of decomposition and high productivity of grasslands. The soil carbon increases from tropical to boreal climates, with temperate forests retaining up to 100 Mg C ha^{-1} or more (Lal 2013). Our study showed similar results, with SNNP forest in the subtropical zone storing more SOC (71.72 t ha^{-1}) than grassland (55.5 t ha^{-1}). Ghimire et al. (2018) found higher SOC (110 t ha^{-1}) in forests, noting that SOC varies with land use. Moderate temperatures in temperate zones reduced microbial activity, but vegetation adds more organic matter to the soil. A study by Cai et al. (2016) showed higher MOC/TSOC ratios in temperate forest and grassland soils compared to subtropical areas, emphasizing that soil texture, type, climate, and land use are key factors for SOC storage.

5. CONCLUSION

The study found significant variation in soil properties between grassland and forest across land use and climatic zones. In ACA temperate grassland, most soil properties were higher than in the forest, except for soil moisture and clay/silt percentages. In SNNP subtropical climate, grasslands had higher soil temperature, moisture, pH, bulk density, and sand content. ACA grassland stored more SOC, while SNNP forest had higher SOC than the grassland. Grasslands showed lower SOC storage due to frequent disturbances. In ACA grassland, SOC positively correlated with bulk density (BD), while in the forest, it had a negative correlation. In SNNP grassland, SOC, organic matter (OM), and moisture content (MC) negatively correlated with BD, while in the forest, MC, OM, and SOC were positively correlated. SOC sequestration was higher in the temperate zone. The study emphasized the importance of grassland and forest soils in SOC storage and the need for effective soil management, including grazing control, soil quality assessment, ecosystem research, protective laws, and public awareness.

ACKNOWLEDGEMENT

This research was supported by the Nepal Academy of Science and Technology (NAST) through equipment, chemicals, and guidance. We thank the Department of National Park and Wildlife Conservation (DNPWC), Government of Nepal and Annapurna Conservation Area Project (ACAP) for sampling permission, and the local people for their valuable support.

REFERENCES

Adhikari, K. and A. E. Hartemink, 2017. Soil organic carbon increases under intensive agriculture in the Central Sands, Wisconsin, USA. Geoderma Regional, 10:115-125. DOI: 10.1016/j.geodrs.2017.07.003

Ali, A., M. I. Ashra., S. Gulzar, M. Akmal and B. Ahmad, 2020. Estimation of soil carbon pools in the forests of Khyber Pakhtunkhwa Province, Pakistan. Journal of Forestry Research, 31:2313-2321. DOI: 10.1007/s11676-019-01059-9

Alidoust, E., Afyuni, M., Hajabbasi, M. A., and Mosaddeghi, M. R, 2018. Soil carbon sequestration potential as affected by soil physical and climatic factors under different land uses in a semiarid region. Catena, 171:62-71. DOI: 10.1016/j.catena.2018.07.005

Antony, D., C. D. Collins, J. M. Clark and T. Sizmur, 2022. Soil organic matter storage in temperate lowland arable, grassland and woodland topsoil and subsoil. Soil Use and Management, 38(4):1532-1546. DOI: 10.1111/sum.12801

Beniston, J. W., S. T. DuPont, J. D. Glover, R. Lal and J. A. Dungait, 2014. Soil organic carbon dynamics 75 years after land-use change in perennial grassland and annual wheat agricultural systems. Biogeochemistry, 120:37-49. DOI: 10.1007/s10533-014-9980-3

Bhattacharyya, T., D. K. Pal, P. Chandran, S. K. Ray, C. Mandal and B. Telpande, 2008. Soil carbon storage capacity as a tool to prioritize areas for carbon sequestration. Current science, 482-494.

Bhutia, P. L., B. Gupta, R. P. Yadav, A. K. Gupta, K. G. Bhutia and P. Rai, 2021. Soil physico-chemical and biological properties as affected by vegetation systems and elevation in western Himalayas. Range Management and Agroforestry, 42(1):86-94.

Binkley, D., F. Singer, M. Kaye and R. Rochelle, 2003. Influence of elk grazing on soil properties in Rocky Mountain National Park. Forest Ecology and Management, 185(3):239-247. DOI: 10.1016/S0378-1127(03)00162-2

Blake, G. R. and K. H. Hartege, 1986. Bulk density. In: Physical and mineralogical methods of agronomy, methods of soil Analysis (2nd ed., pp. 425-442). Maidson, ASA; SSSA. Monographs. DOI: 10.2136/sssabookser5.1.2ed.c13

Bonan, G. B., 2008. Forests and climate change: forcings, feedbacks, and the climate benefits of forests. Science, 320(5882):1444-1449. DOI: 10.1126/science.1155121 PMID: 18556546

Cai, A., W. Feng, W. Zhang and M. Xu, 2016. Climate, soil texture, and soil types affect the contributions of fine-fraction-stabilized carbon to total soil organic carbon in different land uses across China. Journal of Environmental Management, 172:2-9. DOI: 10.1016/j.jenvman.2016.02.009 PMID: 26905446

Chaneton, E. J. and R. S. Lavado, 1996. Soil nutrients and salinity after long-term grazing exclusion in a flooding Pampa grassland. Journal of Range Management, 49(2):182-187. DOI: 10.2307/4002692

Chaudhari, P. R., D. V. Ahire, V. D. Ahire, M. Chkravarty and S. Maity, 2013. Soil bulk density as related to soil texture, organic matter content and available total nutrients of Coimbatore soil. International Journal of Scientific and Research Publications, 3(2):1-8.

Dar, Z. A., Q. Humaira, M. S. Ahmad, B. Bilal and A. Amin, 2018. Assessment of physico-chemical parameters of forest soil of Hirpora Wildlife Sanctuary,Kashmir. International Journal of Advance Research in Science and Engineering, 7(4): 46-56.

Dhital D, S. Prajapati, S. R. Maharjan and H. Koizumi, 2019. Soil carbon dioxide emission: soil respiration measurement in temperate grassland, Nepal. Journal of Environmental Protection, 10(2):289-314. DOI: 10.4236/jep.2019.102017

Dhital D, P. Manandhar, B. Gosain and J. Sijapati, 2022a. Soil respiration variations in temperate Rhododendron (*Rhododendron arboreum*) forest of Annapurna Conservation Area (ACA) in Nepal. International Journal of Forestry Research, 1-14. DOI: 10.1155/2022/1677084

Dhital D, R. Manandhar, P. Manandhar and S. R. Maharjan, 2022b. Soil CO2 efflux dynamics and its relationship with the environmental variables in a sub-tropical mixed forest. Open Journal of Forestry, 12(3):312-336. DOI: 10.4236/ojf.2022.123017

Dondini, M., M. Martin, C. De Camillis, A. Uwizeye, J. F. Soussana, T. Robinson and H. Steinfeld, 2023. Global assessment of soil carbon in grasslands: From current stock estimates to sequestration potential, vol. 187. Rome, Food and Agriculture Organization of the United Nations FAO.

Douglas W. Pribyl, 2010. A critical review of the conventional SOC to SOM conversion factor, Geoderma, 156(3-4):75-83. DOI: 10.1016/j.geoderma.2010.02.003

Feeney C. J., L. Bentley, D. D. Rosa, P. Panagos, B. A. Emmett, A. Thomas, D. A. Robinson, 2024. Benchmarking soil organic carbon (SOC) concentration provides more robust soil health assessment than the SOC/clay ratio at European scale. Science of The Total Environment, 951:175642. DOI: 10.1016/j.scitotenv.2024.175642 PMID: 39163941

Food and Agriculture Organization (FAO) of the United Nations, 2020. Global forest resources assessment (pp. 1-186), Rome.

Ghosh, C., M. Mukherjee and K. Biswas, 2020. Physico-chemical Properties of Soil of Jaldapara National Park in West Bengal, India. International Journal of Advanced Research in Biological Sciences, 7(6):141-150.

Ghosh, P. K., and S. K. Mahanta, 2014. Carbon sequestration in grassland systems. Range Management and Agroforestry, 35(2):173-181.

Ghimire, P., B. Bhatta, B. Pokhrel, G. Kafle and P. Paudel, 2018. Soil organic carbon stocks under different land uses in Chure region of Makawanpur district, Nepal. SAARC Journal of Agriculture, 16(2):13-23. DOI: 10.3329/sja.v16i2.40255

Gupta, M. K. and S. D. Sharma, 2013. Sequestered organic carbon status in the soils under grassland in Uttarakhand State, India. Applied Ecology and Environmental Sciences, 1(1):7-9. DOI: 10.12691/aees-1-1-2

Hamza, M. A. and W. K. Anderson, 2005. Soil compaction in cropping systems: A review of the nature, causes and possible solutions. Soil and Tillage Research, 82(2):21-145. DOI: 10.1016/j.still.2004.08.009

Harden, J. W., G. Hugelius, A. Ahlström, J. C. Blankinship, B. Bond-Lamberty, C. R. Lawrence and L. E. Nave, 2018. Networking our science to characterize the state, vulnerabilities, and management opportunities of soil organic matter. Global Change Biology, 24(2):e705-e718. DOI: 10.1111/gcb.13896 PMID: 28981192

Iranmanesh M. and H. Sadeghi, 2019. Effects of soil texture and nitrogen on ability of carbon sequestration in different organs of two *Tamarix* species as a good choice for carbon stock in dry lands. Ecological Engineering, 139:105577. DOI: 10.1016/j.ecoleng.2019.08.007

Islam, M., S. H. Salim, M. H. Kawsar and M. Rahman, 2016. The effect of soil moisture content and forest canopy openness on the regeneration of Dipterocarpus turbinatus CF Gaertn (Dipterocarpaceae) in a protected forest area of Bangladesh. Tropical Ecology, 57(3):455-464.

Kopittke, P. M., A. A. Berhe, Y. Carrillo, T. R. Cavagnaro, D. Chen, Q. L. Chen, et al., 2022. Ensuring planetary survival: the centrality of organic carbon in balancing the multifunctional nature of soils. Critical Reviews in Environmental Science and Technology, 52(23): 4308-4324. DOI: 10.1080/10643389.2021.2024484

Kumar, D., D. R. Bhardwaj, P. Sharma, Bharti, N. Sankhyan, N. Al-Ansari and N. T. Linh, 2022. Population dynamics of juniperus macropoda bossier forest ecosystem in relation to soil physicochemical characteristics in the cold desert of north-western Himalaya. Forests, 13(10):624. DOI: 10.3390/f13101624

Lal, R., 2005. Forest soils and carbon sequestration. Forest ecology and management, 220(1-3):242-258. DOI: 10.1016/j.foreco.2005.08.015

Lal, R. 2013. Soil carbon management and climate change. Carbon Management, 4(4):439-462. DOI: 10.4155/cmt.13.31

Lozano-Parra, J., M. Pulido, C. Lozano-Fondón and S. Schnabel, 2018. How do soil moisture and vegetation covers influence soil temperature in drylands of mediterranean regions? Water, 10:12-747. DOI: 10.3390/w10121747

Luis, M. R., M. D. Hidalgo Galvez, J. Cambrolle, M. T. Dominguez and I. M. Perez-Ramos, 2021. How will forecasted warming and drought affect soil respiration in savannah ecosystems? The role of tree canopy and grazing legacy. Agricultural and Forest Meteorology, 304:305-108425. DOI: 10.1016/j.agrformet.2021.108425

Mason, J. A. and C. W. Zanner, 2005. Grassland soils. Encyclopedia of Soils in the Environment, 138-145. DOI: 10.1016/B0-12-348530-4/00028-X

Mayer, M., C. F. Prescott, W. E. Abaker, L. Augusto, L. Cécillon, G. W. Ferreira and L. Vesterdal, 2020. Tamm Review: Influence of forest management activities on soil organic carbon stocks: A knowledge synthesis. Forest Ecology and Management, 466:118127. DOI: 10.1016/j.foreco.2020.118127

McCauley, A., C. Jones and J. Jacobsen, 2009. Soil pH and organic matter. Nutrient management module, 8(2):1-12.

Melillo, J. M., X. Lu, D. W. Kicklighter, J. M. Reilly, Y. Cai and A. P. Sokolov, 2016. Protected areas' role in climate-change mitigation. Ambio, 45:133-145. DOI: 10.1007/s13280-015-0693-1 PMID: 26474765 PMCID: PMC4752559

Meena, V. S., T. Mondal, B. M. Pandey, A. Mukherjee, R. P. Yadav, M. Choudhary and A. Pattanayak, 2018. Land use changes: Strategies to improve soil carbon and nitrogen storage pattern in the mid-Himalaya ecosystem, India. Geoderma, 321:69-78. DOI: 10.1016/j.geoderma.2018.02.002

Morecroft, M. D., M. E. Taylor and H. R. Oliver, 1998. Air and soil microclimates of deciduous woodland compared to an open site. Agricultural and Forest Meteorology, 90(1-2):141-156. DOI: 10.1016/S0168-1923(97)00070-1

Muche, M., A. Kokeb and E. Molla, 2015. Assessing the physicochemical properties of soil under different land use types. Journal of Environmental and Analytical Toxicology, 5(5):1-5.

National Research Council, 1993. Soil and water quality: An agenda for agriculture. National Academies Press.

Oli, B. N. and K. Shrestha, 2009. Carbon status in forests of Nepal: An overview. Journal of Forest and Livelihood, 8(1):62-66.

Onwuka, B. and B. Mang, 2018. Effects of soil temperature on some soil properties and plant growth. Journal of Agricultural Science, 8(1):34-37. DOI: 10.15406/apar.2018.08.00288

Pan, Y., R. A. Birdsey, J. Fang, R. Houghton, P. E. Kauppi, W. A. Kurz and D. Hayes, 2011. A large and persistent carbon sink in the world's forests. Science, 333(6045):988-993. DOI: 10.1126/science.1201609 PMID: 21764754

Panchal, P., C. Preece, J. Peñuelas and J. Giri, 2022. Soil carbon sequestration by root exudates. Trends in Plant Science, 27(8):749-757. DOI: 10.1016/j.tplants.2022.04.009 PMID: 35606255

Paustian, K., H. P. Collins and E. A. Paul, 2019. Management controls on soil carbon. Soil organic matter in temperate agroecosystems, pp. 15-49. CRC Press DOI: 10.1201/9780367811693-2

Pradhan, S. B., 1996. Soil and plant analysis manual. Nepal Agricultural Research Council (NARC).

Rawat, V., A. S. Bagri, H. Singh, P. Tiwari and J. Krishan, 2021. Altitudinal variation in soil physico-chemical properties of a Western Himalayan Forest, Uttarakhand, India. Journal of Mountain Research, 16(3):111-119. DOI: 10.51220/jmr.v16i3.12

Shapkota, J. and G. Kafle, 2021. Variation in Soil Organic Carbon under Different Forest Types in Shivapuri Nagarjun National Park, Nepal. Scientifica, 2021. DOI: 10.1155/2021/1382687 PMID: 34777893 PMCID: PMC8580687

Sheikh, M. A., M. Kumar and R. W. Bussmann, 2009. Altitudinal variation in soil organic carbon stock in coniferous subtropical and broadleaf temperate forests in Garhwal Himalaya. Carbon Balance and Management, 4:1-6. DOI: 10.1186/1750-0680-4-6 PMID: 19706175 PMCID: PMC2745406

Sheshnitsan, S., G. Odnoralov, E. Tikhonova, N. Gorbunova, T. Sheshnitsan, O. C. Murariu and G. Caruso, 2024. Influence of Soil Texture on Carbon Stocks in Deciduous and Coniferous Forest Biomass in the Forest-Steppe Zone of Oka-Don Plain. Soil Systems, 8:4-118. DOI: 10.3390/soilsystems8040118

Shi, W. Y., R. Tateno, J. G. Zhang, Y. L. Wang, N. Yamanaka and S. Du, 2011. Response of soil respiration to precipitation during the dry season in two typical forest stands in the forest-grassland transition zone of the Loess Plateau. Agricultural and Forest Meteorology, 151(7):854-863. DOI: 10.1016/j.agrformet.2011.02.003

Shrestha, K, 2016. Variation in soil organic carbon within highland grasslands of Langtang National Park, Nepal. International Journal of Environment, 5(3):57-65. DOI: 10.3126/ije.v5i3.15704

Shrestha, S. and G. Kafle, 2020. Variation of selected physicochemical and hydrological properties of soils in different tropical land use systems of Nepal. Applied and Environmental Soil Science, 2020(1):8877643. DOI: 10.1155/2020/8877643

Sigdel, S. R., D. Rupakheti, U. Baral, L. Tripathee, R. Aryal, S. Dhital and P. Sharma, 2015. Physico-chemical characteristics of soil along an altitudinal gradient at southern aspect of Shivapuri Nagarjun National Park, Central Nepal. International Research Journal of Earth Sciences, 3(2):1-6.

Smith, J. L., and J. W. Doran, 1997. Measurement and Use of pH and Electrical Conductivity for Soil Quality Analysis. In Methods for Assessing Soil Quality, pp. 169-185. John Wiley & Sons, Ltd. DOI: 10.2136/sssaspecpub49.c10

Subashree, K., J. A. Dar and S. Sundarapandian, 2019. Variation in soil organic carbon stock with forest type in tropical forests of Kanyakumari Wildlife Sanctuary, Western Ghats, India. Environmental Monitoring and Assessment, 191:1-16. DOI: 10.1007/s10661-019-7881-6 PMID: 31664599

Sun, S., G. Zhang, T. He, S. Song and X. Chu, 2021. Effects of landscape positions and landscape types on soil properties and chlorophyll content of citrus in a sloping orchard in the three gorges reservoir area, China. Sustainability, 13:8-4288. DOI: 10.3390/su13084288

Tang M., W. Li, X. Gao, P. Wu, H. Li, Q. Ling and C. Zhang, 2022. Land use affects the response of soil moisture and soil temperature to environmental factors in the loess hilly region of China. PeerJ 10:e13736. DOI: 10.7717/peerj.13736 PMID: 35855431 PMCID: PMC9288829

Tellen, V. A. and B. P. K. Yerima, 2018. Effects of land use change on soil physicochemical properties in selected areas in the North West region of Cameroon. Environmental Systems Research, 7:1-29. DOI: 10.1186/s40068-018-0106-0 van der Meij, W. M., A. J. A. M. Temme, J. Wallinga and M. Sommer, 2020. Modeling soil and landscape evolution - the effect of rainfall and land-use change on soil and landscape patterns, Soil, 6:337-358. DOI: 10.5194/soil-6-337-2020

Walkley, A. and I. A. Black, 1934. An Examination of the Degtjareff method for determining organic carbon in soils: Effect of variations in digestion conditions and of inorganic soil constituents. Soil Science, 63:251-263. DOI: 10.1097/00010694-194704000-00001

Wiesmeier, M., L. Urbanski, E. Hobley, B. Lang, M. von Lützow, E. Marin-Spiotta and I. Kögel-Knabner, 2019. Soil organic carbon storage as a key function of soils-A review of drivers and indicators at various scales. Geoderma, 333:149-162. DOI: 10.1016/j.geoderma.2018.07.026

Zhang, X., J. F. Adamowski, R. C. Deo, X. Xu, G. Zhu and J. Cao, 2018. Effects of Afforestation on Soil Bulk Density and pH in the Loess Plateau, China. Water, 10(12):1710. DOI: 10.3390/w10121710

Zhong, X. L., J. T. Li, X. J. Li, Y. C. Ye, S. S. Liu, P. D. Hallett and M. Naveed, 2017. Physical protection by soil aggregates stabilizes soil organic carbon under simulated N deposition in a subtropical forest of China. Geoderma, 285:323-332. DOI: 10.1016/j.geoderma.2016.09.026

Zhou, Q., Z. Sun, X. Liu, X. Wei, Z. Peng, C. Yue and Y. Luo, 2019. Temporal soil moisture variations in different vegetation cover types in karst areas of southwest China: A plot scale case study. Water, 11(7):1423. DOI: 10.3390/w11071423

A Comparative Analysis of the Photon Beam Percentage Depth Dose in an Elekta Linear Accelerator at a Comprehensive Cancer Center

Rajan Prajapati[1*], Junaid Abdul Salam[1], Abish Adhikari[1], Gerim Prasai[1], Subhas Pandit[2], Simit Sapkota[2], Anjani Kumar Jha[2]

[1] Department of Radiation Oncology, Kathmandu Cancer Center, Tathali, Bhaktapur, Nepal
[2] Department of Clinical Oncology, Kathmandu Cancer Center, Tathali, Bhaktapur, Nepal

***CORRESPONDING AUTHOR:**

Rajan Prajapati
Email: rajanprajapati1617@gmail.com

ISSN : 2382-5359(Online), 1994-1412(Print)

DOI:
https://doi.org/10.3126/njst.v22i2.100112

Date of Submission: 13 Apr, 2026

Date of Acceptance: 29 May, 2026

ABSTRACT

This study aims to verify the photon beam energy characteristics of an Elekta Synergy Platform LINAC at Kathmandu Cancer Center, Tathali Nala road by comparing measured PDD data with established British Journal of Radiology (BJR) Supplement 25 and other published literature. PDD measurements were performed for photon energies of 4 MV, 6 MV, and 15 MV using seven different field sizes. All measurements were taken under consistent environmental and setup conditions, including identical pressure, temperature, incremental depth steps, geometry, chamber voltage, and polarity.

For the reference 10 × 10 cm² field size, the measured maximum depth doses (d_{max}) were found to be 1.18 cm, 1.58 cm, and 2.68 cm for 4 MV, 6 MV, and 15 MV photon beams, respectively. The corresponding PDD values at 10 cm depth (d_{10}) were 62.2% for 4 MV, 66.1% for 6 MV, and 74.9% for 15 MV photon energies.

The measured values for 4, 6, and 15 MV photon beams fell within acceptable tolerance limits. The resulting PDD curves demonstrated strong agreement with the reference data in BJR-25 and other published studies, thereby confirming the consistency of beam quality of the Elekta Synergy Platform LINAC.

Keywords: Linear accelerator, Photon beam, Radiotherapy, percentage depth dose (PDD).

1. INTRODUCTION

A linear accelerator (LINAC) is an advanced device used in radiation therapy for cancer treatment, capable of producing high-energy X-ray (photon) or electron beams that precisely target tumors while reducing radiation exposure to surrounding healthy tissues (Corradini et al., 2019). Photon beams are the most used modality in radiotherapy, and a thorough understanding of their dosimetric properties and is essential for accurate and effective treatment planning.

The quality of a photon beam is chiefly determined by its penetrating ability, which is related to its mean photon energy. This characteristic is effectively assessed by the Percentage Depth Dose (PDD) in water (Kato et al., 2004). PDD is therefore a fundamental parameter in radiation dose calculations, ensuring that the prescribed dose is accurately delivered to the tumor (Memon et al., 2015). As direct measurement of dose distribution within a patient is not feasible, PDDs are measured in a homogeneous water phantom that closely mimics human tissue (Ali et al., 2023). These measurements are subsequently incorporated into the treatment planning system (TPS) to determine the absorbed dose for clinical radiotherapy applications (Khan & Gibbons, 2014; Xhafa et al., 2014).

The absorbed dose distribution within the patient depends on several influencing factors, including field size, beam energy, source-to-surface distance (SSD), depth, angle of beam incidence, and beam-modifying devices (Bilge et al., 2010). High-precision dose delivery is vital, as even slight inaccuracies can significantly impact treatment outcomes. Research has shown that a 5% deviation in absorbed dose may result in a 10–20% change in tumor control probability and a 20–30% increase in normal tissue complications (Brahme, 1984). Similarly, dose deviations of 10–15% variation can potentially reduce the probability of cure while increasing irreversible damage by two to three times. Therefore, radiotherapy requires strict adherence to dose accuracy within ±5% of the prescribed dose to safeguard surrounding organs and critical structures (Omer, 2015).

Accurate acquisition of beam data is essential to ensure reliable treatment delivery, as any discrepancies may affect every patient treated with the system (Knutson et al., 2018). In this context, PDD measurements play a crucial role in providing precise information on dose deposition at various depths within tissues, thereby supporting optimal treatment planning and clinical outcomes (Mihailidis, 2011).

Therefore, this study aims to measure and validate PDDs across different field sizes and depths, comparing the results with established reference data to ensure the quality assurance and performance reliability of the Elekta Synergy Platform LINAC at Kathmandu Cancer Center, Nepal.

2. MATERIALS AND METHODS

2.1 Linear Accelerator and Photon Beam Specifications

This study was conducted using an Elekta Synergy Platform linear accelerator, commissioned in 2016, capable of delivering dual-energy photon beams of 4 MV, 6 MV, and 15 MV, as well as multiple electron energies ranging from 4 MeV to 15 MeV. For the purposes of this study, PDD measurements were performed specifically for the photon beams of 4 MV, 6 MV, and 15 MV.

2.2 Measurement Setup

2.2.1 Phantom and Chamber Configuration

PDD measurements were carried out using a 3D water phantom (The Ecophan Water Phantom, IBA). A CC13 ionization chamber (SN 14089) was used as the field chamber and positioned along the central axis inside the water phantom. A second CC13 ionization chamber (SN 14077) served as the reference chamber and was placed just above the water surface outside the primary beam to continuously correct for variations in beam output. All measurements were managed using IBA myQA Accept software version 2016-001 (8.0.1.0) in accordance with the IAEA TRS-398 dosimetry protocol (2004).

2.2.2 Chamber Positioning and Effective Point of Measurement

The water phantom was leveled using a spirit level, and the source-to-surface distance (SSD) was maintained at 100 cm. The field chamber was initially aligned with the water surface to define zero depth. To account for the Effective Point of Measurement (EPOM), the field chamber was shifted downstream by half of its internal radius (0.5r) of the CC13 ionization chamber SN 14089, as recommended by the IAEA (Musolino, 2001). After adjustment, the zero depth was re-established, ensuring accurate measurement along the central axis.

2.3 Percentage Depth Dose (PDD)

The Percentage Depth Dose (PDD) is defined as the ratio of the absorbed dose at a specific depth along the central axis of the beam to the dose at a reference depth, expressed as a percentage. Mathematically, it is represented as:

$PDD = D_P / D_Q * 100\%$

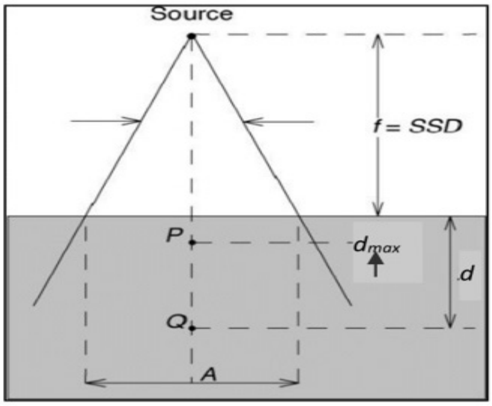

Fig 1: *The Setup for PDD measurement (IAEA TRS 398 2004).*

where represents the absorbed dose at depth Q, and represents the absorbed dose at the reference depth, P. Measurement of the PDD along the central axis is a key component of LINAC commissioning, as it provides essential information for accurate dose calculations in treatment planning (Khan & Gibbons, 2014).

2.4 Measurement Procedure

During the experiment, the field chamber was mounted inside the water phantom along the central beam axis, while the reference chamber monitored output stability. Continuous scanning was performed from a depth of 35 cm up to the water surface (0 mm) to minimize disturbances caused by water movement. The scanning and data acquisition processes were fully automated and controlled by the myQA Accept software (Mani et al., 2018).

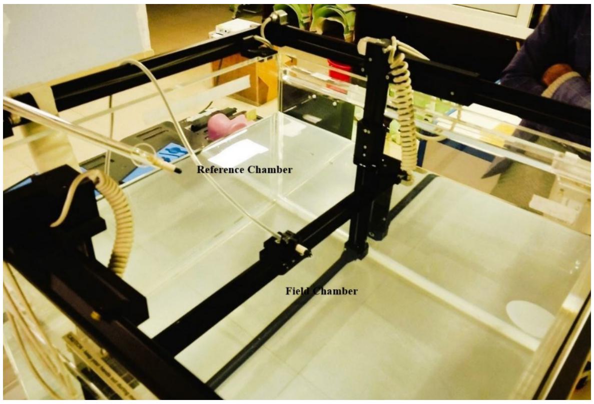

Fig 2: *Phantom setup for PDDs measurements*

2.5 Field Sizes and Beam Configuration

PDDs were measured for seven square field sizes: 5 × 5, 7 × 7, 10 × 10, 15 × 15, 20 × 20, 30 × 30, and 40 × 40 cm². The Field sizes were defined using the collimator jaws rather than multileaf collimators (MLCs) to avoid dosimetric uncertainties caused by leaf transmission or interleaf gaps (Rahman et al., 2021).

2.6 Data Processing

The measured PDD curves were smoothed using the myQA Accept software. Further analysis, graph plotting, and final presentation of the PDD curves were performed using Microsoft Excel (Microsoft Office Professional 2016).

3. RESULTS

3.1 PDD Curves for Different Field Sizes

The percentage depth dose (PDD) curves for photon energies of 4 MV, 6 MV, and 15 MV across various field sizes normalized d_{max} are presented in Figures 3, 4, and 5, respectively. For all beam energies, the PDD initially increases rapidly in the buildup region, reaches a maximum at d_{max}, and then gradually decreases with depth due to photon attenuation and scattering. The magnitude of the PDD and the depth of the maximum dose are influenced by both photon energy and field size. Higher photon energies exhibit greater penetration, resulting in higher PDD values at the same depth compared to lower-energy beams.

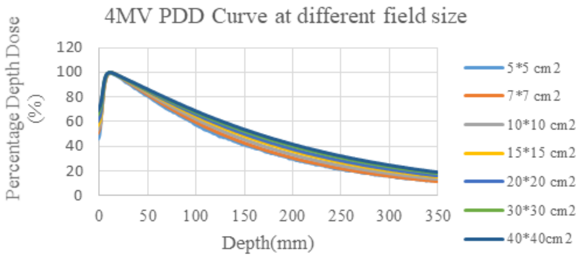

Fig 3: *4MV PDDs Curve at different field sizes*

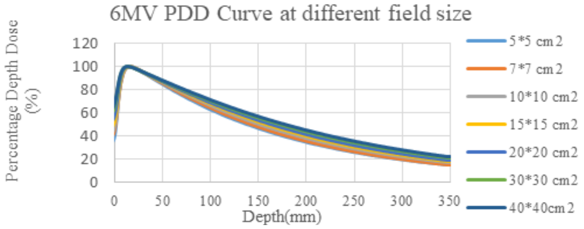

Fig 4: *6MV PDDs Curve at different field sizes.*

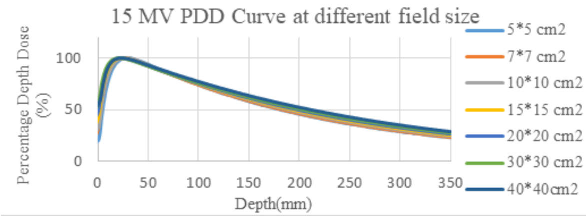

Fig 5: *15MV PDDs Curve at different field sizes*

3.2 Surface Dose, Depth of Maximum Dose, and Depth of 50% Dose

The measured surface dose (d_s), depth of maximum dose (d_{max}), depth at 10 cm (D_{10}), and depth of 50% dose (d_{50}) for different field sizes and photon energies are summarized in Table 1. For the standard 10 × 10 cm² field, the surface doses were 57.2%, 52.6%, and 32.8% for 4 MV, 6 MV, and 15 MV beams, respectively. The corresponding depths of maximum dose were 1.18 cm, 1.58 cm, and 2.68 cm, indicating that the point of peak dose shifts deeper as photon energy increases.

The average dose increase per centimeter up to d_{max} was 42.37% for 4 MV, 31.65% for 6 MV, and 18.66% for 15 MV beams. The percentage increase in dose per centimeter in the build-up region decreased with increasing photon energy. The 4 MV beam exhibited the steepest dose build-up (42.37% per cm), followed by 6 MV (31.65% per cm) and 15 MV (18.66% per cm). This trend reflects the deeper d_{max} and improved skin-sparing characteristics of higher-energy photon beams (Podgorsak, 2005). Conversely, the dose fall-off from d_{max} to d_{50} decreased with increasing photon energy, with measured average reductions of 4.05%, 3.72%, and 3.081% per centimeter for 4 MV, 6 MV, and 15 MV beams, respectively. Smaller field sizes exhibited a slightly higher dose fall-off, likely due to reduced contribution from overlapping scatter regions.

3.3 Standard Field Size PDD Profiles

Figure 6 presents the PDD curves for a 10 × 10 cm² reference field at Photon energies of 4 MV, 6 MV, and 15 MV. The curves demonstrate the rapid buildup of dose in the first few millimeters, followed by a gradual decrease after reaching d_{max}. As expected, the depth of maximum dose increases with photon energy, while the surface dose decreases. These trends are consistent with the physical behavior of photon beams, where higher-energy photon beams penetrate deeper before depositing the maximum dose.

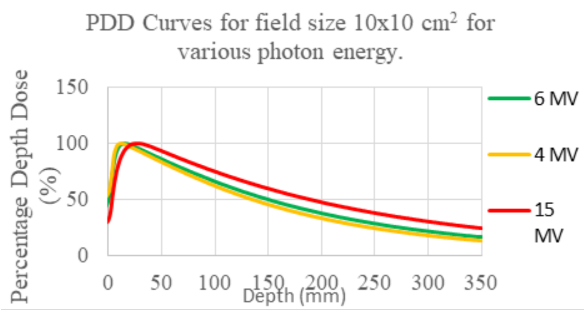

Fig 6: *PDD curves for a 10 × 10 cm² field size at different photon beam energies*

3.4 Observations across field sizes

As the field size increases from 5 × 5 cm² to 40 × 40 cm², the surface dose and D_{10} values increase for all photon energies, reflecting increased scatter contributions from larger fields. The depth of maximum dose, however, shows a slight decrease with larger fields at lower photon energies, while remaining relatively stable at higher photon energies. These results align with expected dosimetric behavior and provide essential reference data for treatment planning and LINAC commissioning (Khan & Gibbons, 2014; Podgorsak, 2005).

Table 1: Surface dose (ds), depth of maximum dose (d max), and depth of 50% dose (d_{50}) for different field sizes of 4MV, 6 MV, and 15 MV photon beams.

Field Size (cm^2)	Surface Dose d_s (%)			Depth of max. dose dmax(cm)			PDD at 10 cm			Depth at which 50% dose(d_{50}) in cm.		
	4MV	6 MV	15 MV	4MV	6MV	15MV	4MV	6MV	15MV	4 MV	6 MV	15MV
5*5	51.3	45.6	20.9	1.18	1.57	3.18	57.4	62.7	74.2	12.07	13.77	18.22
7*7	55.6	50.5	31.9	1.18	1.58	2.68	60.0	64.5	74.0	12.76	14.33	18.32
10*10	57.2	52.6	31.9	1.18	1.58	2.68	62.2	66.1	74.9	13.51	15.02	18.91
15*15	60.7	57.7	42.7	1.18	1.38	2.38	64.5	67.9	75.1	14.42	15.88	19.40
20*20	64.1	62.4	48.9	1.18	1.38	2.28	66.0	68.9	75.4	15.05	16.43	19.80
30*30	69.6	69.3	56.2	1.18	1.38	2.08	67.6	70.4	76.0	15.89	17.29	20.40
40*40	72.4	71.6	55.0	1.07	1.37	2.38	68.7	71.2	77.2	16.44	17.84	21.07

4. DISCUSSION

The observed percentage depth-dose (PDD) behavior in this study is consistent with the physical principles of photon interactions in tissue-equivalent media. Beyond the depth of maximum dose (d_{max}), PDD decreases with increasing depth due to photon attenuation, scattering, and the inverse square law. Conversely, higher-energy photon beams exhibit greater penetration, resulting in higher PDD values at a given depth compared to lower-energy beams (Khan & Gibbons, 2014). In the buildup region, PDD increases with depth due to the generation of secondary electrons, which deposit their energy over a short distance downstream of their origin before being fully stopped.

The dependence of PDD on field size is influenced by photon energy. For a lower-energy Photon beam, increasing the field size enhances the contribution of scattered radiation, resulting in higher PDD values. However, as photon energy increases, the probability of scattering decreases, and photons tend to scatter more in the forward direction. Consequently, the effect of field size on PDD diminishes for higher-energy beams (Rahman et al., 2021; Podgorsak, 2005; Roy et al., 2021).

4.1 Comparison with BJR-25 and Published Data

The measured PDD values for photon beam of 4 MV, 6 MV, and 15 MV with a reference field size of 10 × 10 cm^2 were plotted, normalized the measured dose value to 100% at dmax and compared to the reference data from BJR Supplement 25. Figures 7 to 9 illustrate the PDD curves for the three photon energies, demonstrating excellent agreement between the measured data and BJR-25 reference values (Bewley, 1983). Table 2 further confirms the consistency of key dosimetric parameters, including the dose at 10 cm depth (D_{10}), depth of 80% dose (D_{80}), depth of maximum dose (d_{max}), and the dose fall-off from d_{max} to D_{50}. The measured values align closely with BJR-25 and other published datasets, validating the commissioning data for the Elekta Synergy LINAC.

For 4 MV beam, the measured d_{max} was 1.18 cm, d_{10} was 62.2%, and d_{80} was 5.75 cm, closely matching BJR-25 values of 1.0 cm, 63.0%, and 5.9 cm, respectively. Similarly, the 6 MV beam measurements yielded a d_{max} of 1.58 cm, d_{10} of 66.1%, and d_{80} of 6.42 cm, closely matching BJR-25 values of 1.5 cm, 67.5.0%, and 6.7 cm, respectively. Also, for the 15 MV beam, the measured d_{max} was at 2.68 cm, d_{10} at 74.9%, and d_{80} at 8.52 cm, closely matching BJR- 25 values of 2.9 cm, d_{10} was 77%, and d_{80} was 9.1 cm, respectively. The Commissioning data show small deviations from BJR-25 values for d_{10}, d_{80}, d_{max} and dose fall off, which are expected due to the machine-specific nature of measured data. BJR-25 represents average reference beam data, whereas commissioning measurements reflects the unique beam characteristics of the Linac, including target design, flattering filter geometry, and head scatter (Khan & Gibbons, 2014; Podgorsak, 2005). The observed difference, typically within 1-3% for d_{10} and within a few millimeters for depth parameters, is consistent with published studies and lies within acceptable dosimetric tolerances for clinical use (IAEA TRS 398 2004; Buzdar et al., 2009; Mia et al., 2019). The dose fall-off per centimeter from d_{max} to d_{50} also matches reference values, further confirming the accuracy of the measured PDD curves.

Table 2: Comparison of measured data with BJR-25 and other published studies for a reference field size of 10 × 10 cm².

Energy	Observation	d_{10} (%)	d_{80} (cm)	d_{max} (cm)	Fall of dose d_{max} to d_{50}(%/cm)
4MV	BJR 25	63.0	5.9	1.0	3.906
	Commissioning Data	62.2	5.75	1.18	4.055
	Buzdar et al. 2009	-	-	1.0	3.88
	Mia et al. 2019	-	-	-	-
6MV	BJR 25	67.5	6.7	1.5	3.546
	Commissioning Data	66.1	6.42	1.58	3.720
	Buzdar et al. 2009	-	-	1.5	3.55
	Mia et al. 2019	66.8	-	1.58	3.72
15MV	BJR 25	77.0	9.1	2.9	2.934
	Commissioning Data	74.9	8.52	2.68	3.081
	Buzdar et al. 2009	-	-	2.9	2.92
	Mia et al. 2019	76.8	-	2.79	2.96

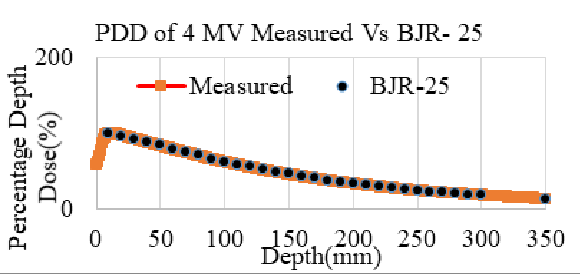

***Fig 7:** PDD curve for a 10 × 10 cm² field size using a 4 MV photon beam*

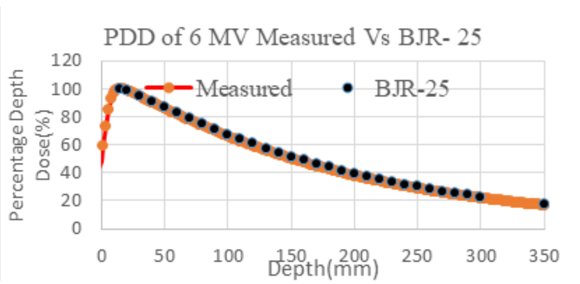

***Fig 8:** PDD curve for a 10 × 10 cm² field size using a 6 MV photon beam*

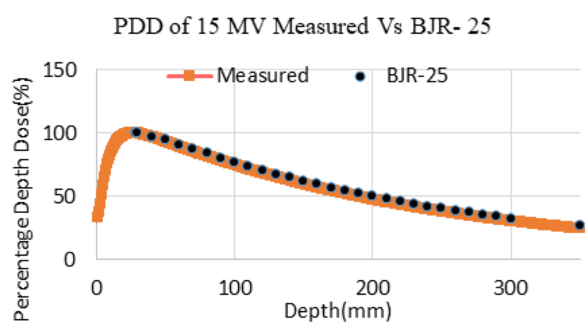

***Fig 9:** PDD curve for a 10 × 10 cm² field size using a 15 MV photon beam*

4.2 Compliance with International Protocols

For low-energy photon beams (<10 MV), the expected PDD at a 10 cm depth should be up to 75%. For higher-energy beams, it can reach up to 89% (Almond et al., 1999; Shimozato et al., 2017). In this study, the PDD values at 10 cm depth were 62.2%, 66.1%, and 74.9% for 4 MV, 6 MV, and 15 MV beams, respectively. These results are well within the recommended tolerance limits, indicating that the Elekta Synergy LINAC meets the dosimetric standards specified in the AAPM TG-51 protocol (Kragl et al., 2009; Beyer, 2013).

5. CONCLUSION

Accurate knowledge of a linear accelerator's percentage depth dose (PDD) is essential for effective radiotherapy treatment planning, so that the prescribed dose is delivered to the tumor while minimizing exposure to surrounding healthy tissues. In this study, PDD values increase with photon beam energy due to greater penetration and also rise with increasing field size. Conversely, the depth of maximum dose (d_{max}) increases with higher beam energy but slightly decreases with larger field sizes. The measured PDDs showed excellent agreement with reference data from BJR-25 and other published studies across multiple depths and field sizes, confirming the reliability of the Elekta Synergy LINAC. These results reinforce accurate dose calculation, provide essential guidance for optimizing treatment planning, and contribute to enhanced precision and improved clinical outcomes in radiotherapy.

REFERENCES

Ali, J., Sohail, M., Samad, A., Ahmad, I., Soomro, H., Biradar, G., Naz, I., & Tariq, I. (2023). Comparison of percentage depth doses with the published data for Co-60 radiotherapy machine at a regional cancer hospital. *Journal of Physics and Its Applications, 6*(1), 24–30.

Almond, P. R., Biggs, P. J., Coursey, B. M., Hanson, W. F., Huq, M. S., Nath, R., & Rogers, D. W. (1999). AAPM's TG-51 protocol for clinical reference dosimetry of high-energy photon and electron beams. *Medical Physics, 26*(9), 1847–1870.
DOI: 10.1118/1.598691
PMID: 10505874

Bewley, D. K. (1983). Central axis depth dose data for use in radiotherapy. *Br. J. Radiol. Suppl., 17*, 1–47.

Beyer, G. P. (2013). Commissioning measurements for photon beam data on three TrueBeam linear accelerators, and comparison with Trilogy and Clinac 2100 linear accelerators. *Journal of Applied Clinical Medical Physics, 14*(1), 273–288.
DOI: 10.1120/jacmp.v14i1.4077
PMID: 23318395 PMCID: PMC5714054

Bilge, H., Ozbek, N., Okutan, M., Cakir, A., & Acar, H. (2010). Surface dose and build-up region measurements with wedge filters for 6 and 18 MV photon beams. *Japanese Journal of Radiology, 28*(2), 110–116.
DOI: 10.1007/s11604-009-0393-5
PMID: 20182845

Brahme, A. (1984). Dosimetric precision requirements in radiation therapy. *Acta Radiologica: Oncology, 23*(5), 379–391.
DOI: 10.3109/02841868409136037
PMID: 6095609

Buzdar, S. A., Rao, M. A., & Nazir, A. (2009). An analysis of depth dose characteristics of photon in water. *Journal of Ayub Medical College Abbottabad, 21*(4), 41–45.

Corradini, S., Alongi, F., Andratschke, N., Belka, C., Boldrini, L., Cellini, F., Debus, J., Guckenberger, M., Hörner-Rieber, J., Lagerwaard, F. J., & Mazzola, R. (2019). MR-guidance in clinical reality: Current treatment challenges and future perspectives. *Radiation Oncology, 14*(1), 92.
DOI: 10.1186/s13014-019-1308-y
PMID: 31167658 PMCID: PMC6551911

International Atomic Energy Agency. (2004). *Absorbed dose determination in external beam radiotherapy: An international code of practice for dosimetry based on standards of absorbed dose to water* (Technical Report Series No. 398). IAEA.

Jordan, T. J. (1996). Section 5. Megavoltage x-ray beams: 2–50 MV. *Br. J. Radiol. Suppl., 25*.

Kato, H., Fujii, S., & Suzuki, S. (2004). Method of calculating percentage depth dose for diagnostic X-rays. *Nihon Hoshasen Gijutsu Gakkai Zasshi, 60*(8), 1107–1115.
DOI: 10.6009/jjrt.KJ00000922571
PMID: 15389168

Khan, F. M., & Gibbons, J. P. (2014). *Khan's the physics of radiation therapy*. Lippincott Williams & Wilkins.

Knutson, N. C., Schmidt, M. C., Belley, M. D., Nguyen, N., Price, M., Mutic, S., Sajo, E., & Li, H. H. (2018). Equivalency of beam scan data collection using a 1D tank and automated couch movements to traditional 3D tank measurements. *Journal of Applied Clinical Medical Physics, 19*(6), 60–67.
DOI: 10.1002/acm2.12444 PMID: 30188009 PMCID: PMC6236829

Kragl, G., af Wetterstedt, S., Knäusl, B., Lind, M., McCavana, P., Knöös, T., McClean, B., & Georg, D. (2009). Dosimetric characteristics of 6 and 10 MV unflattened photon beams. *Radiotherapy and Oncology, 93*(1), 141–146.
DOI: 10.1016/j.radonc.2009.06.008
PMID: 19592123

Mani, K. R., Bhuiyan, M. A., Rahman, M. S., & Islam,

S. A. (2018). Open beam dosimetric characteristics of TrueBeam medical linear accelerator with flattening filter (WFF) and flattening filter free (FFF) beam. *Polish Journal of Medical Physics and Engineering, 24*(2), 79–89.
DOI: 10.2478/pjmpe-2018-0011

Memon, S. A., Laghari, N. A., Mangi, F. H., Ahmad, F., Hussain, M. M., Palijo, S., Jhatyal, N., & Adeel, A. (2015). Analysis and verification of percent depth dose and tissue maximum ratio for Co-60 gamma ray beam. *World Applied Sciences Journal, 33*(1), 109–113.

Mia, M. A., Rahman, M. S., Purohit, S., Kabir, S. M., & Meaze, A. K. (2019). Analysis of percentage depth dose for 6 and 15 MV photon energies of medical linear accelerator with CC13 ionization chamber. *Nuclear Science and Applications, 28*(1&2).

Mihailidis, D. (2011). *The physics & technology of radiation therapy*.
DOI: 10.1118/1.3594546

Musolino, S. V. (2001). Absorbed dose determination in external beam radiotherapy: An international code of practice for dosimetry based on standards of absorbed dose to water; Technical Reports Series No. 398.
DOI: 10.1097/00004032-200111000-00017

Omer, M. A. (2015). Partial quality assessment of ^{60}Co-teletherapy machine performance. *Open Journal of Radiology, 5*(4), 235.
DOI: 10.4236/ojrad.2015.54032

Podgorsak, E. B. (2005). Treatment machines for external beam radiotherapy. In *IAEA radiation oncology physics: A handbook for teachers and students*. International Atomic Energy Agency.

Rahman, M., Shamsuzzaman, M., Sarker, M., Jobber, A., Mia, M., Bairagi, A. K., Ahmed, M., Reza, S., Malik, S. R., Bhuiyan, M. M., & Khan, A. H. (2021). Dosimetric characterization of medical linear accelerator photon and electron beams for the treatment accuracy of cancer patients. *World Journal of Advanced Engineering Technology and Sciences, 3*(1), 41–59.
DOI: 10.30574/wjaets.2021.3.1.0046

Roy, S. K., Das, P. K., Khatun, R., Rahman, M. A., Akter, S., Kumar, T., & Ahasan, M. M. (2021). Dosimetric characteristics of 6 MV medical linac at BAEC. *International Journal of Medical Physics, Clinical Engineering and Radiation Oncology, 10*(1), 38.
DOI: 10.4236/ijmpcero.2021.101004

Shimozato, T., Aoyama, Y., Matsunaga, T., & Tabushi, K. (2017). Beam characterization of 10-MV photon beam from medical linear accelerator without flattening filter. *Journal of Medical Physics, 42*(2), 65–71.
DOI: 10.4103/jmp.jmp_71_16
PMID: 28706351 PMCID: PMC5496272

Xhafa, B., Mulaj, T., Hodolli, G., & Nafezi, G. (2014). Dose distribution of photon beam by Siemens linear accelerator. *International Journal of Medical Physics, Clinical Engineering and Radiation Oncology.*
DOI: 10.4236/ijmpcero.2014.31011

List of Reviewers and Editors Vol 23(1)

Regd. No. 87/055/56 DAO/MOH/GON Volume 23(1)

Nepal Journal of Science and Technology (NJST) 23(1)
Published Year: 2025

Nepal Journal of Science and Technology (NJST)

NEPAL ACADEMY OF SCIENCE AND TECHNOLOGY (NAST)

Khumaltar, Lalitpur

GPO Box 3323, Kathmandu

Tel. 5547717, 5547715 Fax: 977-1-5547713

Email: njst@nast.org.np;scitechawareness@gmail.com

ISSN: 1994- 1412

8137 2157

e-ISSN 2382-5359 (Online)